Electronic Supplementary Material (ESI) for Inorganic Chemistry Frontiers.

SUPPORTING INFORMATION

Solvato- and vapochromic exchange-coupled Dy_2 single-molecule magnets achieved by attaching iron-cyanido metalloligands

Michal Liberka,[a,b] Mikolaj Zychowicz[a,b] and Szymon Chorazy*[a]

[a]Faculty of Chemistry, Jagiellonian University, Gronostajowa 2, 30-387 Kraków, Poland

[b]Doctoral School of Exact and Natural Sciences, Jagiellonian University, Łojasiewicza 11, 30-348 Kraków, Poland

*Corresponding author: simon.chorazy@uj.edu.pl

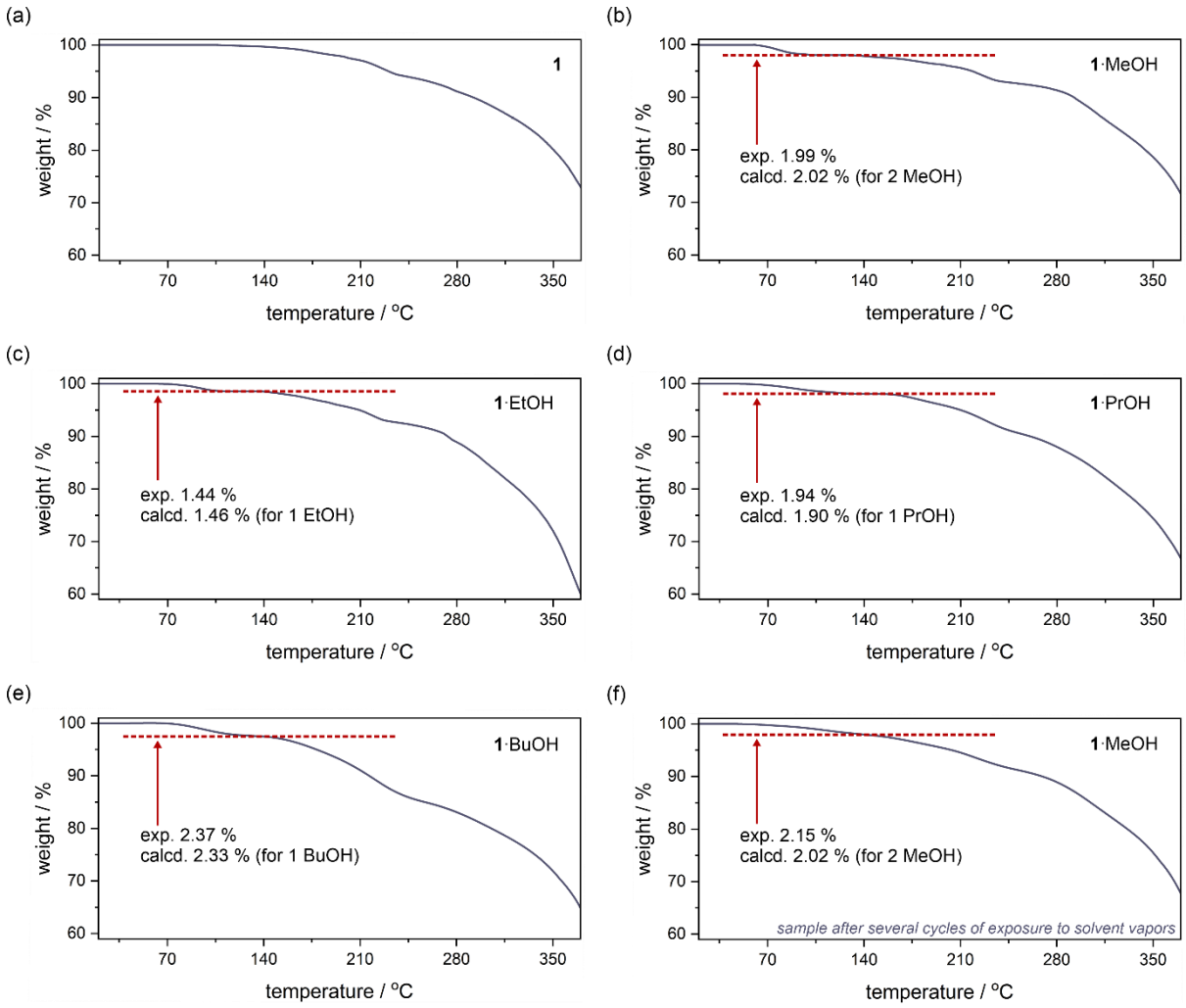

Fig. S1 Thermogravimetric curves collected in the temperature range of 20–370°C for crystalline samples of **1** (*a*), **1·MeOH** (*b*), **1·EtOH** (*c*), **1·PrOH** (*d*), **1·BuOH** (*e*), and **1·MeOH** after several cycles of exposure to solvent vapors (*f*; for details see Fig. S16 with the related comment). The steps related to the loss of solvent molecules are depicted.

Comment to Fig. S1: Upon heating from room temperature, the sample weight of **1** is almost stable up to 140°C, while the weight of **1·MeOH**, **1·EtOH**, **1·PrOH**, and **1·BuOH** is stable to ca. 70°C, and further heating results in a gradual weight loss attributable to the release of alcohol of crystallization. Up to 140°C, their thermogravimetric curves reach the plateau stage, which corresponds to the desolvated states. The related weight losses, depicted in Fig. S1, are in good agreement with the calculated ones. Further heating of all compounds to temperatures above 170°C leads to the dramatic decrease of the sample masses, which is presumably connected with the removal of the cyanido as well as organic ligands, and the resulting decomposition of compounds.

Table S1 Crystal data and structure refinement parameters for **1**, **1·MeOH**, **1·EtOH**, **1·PrOH**, and **1·BuOH**.

compound	**1**	**1·MeOH**	**1·EtOH**	**1·PrOH**	**1·BuOH**
formula	$C_{108}H_{82}Dy_2F_{18}Fe_2N_{22}O_{28}S_6$	$C_{110}H_{90}Dy_2F_{18}Fe_2N_{22}O_{30}S_6$	$C_{110}H_{88}Dy_2F_{18}Fe_2N_{22}O_{29}S_6$	$C_{111}H_{82}Dy_2F_{18}Fe_2N_{22}O_{29}S_6$	$C_{112}H_{82}Dy_2F_{18}Fe_2N_{22}O_{29}S_6$
form. weight / g·mol^{-1}	3107.02	3171.11	3153.09	3159.05	3171.06
λ / Å	0.71073 Å (Mo Kα)				
T / K	100(2)				
crystal system	triclinic				
space group	P −1 (No. 2)				
a / Å	12.6470(16)	12.730(2)	12.6551(6)	12.6685(6)	12.5602(14)
b / Å	14.848(2)	14.823(3)	14.8665(7)	14.8474(8)	14.8503(16)
c / Å	18.720(2)	18.736(3)	18.7758(10)	18.8366(12)	18.911(2)
α / deg	66.965(4)	66.810(5)	66.8570(10)	66.8230(10)	67.271(3)
β / deg	82.140(4)	83.324(5)	82.012(2)	84.052(2)	81.565(3)
γ / deg	71.166(4)	71.290(5)	71.4210(10)	71.4140(10)	71.608(3)
V / Å^3	3061.5(7)	3077.9(9)	3078.5(3)	3086.3(3)	3085.9(6)
Z	1	1	1	1	1
calcd. density / g·cm^{-1}	1.685	1.711	1.701	1.700	1.706
abs. coeff. / cm^{-1}	1.651	1.645	1.643	1.640	1.640
F(000)	1550	1586	1576	1576	1582
Θ range / deg	2.301−25.027	2.851−25.027	2.294−25.027	2.353−25.027	2.289−25.027
collected refl.	37526	33571	37902	40057	34235
limiting indices	−15 < h < 14 −17 < k < 17 −22 < l < 22	−15 < h < 15 −17 < k < 17 −22 < l < 22	−15 < h < 15 −17 < k < 17 −22 < l < 22	−15 < h < 15 −17 < k < 17 −22 < l < 22	−14 < h < 14 −17 < k < 17 −22 < l < 22
R_{int}	0.0303	0.024	0.063	0.0403	0.089
completeness / %	99.8	99.7	99.9	99.9	99.8
data/restraints/param.	10802/39/910	10847/26/874	10875/21/865	10908/42/874	10878/84/883
GOF on F^2	1.054	1.050	1.075	1.099	1.063
final R_1 [$I > 2\sigma(I)$]	0.0252	0.0211	0.0435	0.0401	0.0761
final wR_2 [all data]	0.0615	0.0513	0.0835	0.0912	0.1948
diff. peak and hole / e·Å^{-3}	0.786 and −0.419	0.617 and −0.513	1.035 and −1.097	2.119 and −1.054	2.498 and −1.402

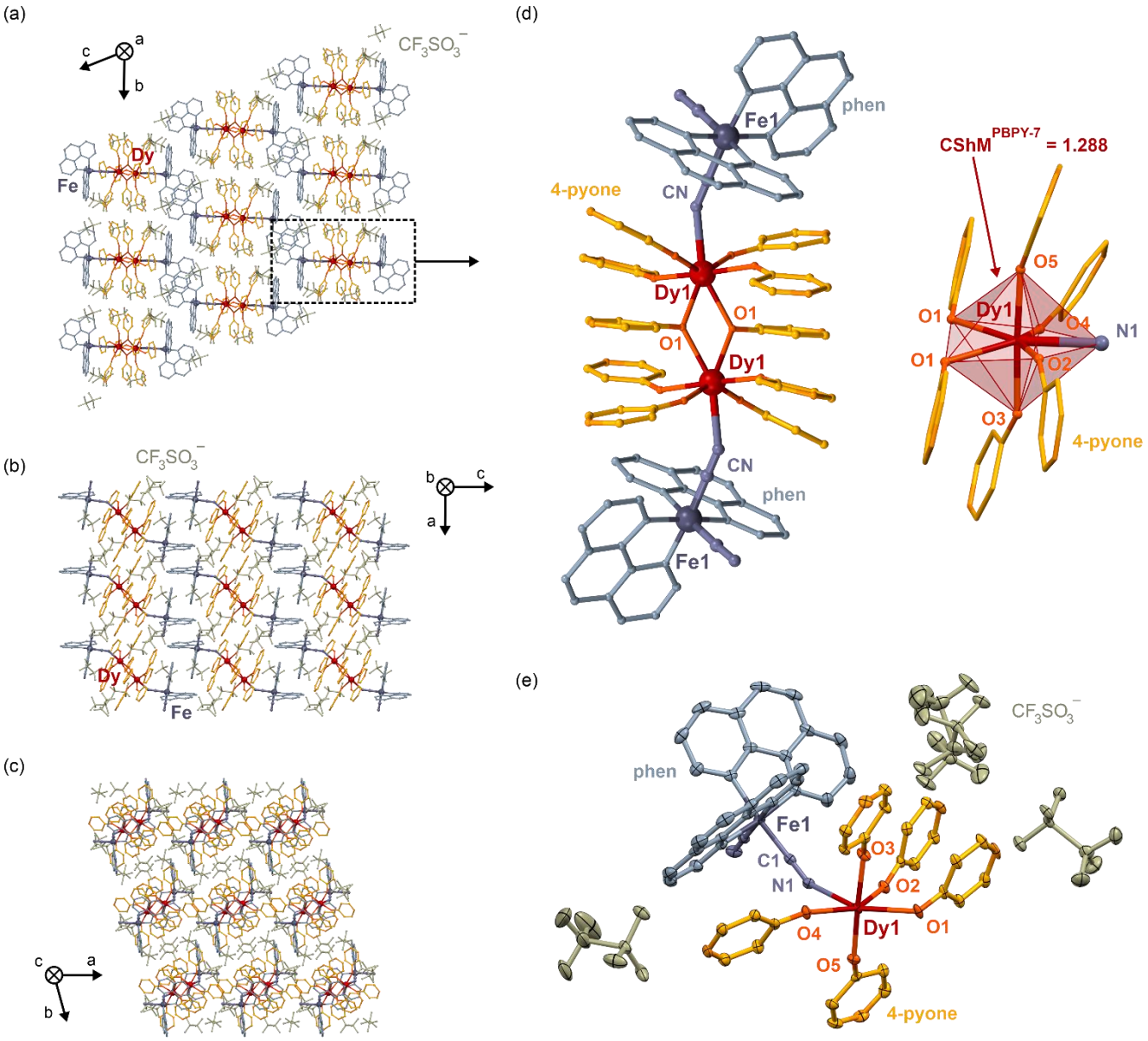

Fig. S2 Detailed structural views of **1**: the representative views of the supramolecular network along the crystallographic *a* axis (*a*), *b* axis (*b*), and *c* axis (*c*), the enlarged view of a tetrametallic $\{Dy^{III}_2Fe^{II}_2\}^{6+}$ molecule and the coordination polyhedron of incorporated seven-coordinated Dy^{III} complexes (*d*), and the asymmetric unit with the labeling scheme for selected symmetrically independent atoms (*e*). The hydrogen atoms are omitted for clarity. Thermal ellipsoids in (*e*) are presented at the 50% probability level. Detailed structure parameters are gathered in Table S2 (see below).

Table S2 Detailed crystal structure parameters for **1**. The labeling scheme is presented in Fig. S2 (see above).

distances in dysprosium(III) and iron(II) complexes / Å					
Dy1–O1	2.3967(18)/ 2.4188(18)	Dy1–O5	2.2354(19)	Fe1–N3	1.970(2)
Dy1–O2	2.2893(18)	Dy1–N1	2.496(2)	Fe1–N4	2.002(2)
Dy1–O3	2.229(2)	Fe1–C1	1.895(3)	Fe1–N5	2.005(2)
Dy1–O4	2.2791(19)	Fe1–C2	1.893(3)	Fe1–N6	1.972(2)
angles in dysprosium(III) and iron(II) complexes / °					
O1–Dy1–O1	63.50(7)	O3–Dy1–O5	172.80(7)	C2–Fe1–N4	92.84(11)
O1–Dy1–O2	80.94(6)/ 141.77(7)	O3–Dy1–N1	87.95(8)	C2–Fe1–N5	174.62(11)
O1–Dy1–O3	79.93(7)/ 98.19(7)	O4–Dy1–O5	98.78(7)	C2–Fe1–N6	92.31(11)
O1–Dy1–O4	130.93(6)/ 72.18(7)	O4–Dy1–N1	72.06(7)	N3–Fe1–N4	81.85(10)
O1–Dy1–O5	99.57(7)/ 87.91(7)	O5–Dy1–N1	89.42(7)	N3–Fe1–N5	93.93(10)
O1–Dy1–N1	152.58(7)/ 143.27(7)	C1–Fe1–C2	88.83(12)	N3–Fe1–N6	173.77(10)
O2–Dy1–O3	88.38(7)	C1–Fe1–N3	93.68(11)	N4–Fe1–N5	87.17(9)
O2–Dy1–O4	146.02(7)	C1–Fe1–N4	175.27(11)	N4–Fe1–N6	92.96(10)
O2–Dy1–O5	84.45(7)	C1–Fe1–N5	91.58(10)	N5–Fe1–N6	82.32(10)
O2–Dy1–N1	74.17(7)	C1–Fe1–N6	91.40(10)	–	–
O3–Dy1–O4	86.79(7)	C2–Fe1–N3	91.40(10)	–	–

distances and angles between dysprosium(III) and iron(II) centers / Å, °			
within $\{Dy_2Fe_2\}^{6+}$ molecules		between $\{Dy_2Fe_2\}^{6+}$ molecules (the shortest distance)	
Dy1···Dy1	4.103(5)	Dy1···Dy1	9.933(5) (along [100] direction)
Dy1–O1–Dy1	116.50(7)	Fe1···Fe1	8.828(5) (along $[1\bar{2}1]$ direction)
Dy1···Fe1	5.268(5)	–	–
Dy1–N1–C1	143.19(7)	–	–

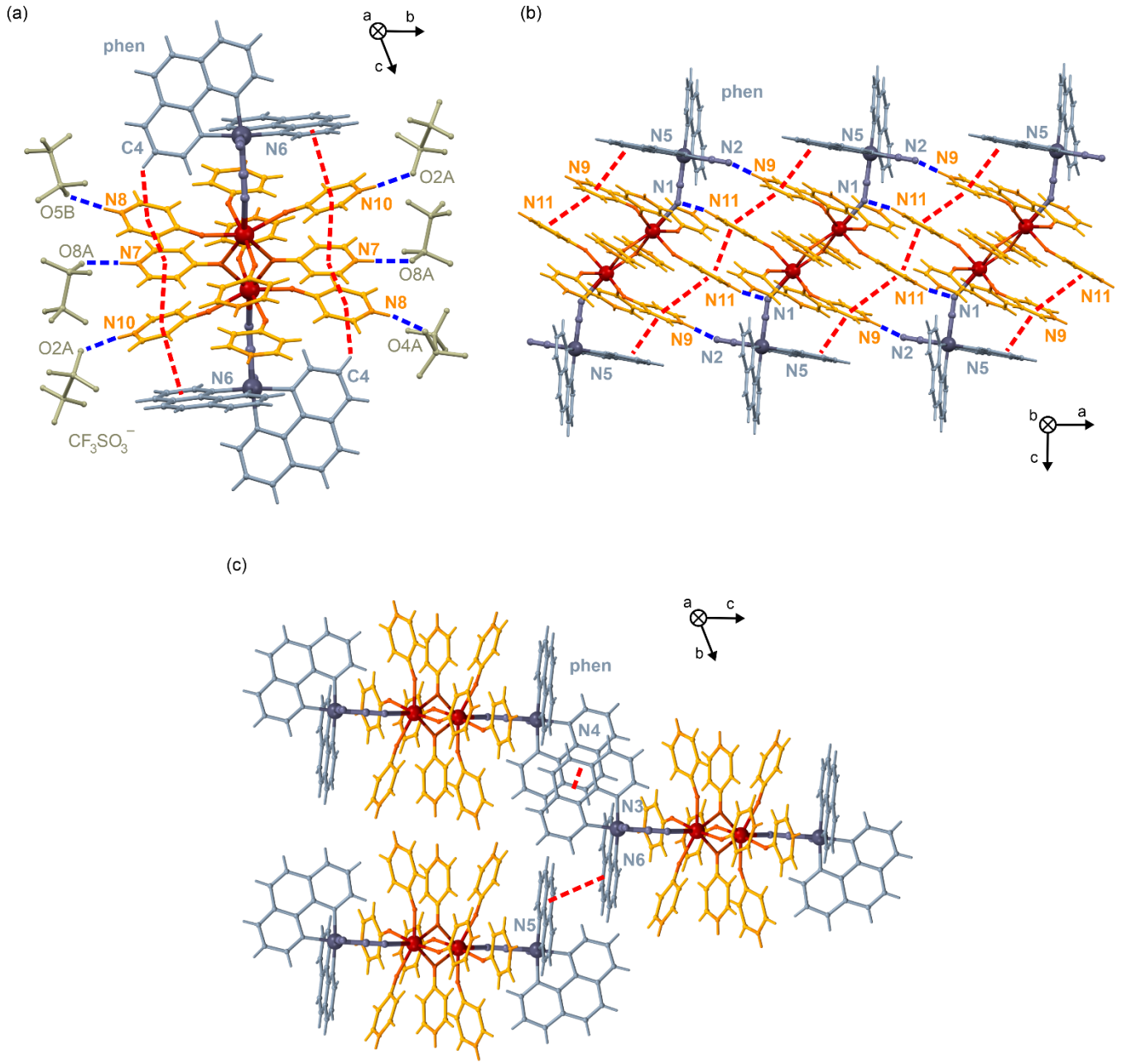

Fig. S3 The visualization of hydrogen bonds involving 4-pyridone ligands and trifluoromethanesulfonate anions or cyanido ligands (blue lines, *a* and *b*), as well as inter- and intramolecular π-π interactions involving 4-pyridone and phenanthroline ligands (red dashed lines, *a*-*c*) in the crystal structure of **1**. The metric parameters of both types of interactions are summarized in Table S3 (see below).

Table S3 Metric parameters for supramolecular interactions in the crystal structure of **1**. The labeling scheme is presented in Fig. S3 (see above).

hydrogen bonds between $CF_3SO_3^-$ ions and 4-pyridone ligands / Å, °		hydrogen bonds between cyanido and 4-pyridone ligands / Å, °	
$N7_L\cdots O8A_{OTf}$ $H7_L\cdots O8A_{OTf}$ $N7_L–H7_L\cdots O8A_{OTf}$	2.789 1.934 172.67	$N9_L\cdots N2_{CN}$ $H9_L\cdots N2_{CN}$ $N9_L–H9_L\cdots N2_{CN}$	2.711 1.882 161.46
$N8_L\cdots O4A_{OTf}$ $H8_L\cdots O4A_{OTf}$ $N8_L–H8_L\cdots O4A_{OTf}$	2.802 1.953 168.84	$N11_L\cdots N1_{CN}$ $H11_L\cdots N1_{CN}$ $N11_L–H11_L\cdots N1_{CN}$	3.035 2.227 147.02
$N8_L\cdots O5B_{OTf}$ $H8_L\cdots O5B_{OTf}$ $N8_L–H8_L\cdots O5B_{OTf}$	2.884 2.049 163.70	–	–
$N10_L\cdots O2A_{OTf}$ $H10_L\cdots O2A_{OTf}$ $N10_L–H10_L\cdots O2A_{OTf}$	2.811 1.986 160.54	–	–
π–π interactions within $\{Dy_2Fe_2\}^{6+}$ molecules / Å, °		π–π interactions between $\{Dy_2Fe_2\}^{6+}$ molecules / Å	
$\pi_{phen}{}^{N6}\cdots\pi_L{}^{N10}$	3.704	$\pi_L{}^{N11}\cdots\pi_L{}^{N11}$	3.546
$\pi_L{}^{N10}\cdots\pi_L{}^{N7}$	3.698	$\pi_{phen}\cdots\pi_{phen}$ (along [001] direction)	3.829
$\pi_L{}^{N7}\cdots\pi_L{}^{N8}$	3.545	$\pi_{phen}\cdots\pi_{phen}$ (along [100] direction)	3.562
$\pi_L{}^{N8}\cdots C4_{phen}$ $\pi_L{}^{N8}\cdots H4_{phen}$ $\pi_L{}^{N8}\cdots H4_{phen}–C4_{phen}$	3.516 2.841 130.33	–	–
$\pi_{phen}{}^{N5}\cdots\pi_L{}^{N9}$	3.988	–	–
$\pi_L{}^{N9}\cdots\pi_L{}^{N11}$	3.996	–	–

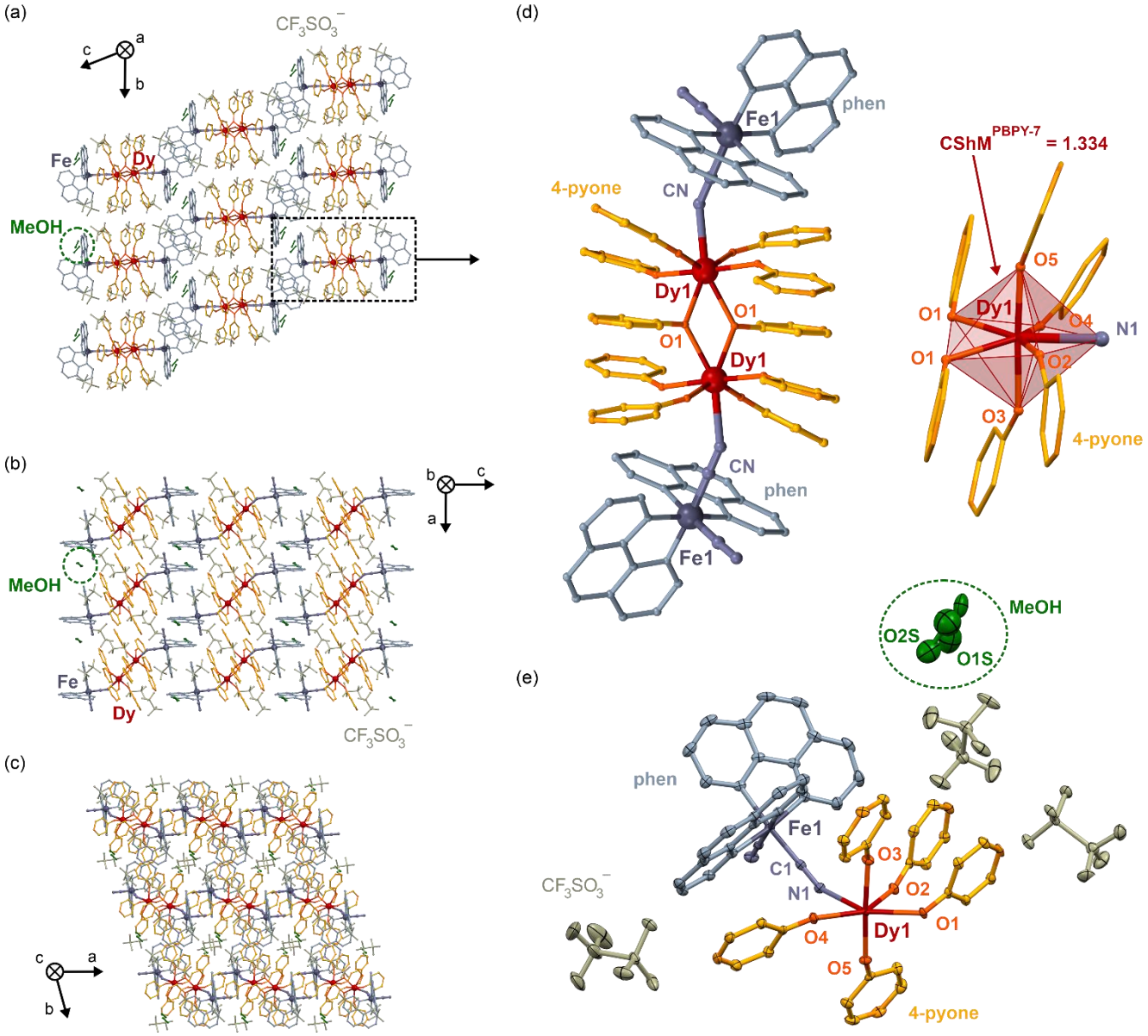

Fig. S4 Detailed structural views of **1·MeOH**: the representative views of the supramolecular network along the crystallographic *a* axis (*a*), *b* axis (*b*), and *c* axis (*c*), the enlarged view of a tetrametallic $\{Dy^{III}_2Fe^{II}_2\}^{6+}$ molecule and the coordination polyhedron of seven-coordinated Dy^{III} complexes (*d*), and the asymmetric unit with the labeling scheme for selected symmetrically independent atoms (*e*). The hydrogen atoms are omitted for clarity. Thermal ellipsoids in (*e*) are presented at the 50% probability level. Detailed structure parameters are gathered in Table S4 (see below).

Table S4 Detailed crystal structure parameters for **1·MeOH**. The labeling scheme is presented in Fig. S4 (see above).

distances in dysprosium(III) and iron(II) complexes / Å					
Dy1−O1	2.4008(14)/ 2.4207(15)	Dy1−O5	2.2312(15)	Fe1−N3	1.9694(19)
Dy1−O2	2.2897(15)	Dy1−N1	2.4910(18)	Fe1−N4	2.0052(19)
Dy1−O3	2.2286(15)	Fe1−C1	1.890(2)	Fe1−N5	2.0030(19)
Dy1−O4	2.2767(15)	Fe1−C2	1.893(2)	Fe1−N6	1.9751(19)
angles in dysprosium(III) and iron(II) complexes / °					
O1−Dy1−O1	63.37(6)	O3−Dy1−O5	172.80(5)	C2−Fe1−N4	93.00(8)
O1−Dy1−O2	81.06(5)/ 141.46(5)	O3−Dy1−N1	88.31(6)	C2−Fe1−N5	175.02(9)
O1−Dy1−O3	79.60(6)/ 98.40(6)	O4−Dy1−O5	98.89(6)	C2−Fe1−N6	92.70(9)
O1−Dy1−O4	130.63(5)/ 72.29(5)	O4−Dy1−N1	72.44(6)	N3−Fe1−N4	81.88(8)
O1−Dy1−O5	99.87(6)/ 87.67(5)	O5−Dy1−N1	89.07(6)	N3−Fe1−N5	93.64(8)
O1−Dy1−N1	152.47(5)/ 143.59(5)	C1−Fe1−C2	88.78(9)	N3−Fe1−N6	173.02(8)
O2−Dy1−O3	88.69(6)	C1−Fe1−N3	94.23(9)	N4−Fe1−N5	87.19(7)
O2−Dy1−O4	146.20(5)	C1−Fe1−N4	175.75(8)	N4−Fe1−N6	92.20(8)
O2−Dy1−O5	84.14(6)	C1−Fe1−N5	91.37(8)	N5−Fe1−N6	82.32(8)
O2−Dy1−N1	73.97(6)	C1−Fe1−N6	91.57(8)	–	–
O3−Dy1−O4	86.71(6)	C2−Fe1−N3	91.31(8)	–	–

distances and angles between dysprosium(III) and iron(II) centers / Å, °			
within $\{Dy_2Fe_2\}^{6+}$ molecules		between $\{Dy_2Fe_2\}^{6+}$ molecules (the shortest distance)	
Dy1···Dy1	4.103(4)	Dy1···Dy1	9.983(5) (along [100] direction)
Dy1−O1−Dy1	116.48(6)	Fe1···Fe1	8.857(5) (along [$\bar{2}$11] direction)
Dy1···Fe1	5.263(4)	–	–
Dy1−N1−C1	142.87(6)	–	–

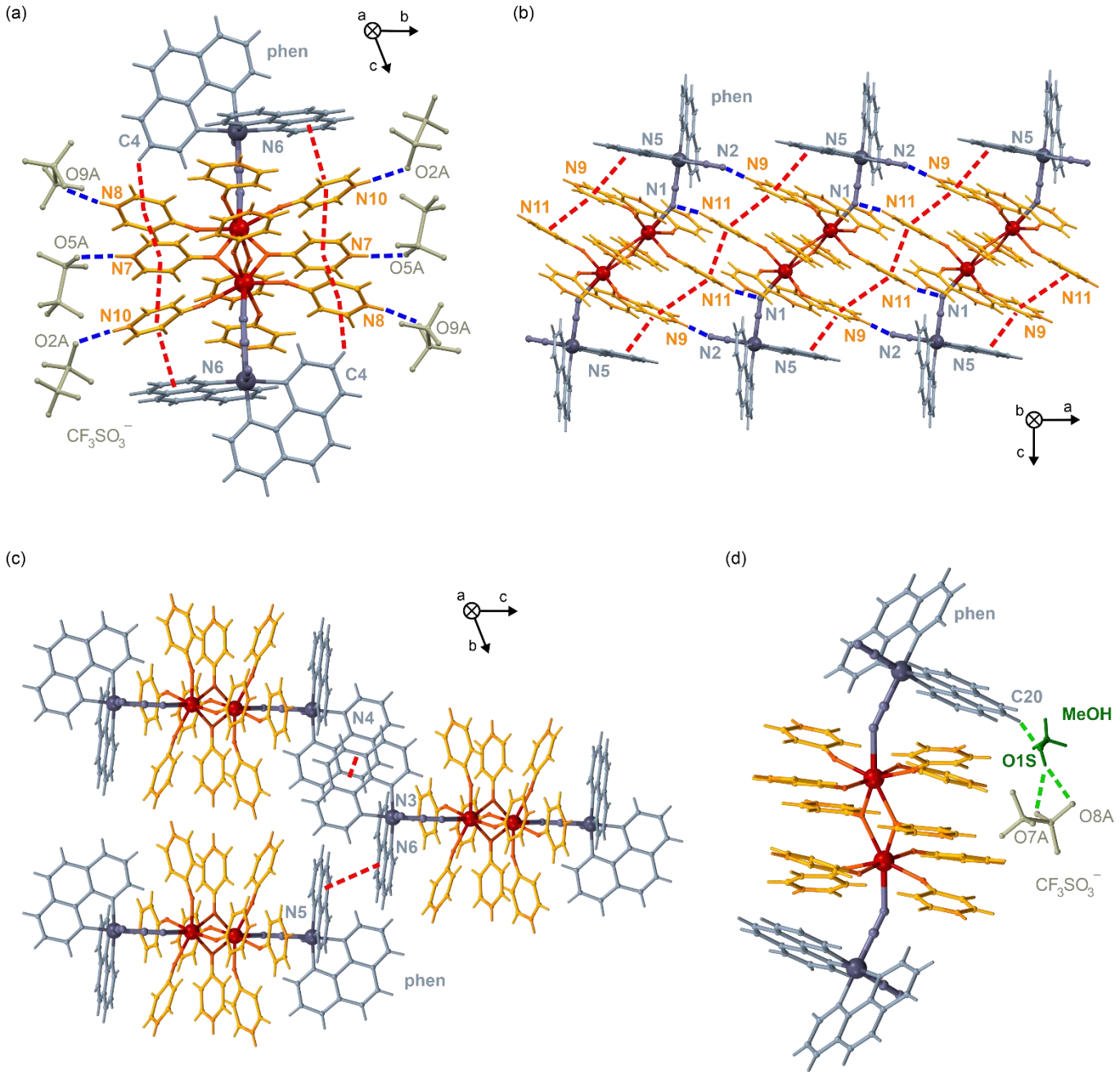

Fig. S5 The visualization of hydrogen bonds involving 4-pyridone ligands and trifluoromethanesulfonate anions or cyanido ligands (blue lines, *a* and *b*), inter- and intramolecular *π*-*π* interactions involving 4-pyridone and phenanthroline ligands (red dashed lines, *a*-*c*), as well as hydrogen bonds engaging solvent MeOH molecules (green dashed lines, *d*) in the crystal structure of **1·MeOH**. The metric parameters of both types of interactions are summarized in Table S5 (see below).

Table S5 Metric parameters for supramolecular interactions in the crystal structure of **1·MeOH**. The labeling scheme is presented in Fig. S5 (see above).

hydrogen bonds between $CF_3SO_3^-$ ions and 4-pyridone ligands / Å, °		hydrogen bonds between cyanido and 4-pyridone ligands / Å, °	
$N7_L\cdots O5A_{OTf}$ $H7_L\cdots O5A_{OTf}$ $N7_L–H7_L\cdots O5A_{OTf}$	2.784 1.938 169.99	$N9_L\cdots N2_{CN}$ $H9_L\cdots N2_{CN}$ $N9_L–H9_L\cdots N2_{CN}$	2.715 1.886 161.45
$N8_L\cdots O9A_{OTf}$ $H8_L\cdots O9A_{OTf}$ $N8_L–H8_L\cdots O9A_{OTf}$	2.820 1.972 168.55	$N11_L\cdots N1_{CN}$ $H11_L\cdots N1_{CN}$ $N11_L–H11_L\cdots N1_{CN}$	3.040 2.277 147.88
$N10_L\cdots O2A_{OTf}$ $H10_L\cdots O2A_{OTf}$ $N10_L–H10_L\cdots O2A_{OTf}$	2.815 1.986 161.38	–	–
π–π interactions within $\{Dy_2Fe_2\}^{6+}$ molecules / Å, °		π–π interactions between $\{Dy_2Fe_2\}^{6+}$ molecules / Å	
$\pi_{phen}{}^{N6}\cdots\pi_L{}^{N10}$	3.678	$\pi_L{}^{N11}\cdots\pi_L{}^{N11}$	3.556
$\pi_L{}^{N10}\cdots\pi_L{}^{N7}$	3.714	$\pi_{phen}\cdots\pi_{phen}$ (along [001] direction)	3.857
$\pi_L{}^{N7}\cdots\pi_L{}^{N8}$	3.562	$\pi_{phen}\cdots\pi_{phen}$ (along [100] direction)	3.576
$\pi_L{}^{N8}\cdots C4_{phen}$ $\pi_L{}^{N8}\cdots H4_{phen}$ $\pi_L{}^{N8}\cdots H4_{phen}–C4_{phen}$	3.569 2.896 130.33	hydrogen bonds involving crystallization MeOH molecules / Å, °	
$\pi_{phen}{}^{N5}\cdots\pi_L{}^{N9}$	4.007	$O1S_{MeOH}\cdots C20_{phen}$ $O1S_{MeOH}\cdots H20_{phen}$ $O1S_{MeOH}\cdots H20_{phen}–C20_{phen}$	3.386 2.523 154.60
$\pi_L{}^{N9}\cdots\pi_L{}^{N11}$	4.030	$O1S_{MeOH}\cdots O7A_{OTf}$ $H1S_{MeOH}\cdots O7A_{OTf}$ $O1S_{MeOH}–H1S_{MeOH}\cdots O7A_{OTf}$	3.175 2.414 154.83
–	–	$O1S_{MeOH}\cdots O8A_{OTf}$ $H1S_{MeOH}\cdots O8A_{OTf}$ $O1S_{MeOH}–H1S_{MeOH}\cdots O8A_{OTf}$	3.813 3.149 139.81

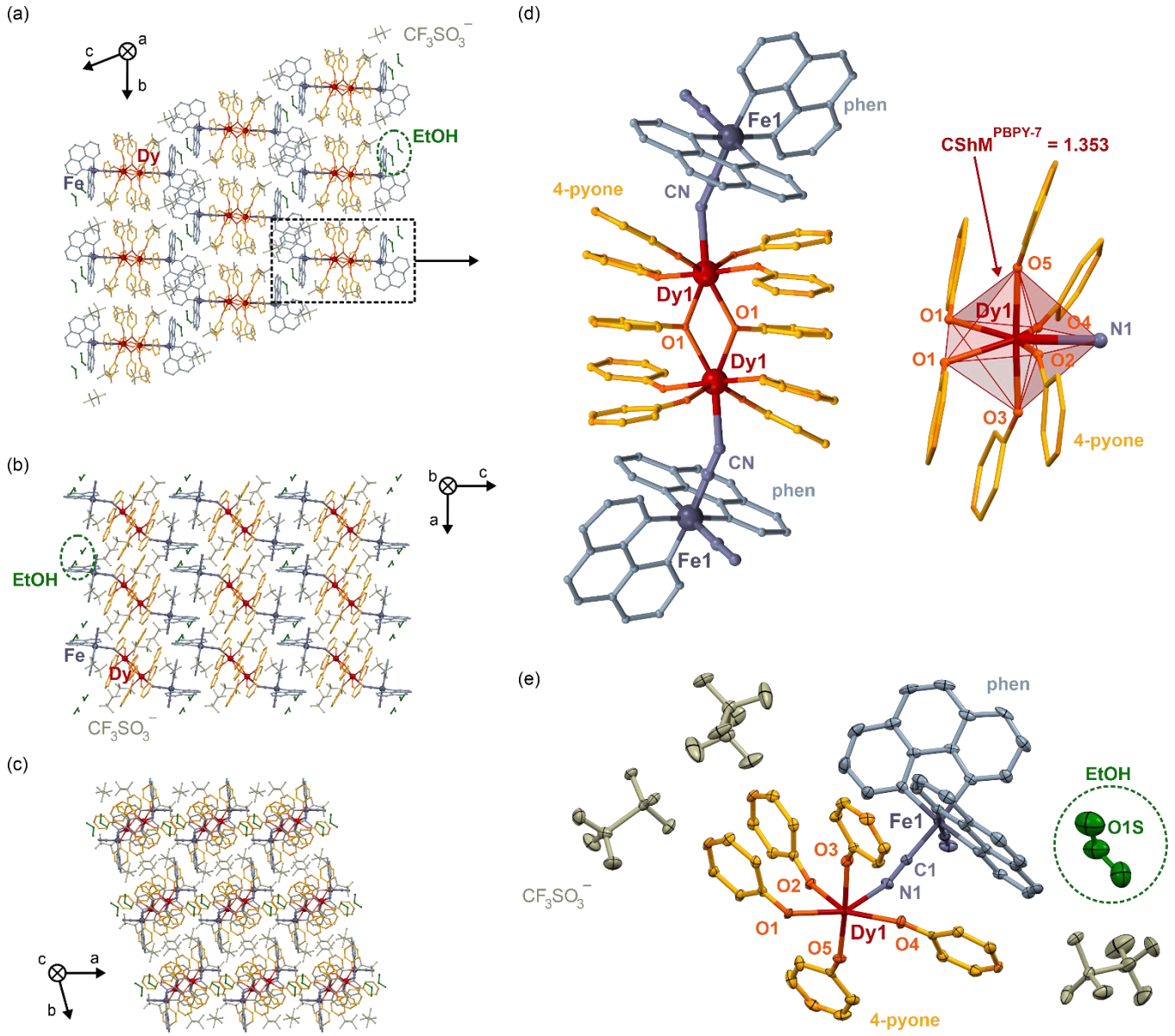

Fig. S6 Detailed structural views of **1·EtOH**: the representative views of the supramolecular network along the crystallographic *a* axis (*a*), *b* axis (*b*), and *c* axis (*c*), the enlarged view of a tetrametallic $\{Dy^{III}_2Fe^{II}_2\}^{6+}$ molecule and the coordination polyhedron of seven-coordinated Dy^{III} complexes (*d*), and the asymmetric unit with the labeling scheme for selected symmetrically independent atoms (*e*). The hydrogen atoms are omitted for clarity. Thermal ellipsoids in (*e*) are presented at the 50% probability level. Detailed structure parameters are gathered in Table S6 (see below).

Table S6 Detailed crystal structure parameters for **1·EtOH**. The labeling scheme is presented in Fig. S6 (see above).

distances in dysprosium(III) and iron(II) complexes / Å					
Dy1–O1	2.399(3)/ 2.417(3)	Dy1–O5	2.229(3)	Fe1–N3	1.964(4)
Dy1–O2	2.290(3)	Dy1–N1	2.493(4)	Fe1–N4	2.002(4)
Dy1–O3	2.228(3)	Fe1–C1	1.895(5)	Fe1–N5	1.999(4)
Dy1–O4	2.275(3)	Fe1–C2	1.891(5)	Fe1–N6	1.972(4)
angles in dysprosium(III) and iron(II) complexes / °					
O1–Dy1–O1	63.56(11)	O3–Dy1–O5	173.10(11)	C2–Fe1–N4	92.36(18)
O1–Dy1–O2	80.88(10)/ 141.12(11)	O3–Dy1–N1	87.19(12)	C2–Fe1–N5	174.85(19)
O1–Dy1–O3	79.65(11)/ 98.58(11)	O4–Dy1–O5	98.37(12)	C2–Fe1–N6	92.47(18)
O1–Dy1–O4	130.89(11)/ 72.43(11)	O4–Dy1–N1	72.47(12)	N3–Fe1–N4	81.77(16)
O1–Dy1–O5	100.33(11)/ 87.50(11)	O5–Dy1–N1	89.80(12)	N3–Fe1–N5	93.51(16)
O1–Dy1–N1	151.65(11)/ 143.99(11)	C1–Fe1–C2	89.2(2)	N3–Fe1–N6	173.24(17)
O2–Dy1–O3	89.46(11)	C1–Fe1–N3	94.03(18)	N4–Fe1–N5	87.07(16)
O2–Dy1–O4	146.33(11)	C1–Fe1–N4	175.56(18)	N4–Fe1–N6	92.58(16)
O2–Dy1–O5	83.74(11)	C1–Fe1–N5	91.77(18)	N5–Fe1–N6	82.45(16)
O2–Dy1–N1	73.93(12)	C1–Fe1–N6	91.51(18)	–	–
O3–Dy1–O4	86.65(12)	C2–Fe1–N3	91.47(18)	–	–

distances and angles between dysprosium(III) and iron(II) centers / Å, °			
within $\{Dy_2Fe_2\}^{6+}$ molecules		between $\{Dy_2Fe_2\}^{6+}$ molecules (the shortest distance)	
Dy1···Dy1	4.094(8)	Dy1···Dy1	9.936(5) (along [100] direction)
Dy1–O1–Dy1	116.46(11)	Fe1···Fe1	8.857(5) (along $[1\bar{2}1]$ direction)
Dy1···Fe1	5.280(8)	–	–
Dy1–N1–C1	143.55(11)	–	–

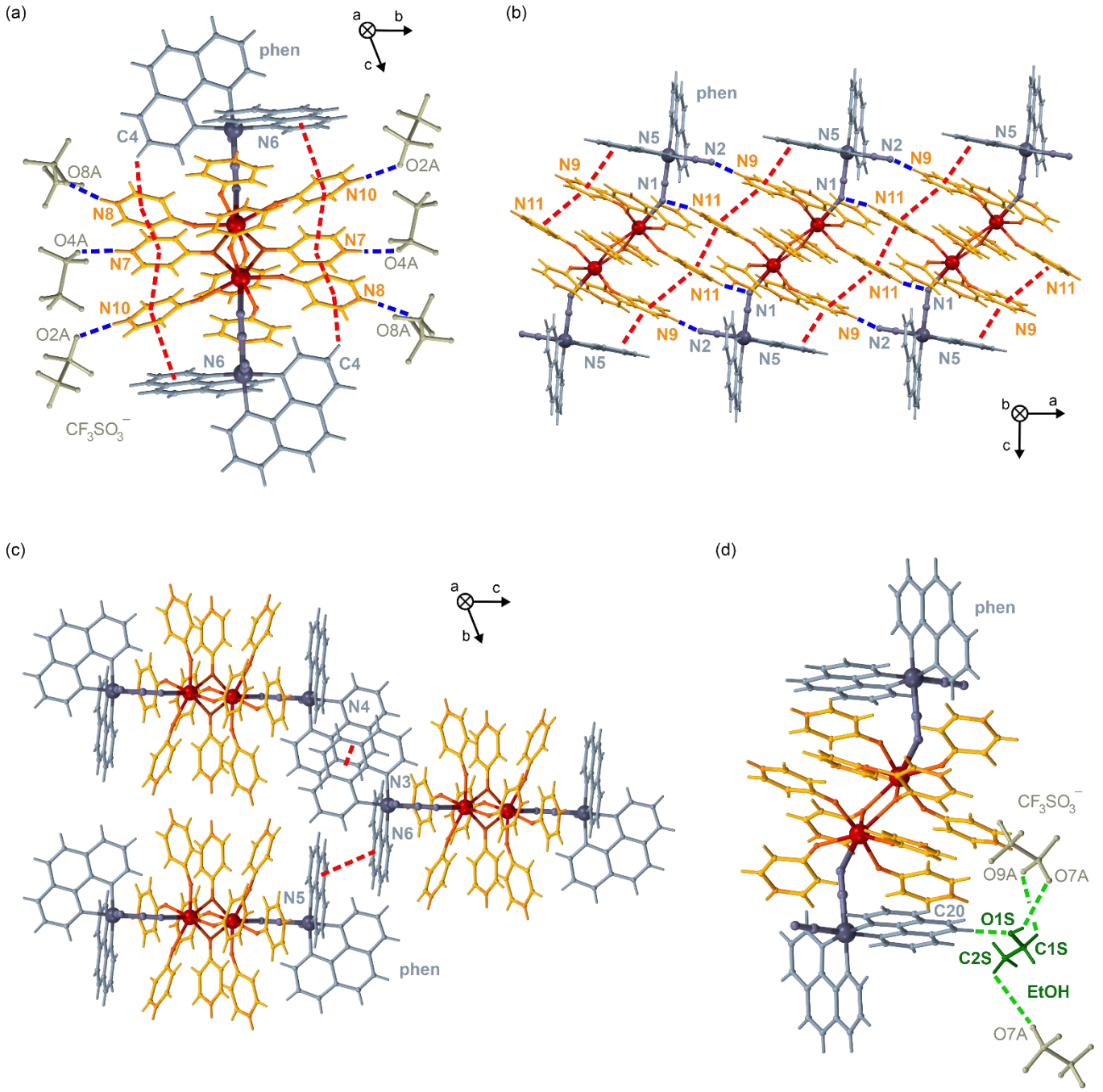

Fig. S7 The visualization of hydrogen bonds involving 4-pyridone ligands and trifluoromethanesulfonate anions or cyanido ligands (blue lines, *a* and *b*), inter- and intramolecular *π*-*π* interactions involving 4-pyridone and phenanthroline ligands (red dashed, *a*-*c*), as well as hydrogen bonds engaging solvent EtOH molecules (green dashed lines, *d*) in the crystal structure of **1·EtOH**. The metric parameters of both types of interactions are summarized in Table S7 (see below).

Table S7 Metric parameters for supramolecular interactions in the crystal structure of **1·EtOH**. The labeling scheme is presented in Fig. S7 (see above).

hydrogen bonds between $CF_3SO_3^-$ ions and 4-pyridone ligands / Å, °		hydrogen bonds between cyanido and 4-pyridone ligands / Å, °	
$N7_L\cdots O4A_{OTf}$ $H7_L\cdots O4A_{OTf}$ $N7_L–H7_L\cdots O4A_{OTf}$	2.785 1.933 170.29	$N9_L\cdots N2_{CN}$ $H9_L\cdots N2_{CN}$ $N9_L–H9_L\cdots N2_{CN}$	2.717 1.889 161.28
$N8_L\cdots O8A_{OTf}$ $H8_L\cdots O8A_{OTf}$ $N8_L–H8_L\cdots O8A_{OTf}$	2.796 1.950 167.33	$N11_L\cdots N1_{CN}$ $H11_L\cdots N1_{CN}$ $N11_L–H11_L\cdots N1_{CN}$	3.039 2.261 150.60
$N10_L\cdots O2A_{OTf}$ $H10_L\cdots O2A_{OTf}$ $N10_L–H10_L\cdots O2A_{OTf}$	2.817 1.990 161.07	–	–
π–π interactions within $\{Dy_2Fe_2\}^{6+}$ molecules / Å, °		π–π interactions between $\{Dy_2Fe_2\}^{6+}$ molecules / Å	
$\pi_{phen}{}^{N6}\cdots\pi_L{}^{N10}$	3.681	$\pi_L{}^{N11}\cdots\pi_L{}^{N11}$	3.535
$\pi_L{}^{N10}\cdots\pi_L{}^{N7}$	3.716	$\pi_{phen}\cdots\pi_{phen}$ (along [001] direction)	3.829
$\pi_L{}^{N7}\cdots\pi_L{}^{N8}$	3.544	$\pi_{phen}\cdots\pi_{phen}$ (along [100] direction)	3.585
$\pi_L{}^{N8}\cdots C4_{phen}$ $\pi_L{}^{N8}\cdots H4_{phen}$ $\pi_L{}^{N8}\cdots H4_{phen}–C4_{phen}$	3.602 2.922 131.02	hydrogen bonds involving crystallization EtOH molecules / Å, °	
$\pi_{phen}{}^{N5}\cdots\pi_L{}^{N9}$	3.991	$O1S_{MeOH}\cdots C20_{phen}$ $O1S_{MeOH}\cdots H20_{phen}$ $O1S_{MeOH}\cdots H20_{phen}–C20_{phen}$	3.440 2.575 154.70
$\pi_L{}^{N9}\cdots\pi_L{}^{N11}$	4.032	$O1S_{MeOH}\cdots O7A_{OTf}$ $H1S_{MeOH}\cdots O7A_{OTf}$ $O1S_{MeOH}–H1S_{MeOH}\cdots O7A_{OTf}$	3.165 2.622 125.09
–	–	$C1S_{MeOH}\cdots O9A_{OTf}$ $H1S_{MeOH}\cdots O9A_{OTf}$ $C1_{MeOH}–H1S_{MeOH}\cdots O9A_{OTf}$	3.683 3.116 118.89
–	–	$C2S_{MeOH}\cdots O7A_{OTf}$ $H2S_{MeOH}\cdots O7A_{OTf}$ $C2S_{MeOH}–H2S_{MeOH}\cdots O7A_{OTf}$	3.589 3.167 108.48

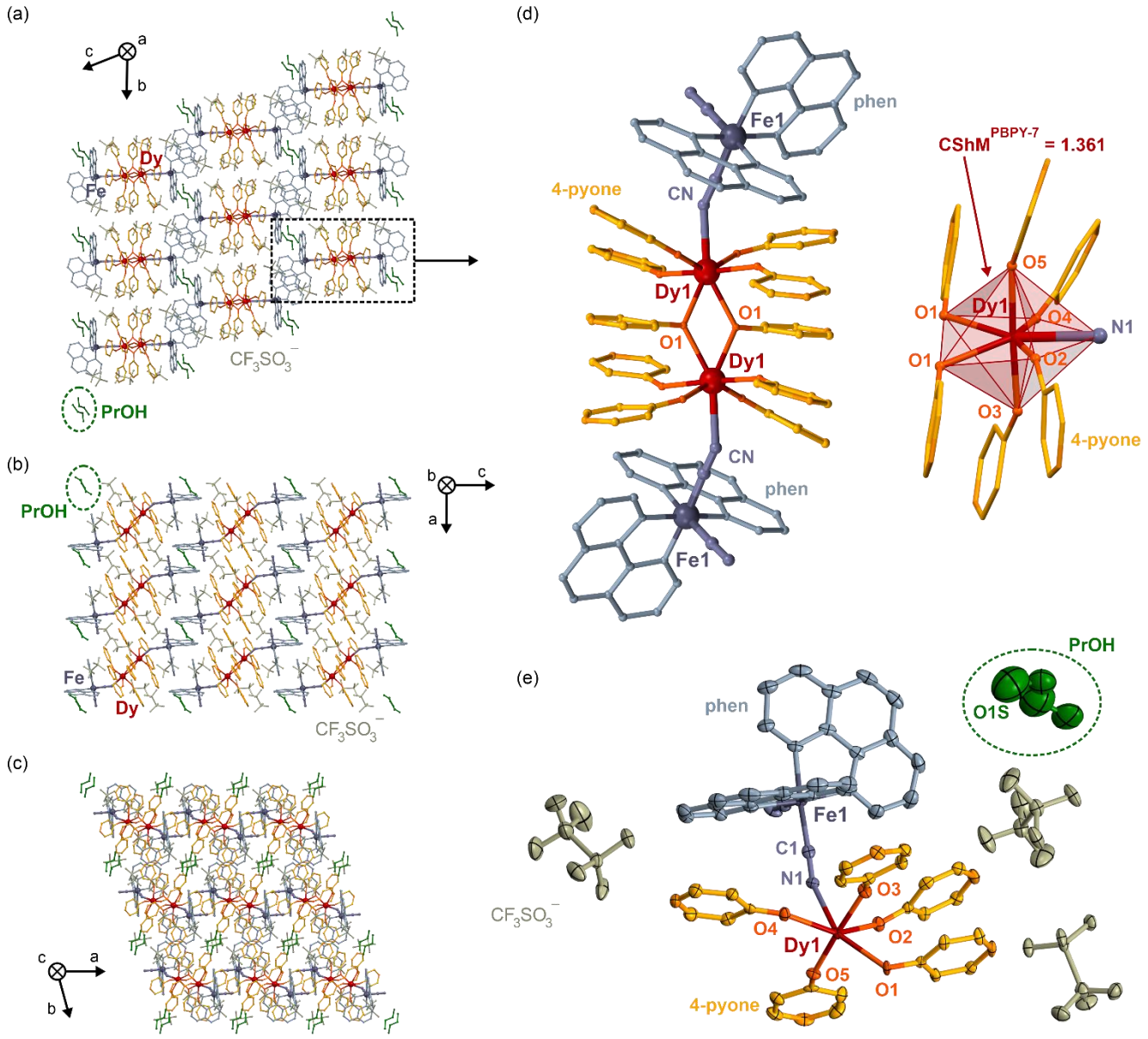

Fig. S8 Detailed structural views of **1·PrOH**: the representative views of the supramolecular network along the crystallographic *a* axis (*a*), *b* axis (*b*), and *c* axis (*c*), the enlarged view of a tetrametallic $\{Dy^{III}_2Fe^{II}_2\}^{6+}$ molecule and the coordination polyhedron of seven-coordinated Dy^{III} complexes (*d*), and the asymmetric unit with the labeling scheme for selected symmetrically independent atoms (*e*). The hydrogen atoms are omitted for clarity. Thermal ellipsoids in (*e*) are presented at the 50% probability level. Detailed structure parameters are gathered in Table S8 (see below).

Table S8 Detailed crystal structure parameters for **1·PrOH**. The labeling scheme is presented in Fig. S8 (see above).

distances in dysprosium(III) and iron(II) complexes / Å					
Dy1–O1	2.401(3)/ 2.407(3)	Dy1–O5	2.227(3)	Fe1–N3	1.970(4)
Dy1–O2	2.281(3)	Dy1–N1	2.482(4)	Fe1–N4	2.004(4)
Dy1–O3	2.226(3)	Fe1–C1	1.902(5)	Fe1–N5	2.002(4)
Dy1–O4	2.275(3)	Fe1–C2	1.898(5)	Fe1–N6	1.969(4)
angles in dysprosium(III) and iron(II) complexes / °					
O1–Dy1–O1	63.58(11)	O3–Dy1–O5	173.12(11)	C2–Fe1–N4	91.77(18)
O1–Dy1–O2	80.89(10)/ 141.10(11)	O3–Dy1–N1	87.29(12)	C2–Fe1–N5	174.62(19)
O1–Dy1–O3	79.60(11)/ 98.75(11)	O4–Dy1–O5	98.46(11)	C2–Fe1–N6	92.45(18)
O1–Dy1–O4	130.88(10)/ 72.49(10)	O4–Dy1–N1	72.78(11)	N3–Fe1–N4	81.79(16)
O1–Dy1–O5	100.21(11)/ 87.22(11)	O5–Dy1–N1	89.84(12)	N3–Fe1–N5	93.71(16)
O1–Dy1–N1	151.41(11)/ 144.28(11)	C1–Fe1–C2	89.42(19)	N3–Fe1–N6	173.33(17)
O2–Dy1–O3	89.34(11)	C1–Fe1–N3	94.38(18)	N4–Fe1–N5	87.61(15)
O2–Dy1–O4	146.29(11)	C1–Fe1–N4	176.02(18)	N4–Fe1–N6	92.70(16)
O2–Dy1–O5	83.85(11)	C1–Fe1–N5	91.56(17)	N5–Fe1–N6	82.25(16)
O2–Dy1–N1	73.61(12)	C1–Fe1–N6	91.04(18)	–	–
O3–Dy1–O4	86.66(11)	C2–Fe1–N3	91.49(18)	–	–

distances and angles between dysprosium(III) and iron(II) centers / Å, °			
within $\{Dy_2Fe_2\}^{6+}$ molecules		between $\{Dy_2Fe_2\}^{6+}$ molecules (the shortest distance)	
Dy1···Dy1	4.095(8)	Dy1···Dy1	9.943(5) (along [100] direction)
Dy1–O1–Dy1	116.44(11)	Fe1···Fe1	8.932(5) (along [$\bar{2}$11] direction)
Dy1···Fe1	5.280(8)	–	–
Dy1–N1–C1	142.55(11)	–	–

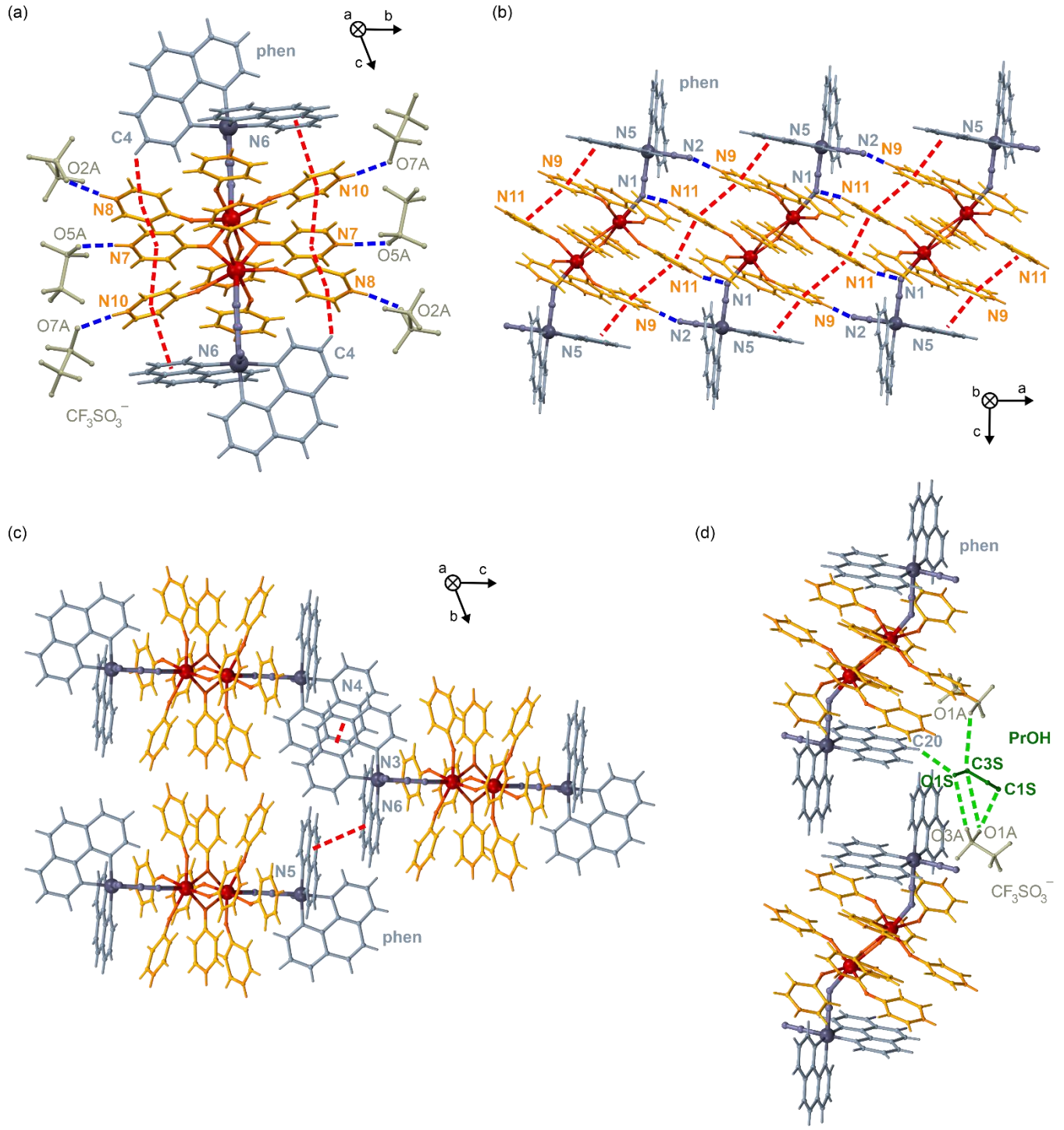

Fig. S9 The visualization of hydrogen bonds involving 4-pyridone ligands and trifluoromethanesulfonate anions or cyanido ligands (blue lines, *a* and *b*), inter- and intramolecular *π*-*π* interactions involving 4-pyridone and phenanthroline ligands (red dashed lines, *a*-*c*), as well as hydrogen bonds engaging solvent 1-PrOH molecules (green dashed lines, *d*) in the crystal structure of **1·PrOH**. The metric parameters of both types of interactions are summarized in Table S9 (see below).

Table S9 Metric parameters for supramolecular interactions in the crystal structure of **1·PrOH**. The labeling scheme is presented in Fig. S9 (see above).

hydrogen bonds between $CF_3SO_3^-$ ions and 4-pyridone ligands / Å, °		hydrogen bonds between cyanido and 4-pyridone ligands / Å, °	
$N7_L\cdots O5A_{OTf}$ $H7_L\cdots O5A_{OTf}$ $N7_L–H7_L\cdots O5A_{OTf}$	2.912 1.941 170.16	$N9_L\cdots N2_{CN}$ $H9_L\cdots N2_{CN}$ $N9_L–H9_L\cdots N2_{CN}$	2.706 1.878 161.29
$N8_L\cdots O2A_{OTf}$ $H8_L\cdots O2A_{OTf}$ $N8_L–H8_L\cdots O2A_{OTf}$	2.807 1.957 168.91	$N11_L\cdots N1_{CN}$ $H11_L\cdots N1_{CN}$ $N11_L–H11_L\cdots N1_{CN}$	3.030 2.258 149.56
$N10_L\cdots O7A_{OTf}$ $H10_L\cdots O7A_{OTf}$ $N10_L–H10_L\cdots O7A_{OTf}$	2.816 1.987 161.61	–	–
π–π interactions within $\{Dy_2Fe_2\}^{6+}$ molecules / Å, °		π–π interactions between $\{Dy_2Fe_2\}^{6+}$ molecules / Å	
$\pi_{phen}^{N6}\cdots\pi_L^{N10}$	3.676	$\pi_L^{N11}\cdots\pi_L^{N11}$	3.547
$\pi_L^{N10}\cdots\pi_L^{N7}$	3.703	$\pi_{phen}\cdots\pi_{phen}$ (along [001] direction)	3.895
$\pi_L^{N7}\cdots\pi_L^{N8}$	3.551	$\pi_{phen}\cdots\pi_{phen}$ (along [100] direction)	3.564
$\pi_L^{N8}\cdots C4_{phen}$ $\pi_L^{N8}\cdots H4_{phen}$ $\pi_L^{N8}\cdots H4_{phen}–C4_{phen}$	3.605 2.927 130.89	–	–
$\pi_{phen}^{N5}\cdots\pi_L^{N9}$	3.999	–	–
$\pi_L^{N9}\cdots\pi_L^{N11}$	4.039	–	–
hydrogen bonds involving crystallization 1-PrOH molecules / Å, ° (*)			
$O1S_{MeOH}\cdots C5_{phen}$ $O1S_{MeOH}\cdots H5_{phen}$ $O1S_{MeOH}\cdots H5_{phen}–C5_{phen}$	4.417 3.632 151.35	$C1S_{MeOH}\cdots O1A_{OTf}$	3.142
$O1S_{MeOH}\cdots C8_{phen}$ $O1S_{MeOH}\cdots H8_{phen}$ $O1S_{MeOH}\cdots H8_{phen}–C8_{phen}$	4.349 3.472 158.05	$C1S_{MeOH}\cdots O3A_{OTf}$	3.617
$O1S_{MeOH}\cdots C17_{phen}$ $O1S_{MeOH}\cdots H17_{phen}$ $O1S_{MeOH}\cdots H17_{phen}–C17_{phen}$	3.884 2.957 174.97	$C2S_{MeOH}\cdots O3A_{OTf}$	3.319
$O1S_{MeOH}\cdots C20_{phen}$ $O1S_{MeOH}\cdots H20_{phen}$ $O1S_{MeOH}\cdots H20_{phen}–C20_{phen}$	4.833 4.153 132.75	$C3S_{MeOH}\cdots O1A_{OTf}$	3.812
$O1S_{MeOH}\cdots O1A_{OTf}$	4.142	$C3S_{MeOH}\cdots O3A_{OTf}$	3.847
$O1S_{MeOH}\cdots O3A_{OTf}$	3.634	–	–

*Because of the disorder of solvent molecules of crystallization, the hydrogen atoms at related C and O atoms were omitted in the refinement procedure (see the experimental section). For this reason, the table contains only information about the distances between the hydrogen bond donor and acceptor (involving the alcohol solvent molecules).

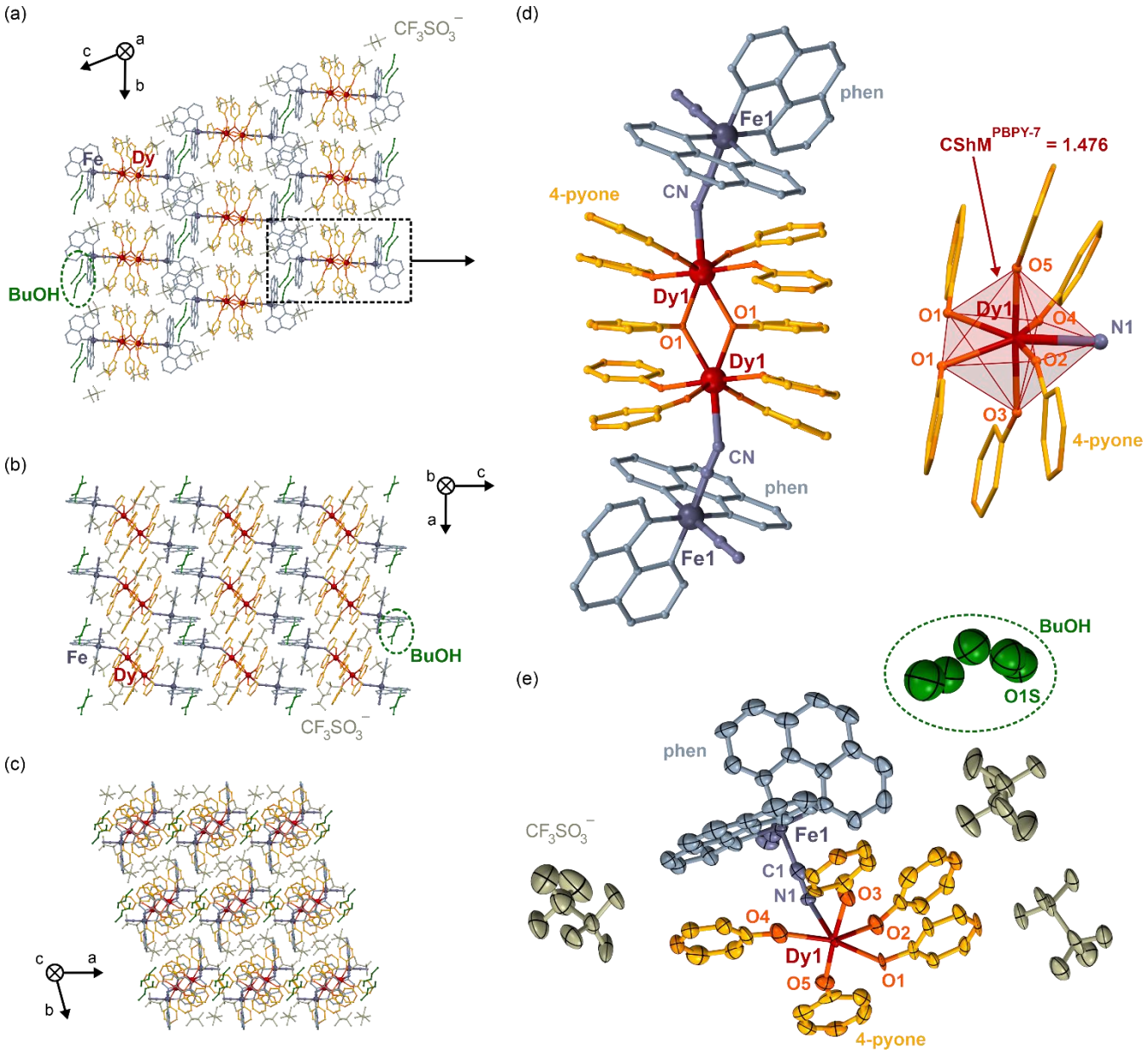

Fig. S10 Detailed structural views of **1·BuOH**: the representative views of the supramolecular network along the crystallographic *a* axis (*a*), *b* axis (*b*), and *c* axis (*c*), the enlarged view of a tetrametallic $\{Dy^{III}_2Fe^{II}_2\}^{6+}$ molecule and the coordination polyhedron of seven-coordinated Dy^{III} complexes (*d*), and the asymmetric unit with the labeling scheme for selected symmetrically independent atoms (*e*). The hydrogen atoms are omitted for clarity. Thermal ellipsoids in (*e*) are presented at the 50% probability level. Detailed structure parameters are gathered in Table S10 (see below).

Table S10 Detailed crystal structure parameters for **1·BuOH**. The labeling scheme is presented in Fig. S10 (see above).

distances in dysprosium(III) and iron(II) complexes / Å					
Dy1–O1	2.399(6)/ 2.403(6)	Dy1–O5	2.228(4)	Fe1–N3	1.977(9)
Dy1–O2	2.278(7)	Dy1–N1	2.459(9)	Fe1–N4	2.007(10)
Dy1–O3	2.238(4)	Fe1–C1	1.921(14)	Fe1–N5	2.008(10)
Dy1–O4	2.272(9)	Fe1–C2	1.895(12)	Fe1–N6	1.977(10)
angles in dysprosium(III) and iron(II) complexes / °					
O1–Dy1–O1	63.6(2)	O3–Dy1–O5	173.5(2)	C2–Fe1–N4	174.9(5)
O1–Dy1–O2	139.8(3)/ 80.4(3)	O3–Dy1–N1	87.0(3)	C2–Fe1–N5	91.4(4)
O1–Dy1–O3	99.7(3)/ 78.6(3)	O4–Dy1–O5	98.4(3)	C2–Fe1–N6	91.6(4)
O1–Dy1–O4	72.7(3)/ 130.1(3)	O4–Dy1–N1	74.1(3)	N3–Fe1–N4	82.8(4)
O1–Dy1–O5	85.8(3)/ 90.3(3)	O5–Dy1–N1	101.1(3)	N3–Fe1–N5	92.8(4)
O1–Dy1–N1	145.6(2)/ 150.1(2)	C1–Fe1–C2	89.2(5)	N3–Fe1–N6	173.5(4)
O2–Dy1–O3	89.5(3)	C1–Fe1–N3	91.2(4)	N4–Fe1–N5	88.3(4)
O2–Dy1–O4	147.4(3)	C1–Fe1–N4	91.5(4)	N4–Fe1–N6	93.4(4)
O2–Dy1–O5	84.1(3)	C1–Fe1–N5	176.0(4)	N5–Fe1–N6	81.8(4)
O2–Dy1–N1	73.3(3)	C1–Fe1–N6	94.2(5)	–	–
O3–Dy1–O4	86.5(3)	C2–Fe1–N3	92.2(4)	–	–

distances and angles between dysprosium(III) and iron(II) centerss / Å, °			
within $\{Dy_2Fe_2\}^{6+}$ molecules		between $\{Dy_2Fe_2\}^{6+}$ molecules (the shortest distance)	
Dy1···Dy1	4.081(19)	Dy1···Dy1	9.886(5) (along [100] direction)
Dy1–O1–Dy1	116.42(3)	Fe1···Fe1	8.980(5) (along $[1\bar{2}1]$ direction)
Dy1···Fe1	5.273(19)	–	–
Dy1–N1–C1	142.17(3)	–	–

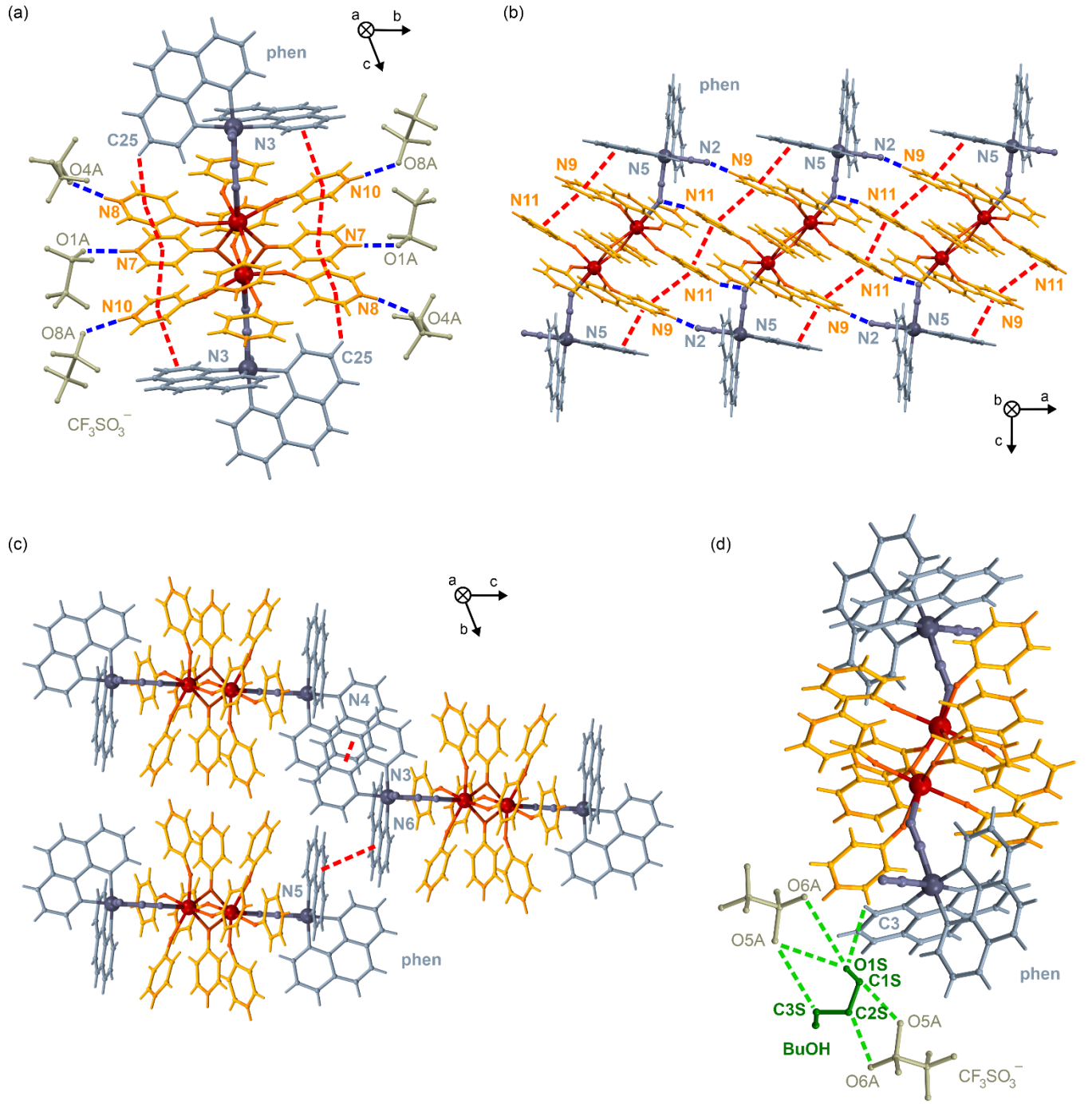

Fig. S11 The visualization of hydrogen bonds involving 4-pyridone ligands and trifluoromethanesulfonate anions or cyanido ligands (blue lines, *a* and *b*), inter- and intramolecular *π*-*π* interactions involving 4-pyridone and phenanthroline ligands (red dashed lines, *a*-*c*), as well as hydrogen bonds engaging solvent 1-BuOH molecules (green dashed lines, *d*) in the crystal structure of **1·BuOH**. The metric parameters of both types of interactions are summarized in Table S11 (see below).

Table S11 Metric parameters for supramolecular interactions in the crystal structure of **1·BuOH**. The labeling scheme is presented in Fig. S11 (see above).

hydrogen bonds between $CF_3SO_3^-$ ions and 4-pyridone ligands / Å, °		hydrogen bonds between cyanido and 4-pyridone ligands / Å, °	
$N7_L\cdots O1A_{OTf}$ $H7_L\cdots O1A_{OTf}$ $N7_L–H7_L\cdots O1A_{OTf}$	2.782 1.927 172.38	$N9_L\cdots N2_{CN}$ $H9_L\cdots N2_{CN}$ $N9_L–H9_L\cdots N2_{CN}$	2.700 1.859 165.47
$N8_L\cdots O4A_{OTf}$ $H8_L\cdots O4A_{OTf}$ $N8_L–H8_L\cdots O4A_{OTf}$	2.826 1.976 169.33	$N11_L\cdots N1_{CN}$ $H11_L\cdots N1_{CN}$ $N11_L–H11_L\cdots N1_{CN}$	3.009 2.208 154.77
$N10_L\cdots O8A_{OTf}$ $H10_L\cdots O8A_{OTf}$ $N10_L–H10_L\cdots O8A_{OTf}$	2.820 1.982 164.62	–	–
π–π interactions within $\{Dy_2Fe_2\}^{6+}$ molecules / Å, °		π–π interactions between $\{Dy_2Fe_2\}^{6+}$ molecules / Å	
$\pi_{phen}{}^{N3}\cdots\pi_L{}^{N10}$	3.681	$\pi_L{}^{N11}\cdots\pi_L{}^{N11}$	3.512
$\pi_L{}^{N10}\cdots\pi_L{}^{N7}$	3.674	$\pi_{phen}\cdots\pi_{phen}$ (along [001] direction)	3.938
$\pi_L{}^{N7}\cdots\pi_L{}^{N8}$	3.552	$\pi_{phen}\cdots\pi_{phen}$ (along [100] direction)	3.570
$\pi_L{}^{N8}\cdots C25_{phen}$ $\pi_L{}^{N8}\cdots H25_{phen}$ $\pi_L{}^{N8}\cdots H25_{phen}–C25_{phen}$	3.640 2.967 130.53	–	–
$\pi_{phen}{}^{N5}\cdots\pi_L{}^{N9}$	3.987	–	–
$\pi_L{}^{N9}\cdots\pi_L{}^{N11}$	4.022	–	–
hydrogen bonds involving crystallization 1-BuOH molecules / Å, ° (*)			
$O1S_{MeOH}\cdots C3_{phen}$	4.009	$C1S_{MeOH}\cdots O6A_{OTf}$	4.083
$O1S_{MeOH}\cdots O5A_{OTf}$	3.630/4.336	$C2S_{MeOH}\cdots O5A_{OTf}$	3.670
$O1S_{MeOH}\cdots O6A_{OTf}$	4.486/4.102	$C2S_{MeOH}\cdots O6A_{OTf}$	3.268
$C1S_{MeOH}\cdots O5A_{OTf}$	3.510	$C3S_{MeOH}\cdots O5A_{OTf}$	3.697

*Because of the disorder of solvent molecules of crystallization, the hydrogen atoms at related C and O atoms were omitted in the refinement procedure (see the experimental section). For this reason, the table contains only information about the distances between the hydrogen bond donor and acceptor (involving the alcohol solvent molecules).

Table S12 Results of Continuous Shape Measure (CShM) analysis for six-coordinated iron(II) and seven-coordinated dysprosium(III) complexes in the crystal structures of **1**, **1·MeOH**, **1·EtOH**, **1·PrOH**, and **1·BuOH**.[S1,S2]

compound	CShM parameters (*) for six-coordinated Fe(II) complexes, *cis*−$[Fe^{II}(\mu-CN)_2(phen)_2]$			
	HP-6	PPY-6	OC-6	TPR-6
1	30.075	27.527	**0.317**	14.956
1·MeOH	30.086	27.747	**0.308**	14.957
1·EtOH	30.150	27.730	**0.299**	15.124
1·PrOH	30.207	27.875	**0.298**	15.274
1·BuOH	30.434	28.087	**0.286**	15.364

compound	CShM parameters (*) for seven-coordinated Dy(III) complexes, $[Dy^{III}(\mu-NC)(4\text{-pyone})_6]^{2+}$				
	HP-7	HPY-7	PBPY-7	COC-7	CTPR-7
1	32.804	23.329	**1.288**	4.495	3.785
1·MeOH	32.717	23.395	**1.344**	4.403	3.692
1·EtOH	32.866	23.685	**1.353**	4.424	3.587
1·PrOH	32.831	23.680	**1.361**	4.401	3.569
1·BuOH	32.760	23.946	**1.476**	4.115	3.200

compound	CShM parameters (*) for the five-coordinated equatorial plane of the coordination polyhedra of Dy(III) complexes, the $[Dy^{III}(\mu-NC)(4\text{-pyone})_4]^{2+}$ part (see Fig. 1b and S12c)			
	PP-5	vOC-5	TBPY-5	SPY-5
1	**1.384**	24.179	28.955	24.799
1·MeOH	**1.461**	23.906	28.659	24.510
1·EtOH	**1.511**	23.909	28.336	24.478
1·PrOH	**1.535**	23.967	28.398	24.547
1·BuOH	**1.718**	23.184	27.326	23.702

*CShM parameters for six- and seven-coordinated complexes: [S1,S2]

for six-coordinated complexes:

CShM HP-6 – the parameter related to the hexagon geometry (D_{6h} symmetry)
CShM PPY-6 – the parameter related to the pentagonal pyramid geometry (C_{5v} symmetry)
CShM OC-6 – the parameter related to the octahedron geometry (O_h symmetry)
CShM TPR-6 – the parameter related to the trigonal prism geometry (D_{3h} symmetry)

for seven-coordinated complexes:

CShM HP-7 – the parameter related to the heptagon geometry (D_{7h} symmetry)
CShM HPY-7 – the parameter related to the hexagonal pyramid geometry (C_{6v} symmetry)
CShM PBPY-7 – the parameter related to the pentagonal bipyramid geometry (D_{5h} symmetry)
CShM COC-7 – the parameter related to the capped octahedron geometry (C_{3v} symmetry)
CShM CTPR-7 – the parameter related to the capped trigonal prism geometry (C_{2v} symmetry)

for five-coordinated complexes:

CShM HP-5 – the parameter related to the pentagon geometry (D_{5h} symmetry)
CShM HPY-5 – the parameter related to the vacant octahedron geometry (C_{4V} symmetry)
CShM PBPY-5 – the parameter related to the trigonal bipyramid geometry (D_{3h} symmetry)
CShM COC-5 – the parameter related to the square pyramid geometry (C_{4V} symmetry)

The value of CShM = 0 is ascribed to an ideal geometry. The increase of the CShM parameter above 0 represents the increasing distortion from an ideal polyhedron.

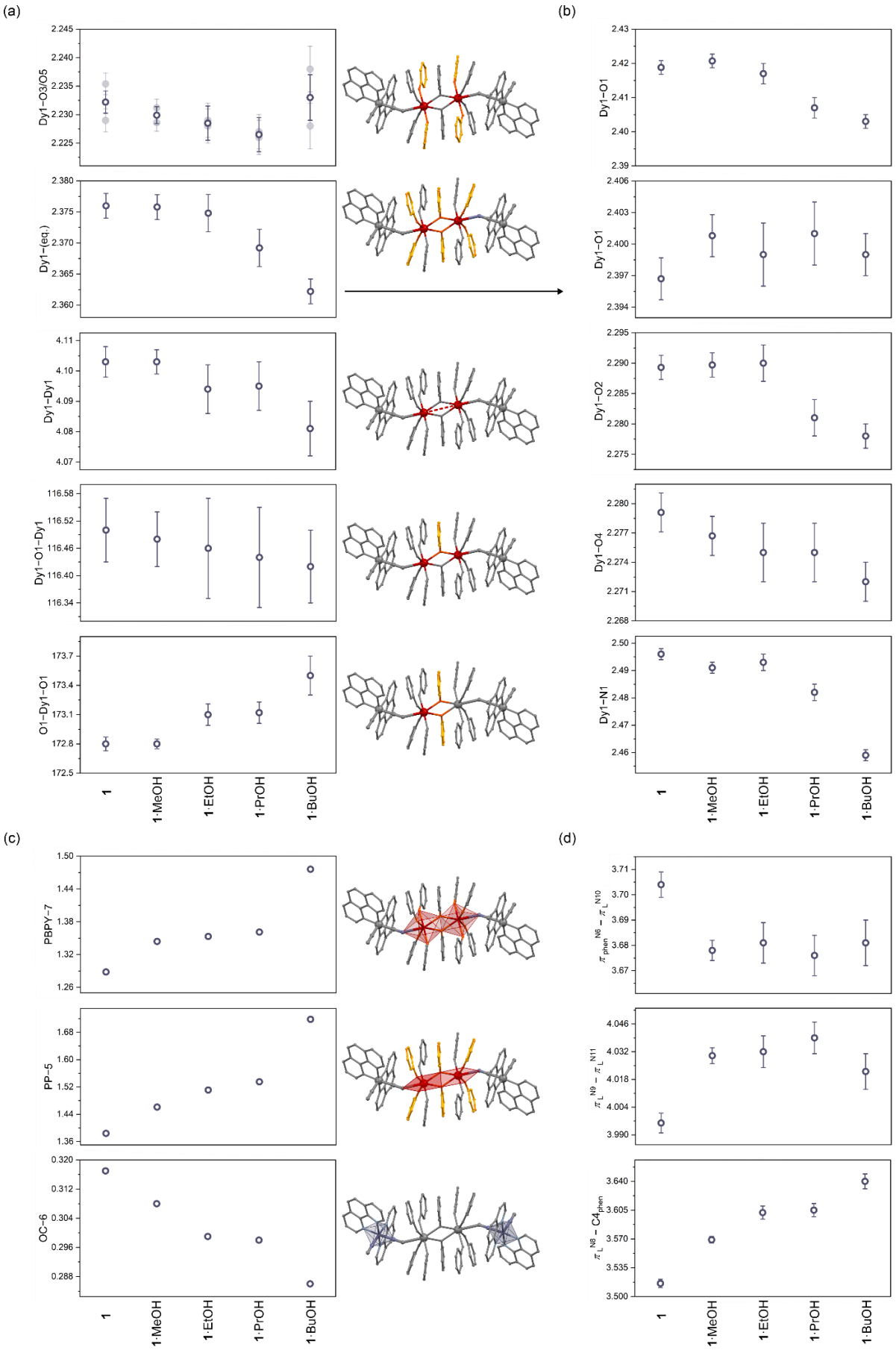

Fig. S12 Comparison of selected distances in a tetrametallic $\{Dy^{III}_2Fe^{II}_2\}^{6+}$ molecule and the coordination polyhedron of Dy(III) complexes (*a*, *b*; Tables S2, S4, S6, S8, and S10), CShM parameters for Fe(II) and Dy(III) complexes (*c*; Table S12), and selected distances of supramolecular interactions (*d*; Tables S3, S5, S7, S9, and S11) in the structure of **1**, **1·MeOH**, **1·EtOH**, **1·PrOH**, and **1·BuOH**. Structural visualization is presented using the example of **1** (central panel).

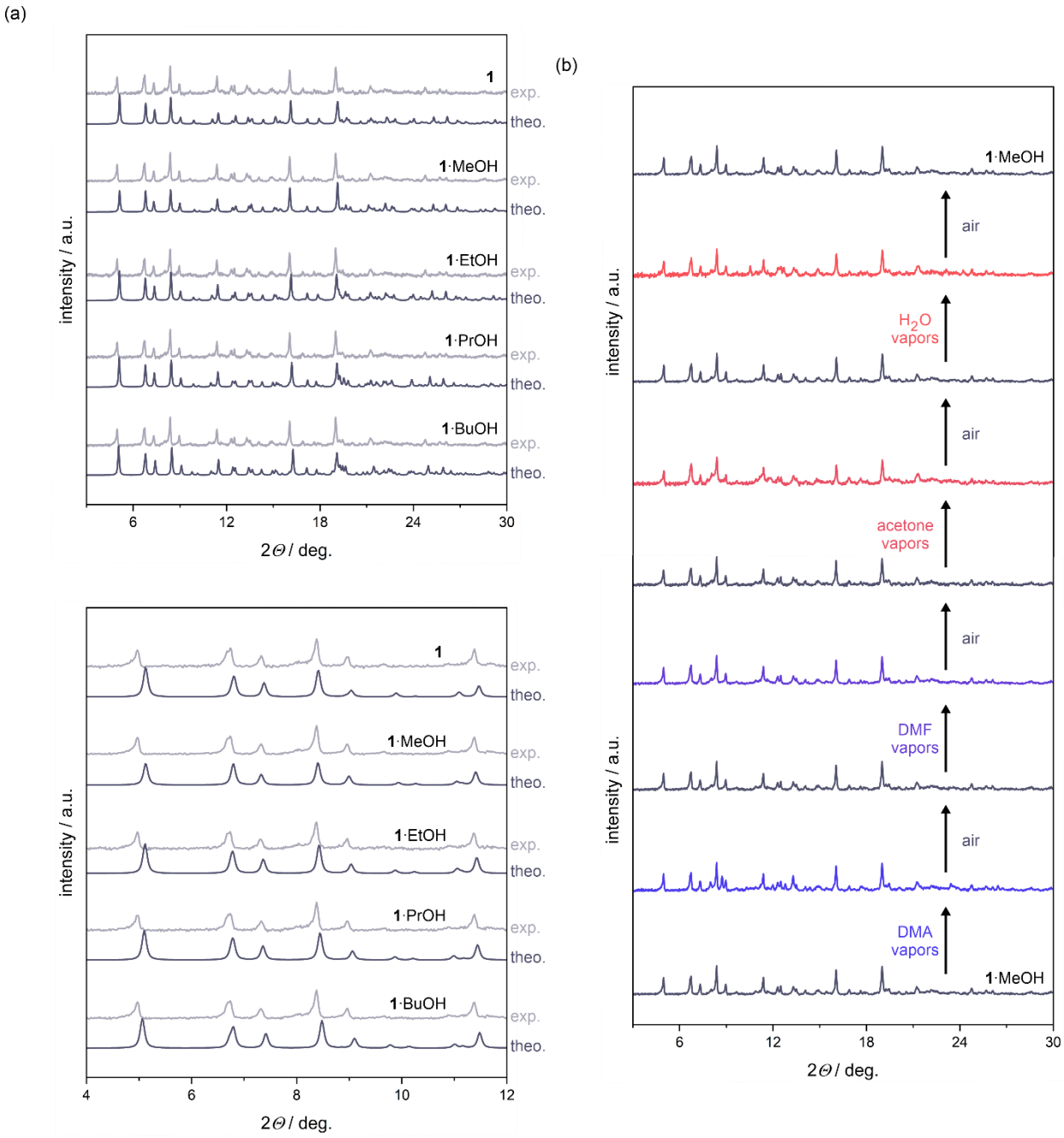

Fig. S13 The comparison of experimental (T = 300 K) and calculated powder X-ray diffraction (P-XRD) patterns of **1**, **1·MeOH**, **1·EtOH**, **1·PrOH**, and **1·BuOH**, presented both in the broad 2Θ range of 3–30° as well as in the limited low angle region of 4–12° (*a*) and the experimental room-temperature P-XRD patterns obtained for the polycrystalline sample of **1·MeOH** exposed to various solvent vapors and air (for details see Fig. S16). Experimental data in (*a*) were compared with the P-XRD patterns calculated from the respective structural models obtained from the single-crystal X-ray diffraction (SC-XRD) structural analyses (T = 100 K, Table S1).

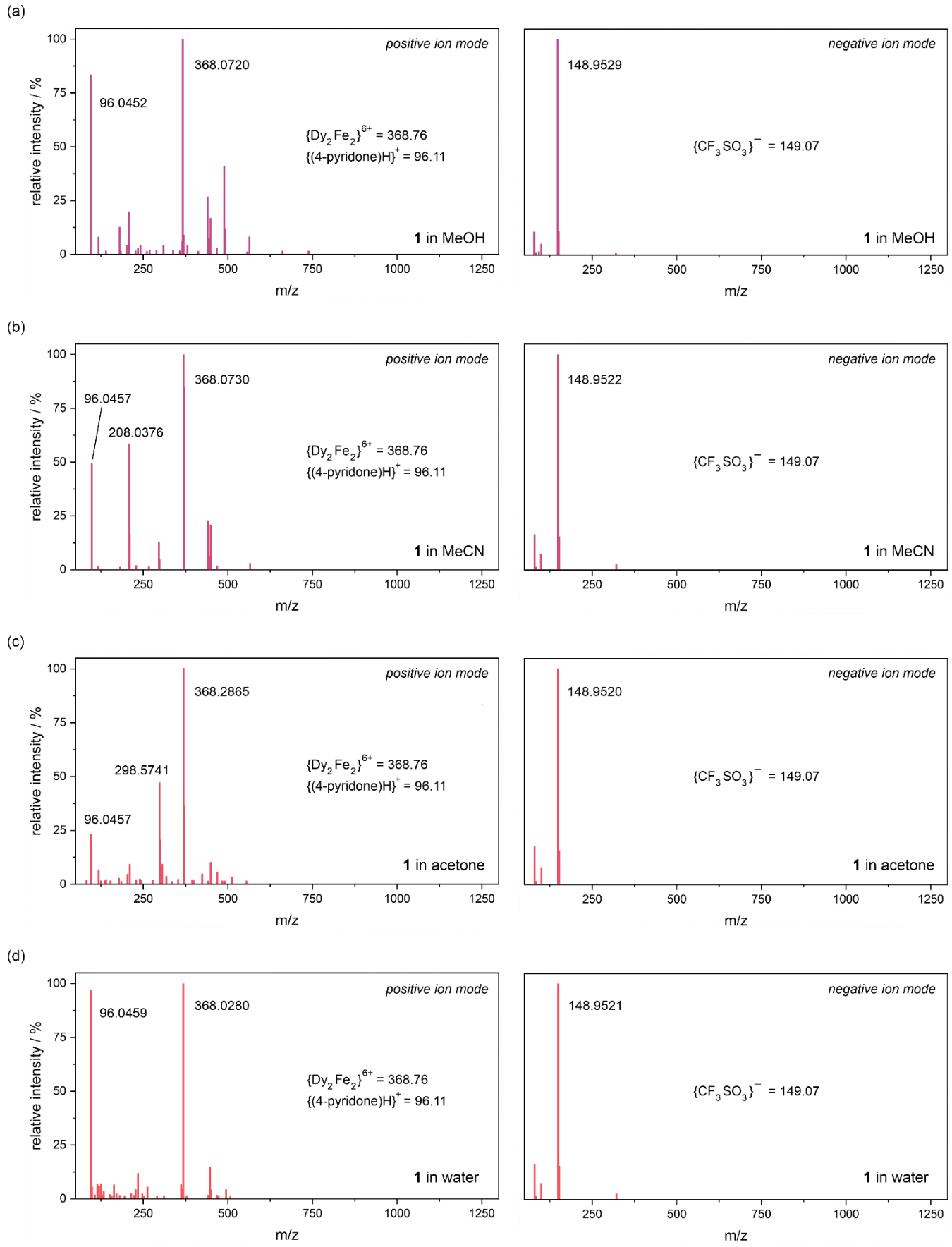

Fig. S14 The electrospray ionization mass spectra (ESI-MS) of **1** in methanol (*a*), acetonitrile (*b*), acetone (*c*), and water (*d*) in positive (left panel) and negative (right panel) ion modes. Only signals above the 1% of relative intensity are marked. The m/z values of the most intense peaks and the theoretical values of selected molecules are marked. Selected spectral parameters of the most intense peaks are summarized in Table S13 (see below), while the interpretation for selected ones is described in the comment provided below Table S13.

Table S13 Selected spectral parameters of the most intense peaks of electrospray ionization mass spectra (ESI-MS) of **1** in methanol, acetonitrile, acetone, and water in positive and negative ion modes (see Fig. S14 above).

m/z	relative intensity / %	full width at half maximum	m/z	relative intensity / %	full width at half maximum
positive ion mode			negative ion mode		
1 in methanol					
96.0452	83.6	0.0042	79.9572	10.5	0.0038
181.0771	12.6	0.0060	94.0297	1.2	0.0044
208.0372	19.8	0.0062	98.9555	4.9	0.0043
368.0720	100.0	0.0074	148.9529	100	0.0110
368.5735	42.8	0.0075	149.0427	1.6	0.0149
369.0748	9.1	0.0082	149.1060	1.6	0.0180
442.0767	26.8	0.0096	149.2370	0.9	0.0192
448.0635	16.9	0.0100	149.3426	2.3	0.0051
491.1698	41.1	0.0100	149.9543	3.4	0.0075
492.0724	12.1	0.0114	150.9484	10.6	0.0053
1 in acetonitrile					
96.0457	49.3	0.0041	79.9566	16.2	0.0037
208.0376	58.6	0.0062	98.9548	7.3	0.0043
208.5391	16.7	0.0062	148.9522	100	0.0126
297.0747	12.9	0.0076	149.0080	1.3	0.0090
368.6730	100.0	0.0154	149.0417	2.3	0.0144
368.8740	85.3	0.0078	149.1050	2	0.0175
369.0752	19.0	0.0077	149.3421	3.3	0.0052
442.0770	22.8	0.0095	149.9533	4.8	0.0068
443.0796	6.4	0.0107	150.9472	15.3	0.0053
448.0637	20.7	0.0096	320.8917	2.4	0.0094
1 in acetone					
96.0457	23	0.0042	79.9564	17.5	0.0037
118.0278	6.2	0.0047	98.9547	7.8	0.0043
208.0379	9	0.0062	148.9520	100.0	0.0126
298.0726	47	0.0074	149.0078	1.4	0.0089
298.2741	20.5	0.0076	149.0415	2.4	0.0144
304.2630	9	0.0081	149.1048	2.0	0.0174
368.4865	100	0.0136	149.1567	1.3	0.0207
369.5895	36.6	0.0068	149.3419	3.4	0.0052
448.0638	9.9	0.0102	149.9531	4.9	0.0068
467.3728	5.3	0.0113	150.9471	15.5	0.0053

1 in water					
96.0459	96.6	0.0041	79.9565	16.9	0.0037
97.0491	5.6	0.0045	98.9548	7.6	0.0043
115.0198	6.7	0.0046	148.9521	100.0	0.0126
119.0312	5.8	0.0051	149.0079	1.4	0.0090
124.0251	6.8	0.0048	149.0416	2.4	0.0144
162.5387	6.3	0.0057	149.1049	2.0	0.0175
234.2086	11.6	0.0077	149.2890	2.3	0.0132
368.5280	100.0	0.0046	149.6476	4.1	0.0060
448.0648	14.4	0.0025	150.4502	10.1	0.0061
491.1711	13.0	0.0140	235.9194	9.0	0.0074

Comment to Fig. S14 and Table S13: The ESI(-)–MS spectra of **1** in all tested solvents are quite similar. The most intense peak at m/z of ca. 148.95 corresponds well to the detection of trifluoromethanesulfonate, $\{CF_3SO_3\}^-$, anions (149.07). Additionally, in each of the spectra, there are small peaks at m/z of 79.96 and 98.95, which presumably corresponds to $\{SO_3\}^-$ (80.06) and $\{SO_3F\}^-$ (99.07), resulting from the fragmentation of $\{CF_3SO_3\}^-$ anions. The spectra collected in positive ionization mode are much more complicated. The peak at m/z of 96.05, which are present in all solvents, is associated with the presence of a protonated form of 4-pyridone ligand, $\{(4\text{-pyridone})H\}^+$ (96.10). In all experiments, the most intense peak at ca. 368.7 is associated with the charged tetrametallic $\{Dy^{III}_2Fe^{II}_2\}^{6+}$ molecular unit or its fragmentation ion. The theoretical value of the whole molecule, $\{[Dy(4\text{-pyone})_5]_2[Fe(CN)_2(phen)_2]_2\}^{6+}$, is 368.76, which matches perfectly with the experimental values. After the theoretical fragmentation of this molecule, the generated vacant coordination sites would be filled by solvent molecules. The theoretical m/z values of the considered (largest possible) fragments, e.g. $\{[Dy(4\text{-pyone})_4(MeOH)][Fe(CN)_2(phen)_2]\}^{3+}$, $\{[Dy(4\text{-pyone})_4(MeOH)_2][Fe(CN)_2(phen)_2]\}^{3+}$, $\{[Dy(4\text{-pyone})_5(MeOH)][Fe(CN)_2(phen)_2]\}^{3+}$, $\{[Dy(4\text{-pyone})_5(MeOH)_2][Fe(CN)_2(phen)_2]\}^{3+}$ and $\{[Dy(4\text{-pyone})_6][Fe(CN)_2(phen)_2]\}^{3+}$ in MeOH, are 347.74, 358.42, 379.44, 390.12 and 400.46, respectively, which are significantly different from the observed value. A more rich fragmentation of the molecule would lead to the formation of fragments with significantly different m/z values. On the other hand, this peak appears in every investigated solvent, therefore it cannot be related to the base peak. Moreover, the presented compounds can be repeatedly recrystallized from several solvents (see the experimental section in the main manuscript) which proves, that the whole tetrametallic $\{Dy^{III}_2Fe^{II}_2\}^{6+}$ molecule is stable after being transferred into the liquid solution, and the most intense peak in the MS spectrum comes from the presence of this molecule. In addition, depending on the solvent, the spectra differ in the presence of additional peaks with lower intensities. In MeOH and MeCN, the peak at m/z of 208.04 corresponds likely to the presence of $\{Fe(phen)_2\}^{2+}$ (208.09) ion, while peak at m/z of 442.08 corresponds to $\{Fe(CN)(phen)_2\}^+$ (442.17) or $\{[Dy(4\text{-pyone})_6(CF_3SO_3)\}^+$ (441.97) ions. In acetone, the peak at 298.27 corresponds to the presence of $\{Fe(phen)_3\}^{2+}$ (298.23) ion. Additionally, in MeOH and water, the peak at m/z of 491.17 may be assigned to $\{Fe(CN)_2(phen)_2+Na\}^+$ (491.28) adduct. All these signals indicate that the $\{Dy^{III}_2Fe^{II}_2\}^{6+}$ molecule is fragmented in these experimental conditions, but detection of the peak at m/z of 368 indicates its presence in the solution. All these signals are consistent with literature values.[S3–S5]

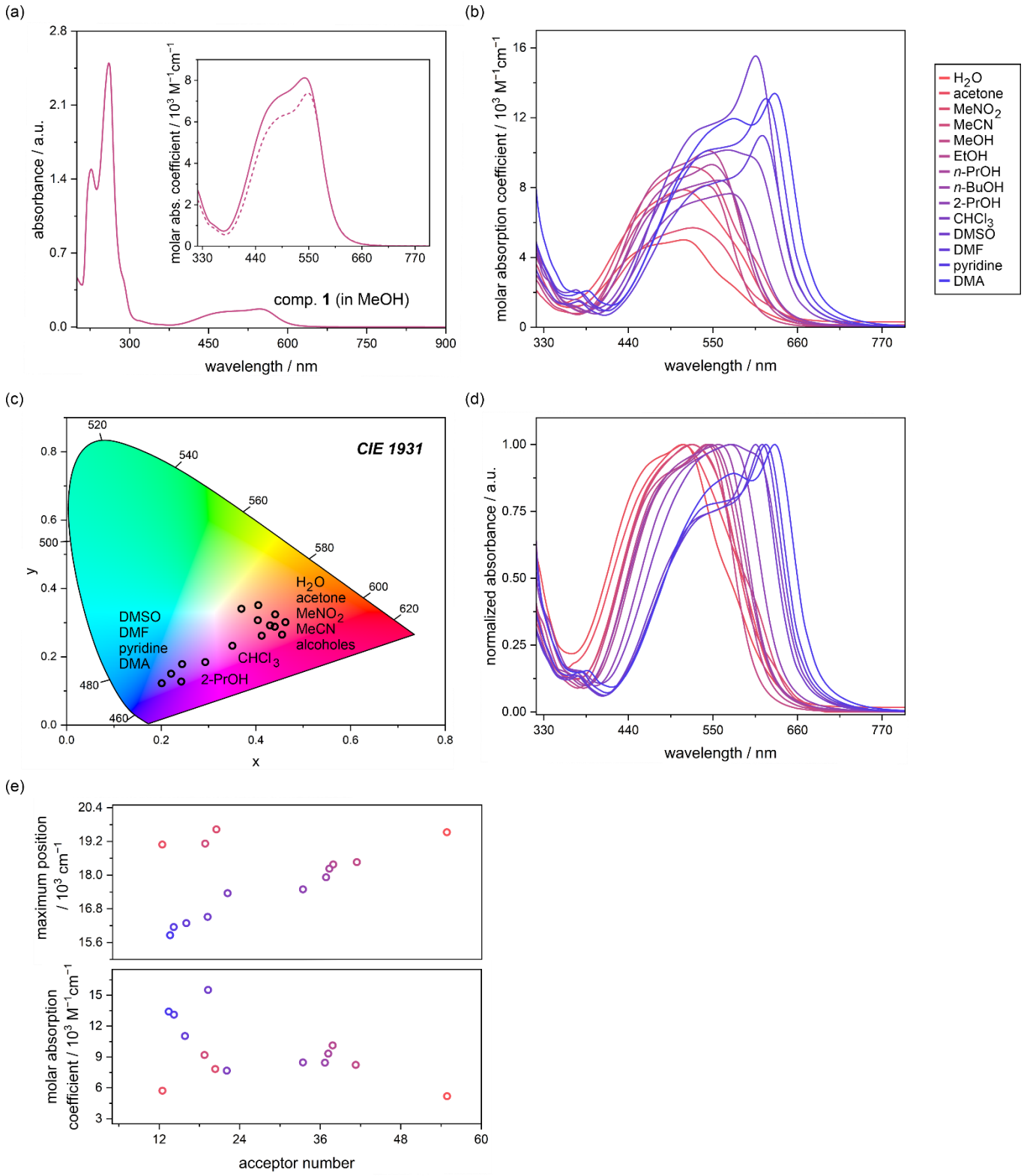

Fig. S15 Solvatochromic properties of **1** in solution: the UV-vis absorption spectrum of **1** (solid lines) dissolved in MeOH (*a*), shown with the comparison with the spectrum of $[Fe(CN)_2(phen)_2]$ precursor (dashed line, the inset), the UV-vis absorption spectra and the corresponding solution colors (shown on the CIE 1931 chromaticity diagram) for the crystals of **1** dissolved in various indicated solvents (the $1{\cdot}10^{-4}$ M solutions; *b*, *c*), and the normalized electronic spectra of the crystals of **1** dissolved in different solvents, followed by the dependences of the absorption maximum position and molar absorption coefficient on the acceptor number of the solvent (*d*, *e*).[S6] Selected spectral parameters related to the presented solvatochromism of **1** are summarized in Table S14.

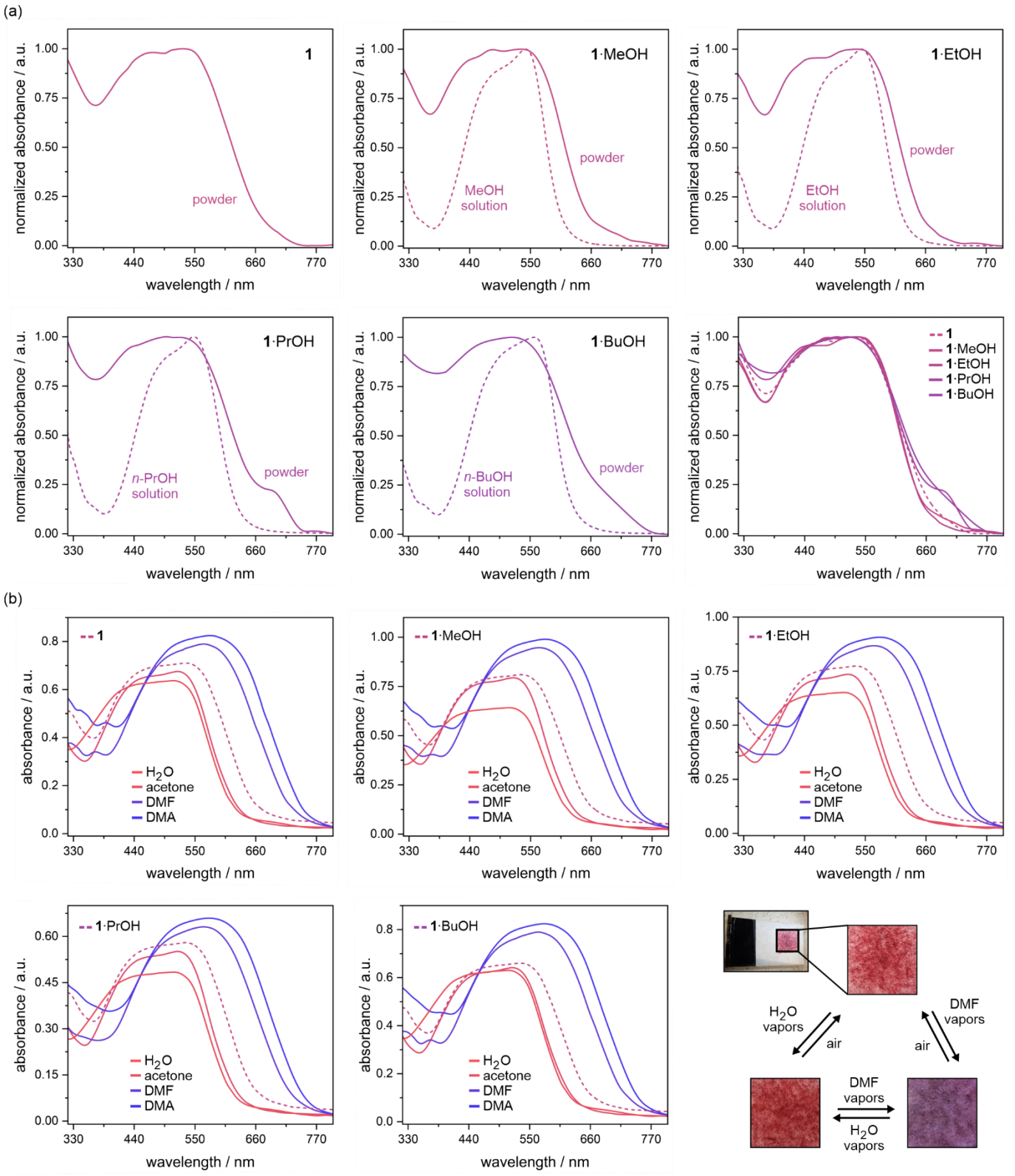

Fig. S16 The solid-state UV-vis absorption spectra of **1**, **1·MeOH**, **1·EtOH**, **1·PrOH**, and **1·BuOH**, including the comparison of their solid-state absorption spectra with the spectra of the respective solutions obtained by dissolving the crystals of the indicated compounds in the appropriate alcohols which are present in the crystal structure (*a*), and the changes in solid-state UV-vis absorption spectra for the crystalline samples of all presented compounds exposed to selected solvent vapors (*b*). Part *b* shows photos of the solid-state solvatochromic effect for the crystals of **1**, exposed to DMF and water vapors and air. Selected spectral parameters are summarized in Table S14 (see below).

Comment on the timescale of solvatochromic and vapochromic effects for 1:

Compounds **1**, as well as **1·alcohol**, are perfectly soluble in water and most typical organic solvents such as acetone, MeCN, simple alcohols, DMSO, or DMF, so the effect of changing the color of the solution after dissolution (solvatochromic effect), is, of course, immediate and permanent.

After evaporation of the solvent, the presented coordination compound can be either recovered in the microcrystalline form of **1** or, in the case of alcoholic solutions, with co-crystallizing solvent molecules as **1·alcohol**. During the exposition of crystal of **1** or **1·alcohol** to solvent vapors (a vapochromic effect), the color change effect is observed within a few minutes (the greater the color change, the faster the effect can be observed with the naked eye, e.g., for DMF in less than 1 minute), and its full saturation usually occurs after several minutes (the spectra that were measured after less than 10 min were a mixture of absorption observed as one very broad band).

The color saturation time after exposure to solvent vapors depends on its volatility (the more volatile the solvent, the faster its interaction with the crystals of the compound). For the least volatile ones, this process may take up to (for the full saturation) 30 minutes, however, the saturation also depends on the fineness of the crystals. All measurements we performed were made on a sample exposed to solvents for at least 60 minutes to ensure the complete process. Regarding the persistence of color after removing the crystals from the atmosphere of solvent vapors, it is analogous, that for volatile solvents the effect of returning to the original phase occurs faster than for less volatile ones (up to 30 minutes). In any case, the color persists long enough to allow the experiment to be carried out after removing the solvent from the atmosphere.

Table S14 Selected spectral parameters of the lowest-energy absorption band in the UV-vis absorption spectra of **1** dissolved in different solvents (Fig. S15) and the solid-state UV-vis absorption spectra of **1**, **1·MeOH**, **1·EtOH**, **1·PrOH**, and **1·BuOH** exposed to selected solvent vapors (Fig. S16).

parameters of UV-vis absorption spectra of **1** dissolved in various indicated solvents (Fig. S15), compared with the acceptor number of investigated solvents			
solvent	λ / nm	ε / 10^3 $dm^3mol^{-1}cm^{-1}$	acceptor no.
water	512.0	5.1	54.8
nitromethane	510.3	7.9	20.5
acetonitrile	522.0	9.2	18.9
acetone	524.0	5.7	12.5
ethanol	544.9	10.1	37.9
1-propanol	548.2	9.3	37.3
methanol	541.5	8.1	41.5
1-butanol	557.5	8.4	36.8
2-propanol	572.2	8.4	33.5
trichloromethane ($CHCl_3$)	577.0	7.7	22.1
dimethyl sulfoxide (DMSO)	605.5	15.5	19.3
N,*N*-dimethylformamide (DMF)	613.0	11.0	16.0
pyridine	619.0	13.1	14.2
N,*N*-dimethylacetamide (DMA)	630.7	13.4	13.6

wavelength positions of the lowest-energy absorption band on the solid-state UV-vis absorption spectra of indicated compounds exposed to selected solvent vapors (Fig. S16) / nm					
compound	on the air (as-synthesized)	water	acetone	*N*,*N*-dimethyl-formamide (DMF)	*N*,*N*-dimethyl-acetamide (DMA)
1	530.1	511.1	518.1	570.5	590.1
1·MeOH	532.2	511.2	519.3	571.8	589.6
1·EtOH	534.4	511.0	517.9	572.1	592.4
1·PrOH	528.9	511.2	518.5	569.3	589.4
1·BuOH	533.2	511.5	518.0	571.7	591.4

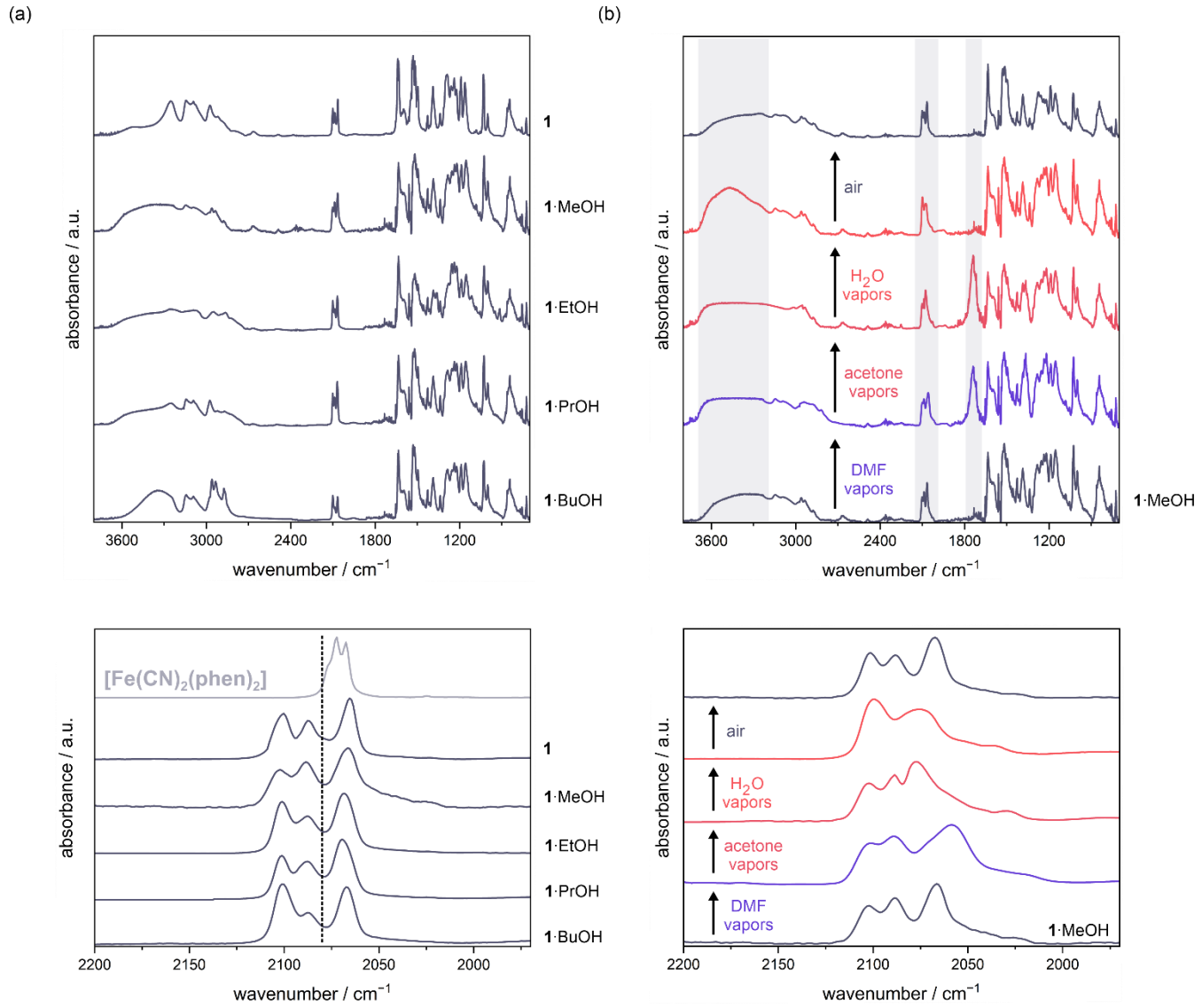

Fig. S17 Infrared (IR) absorption spectra of **1**, **1·MeOH**, **1·EtOH**, **1·PrOH**, and **1·BuOH** in the full 3800–700 cm^{-1} range (top) and the 2200–1980 cm^{-1} range of the stretching vibrations of cyanido ligands (bottom) compared with the spectrum of $[Fe^{II}(CN)_2(phen)_2]$ precursor (*a*), and the infrared absorption spectra of **1·MeOH** obtained after the exposition of the air-dried sample to various solvent vapors and back to air (for details see Fig. S16) (*b*). In the (b) part, the spectra are shown both in the full 3800–700 cm^{-1} range (top) as well as in the limited 2200–1980 cm^{-1} region (bottom).

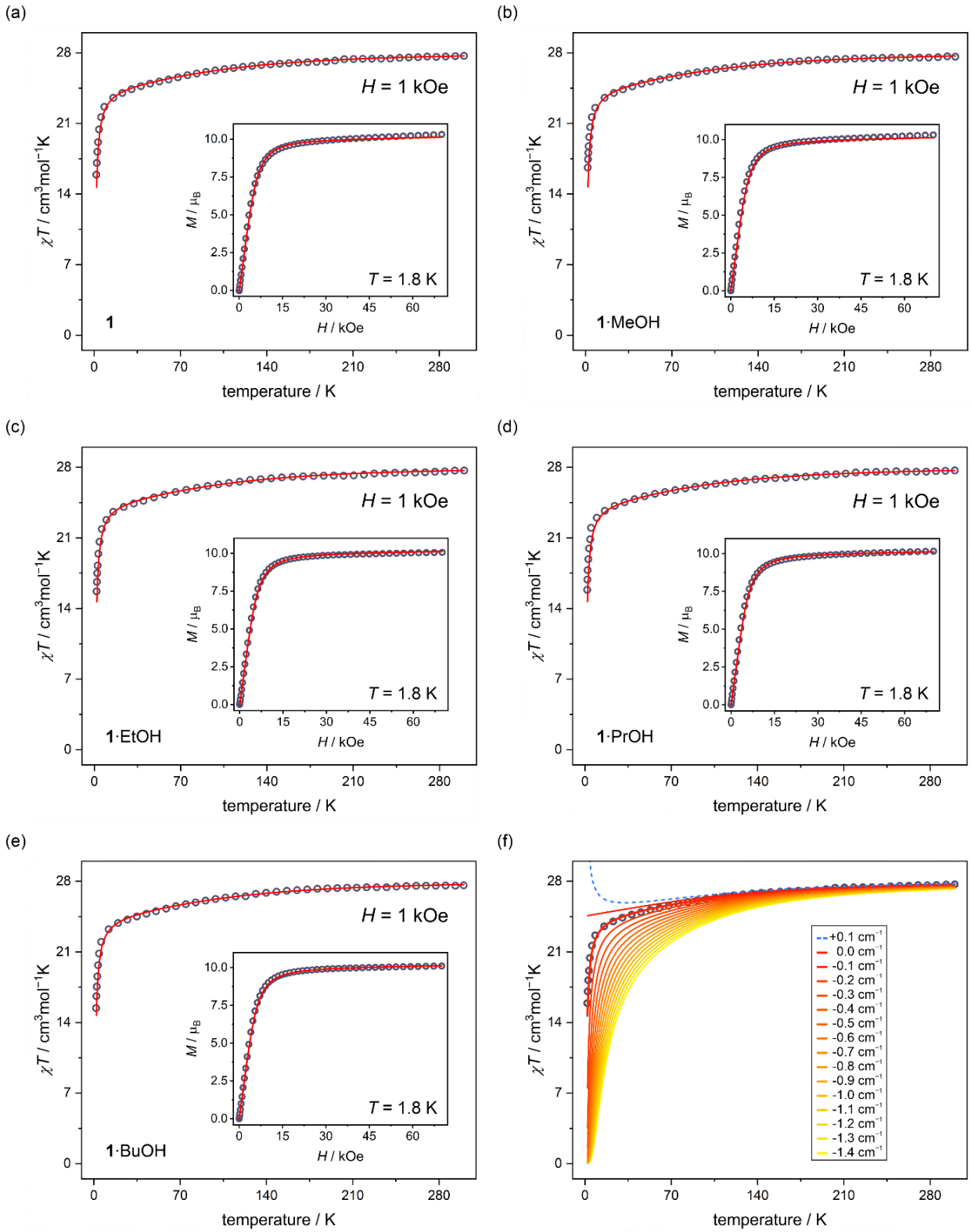

Fig. S18 Direct-current (*dc*) magnetic characteristics, including the temperature dependences of the $\chi_M T$ product under the external magnetic field of H_{dc} = 1000 Oe, and the field dependences of molar magnetization (M) collected at T = 1.8 K (the insets), for **1** (*a*), **1·MeOH** (*b*), **1·EtOH** (*c*), **1·PrOH** (*d*), and **1·BuOH** (*e*), together with the comparison of the experimental $\chi_M T$ and $M(H)$ curves (blue circle points) and the theoretical ones (red solid lines), obtained using the *ab initio* calculations, and, for **1**, the fitting curves of the $\chi_M T$ versus T plots for $\{Dy^{III}_2Fe^{II}_2\}^{6+}$ molecular cations, taking into account the Dy–Dy magnetic interactions with various indicated J values from the range between +0.1 cm^{-1} and −1.4 cm^{-1} (*f*). The details of the related calculations are provided below.

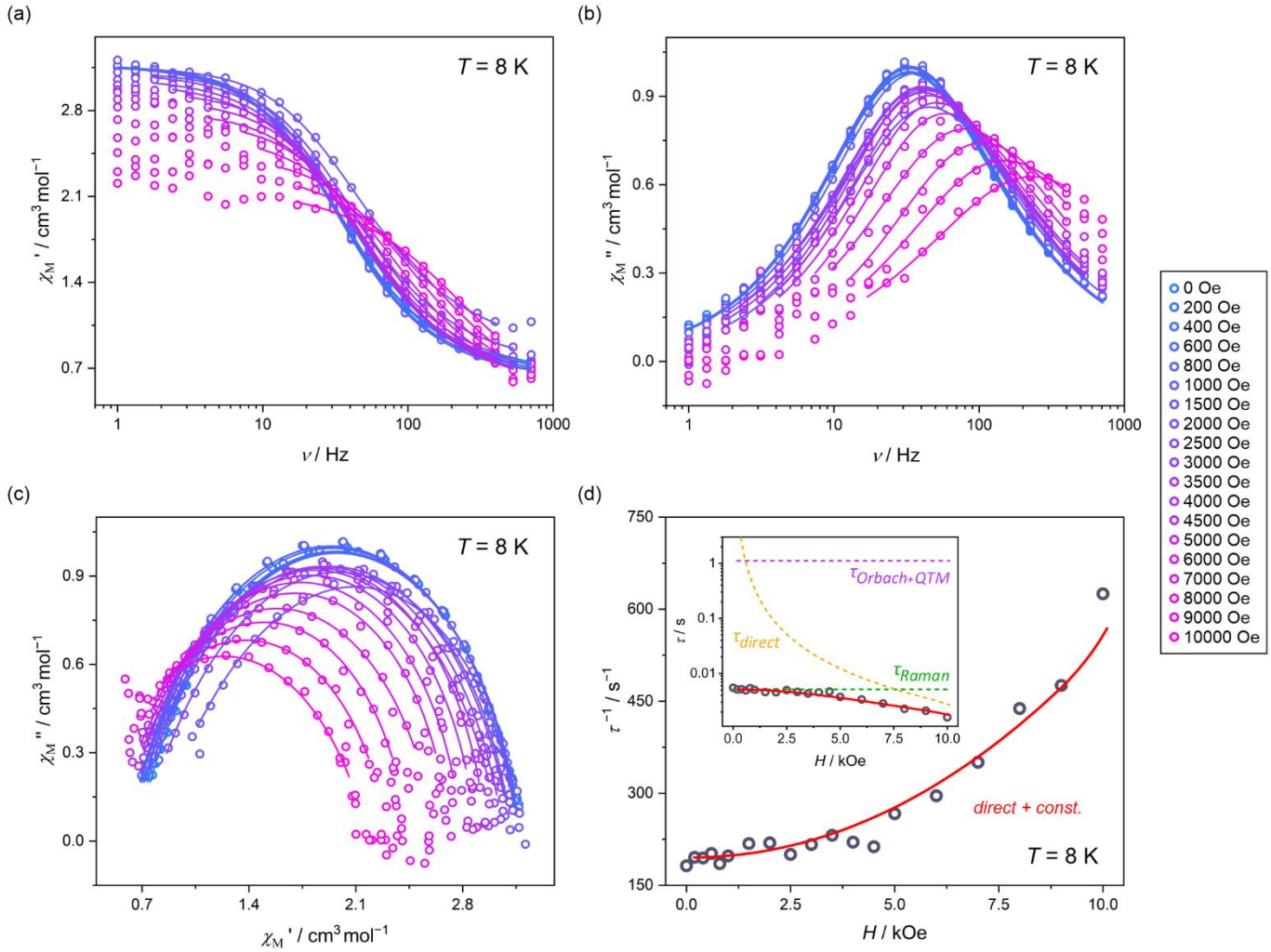

Fig. S19 Magnetic-field-variable alternate-current (*ac*) magnetic characteristics of **1** at T = 8 K, shown with the related analyses: the frequency dependences of (*a*) the in-phase susceptibility, χ_M', and (*b*) the out-of-phase susceptibility, χ_M", under variable indicated *dc* fields from the range of 0–10 kOe, (*c*) the related Argand plots, and (*d*) the field dependence of resulting relaxation times, τ. Colored solid curves in (*a*–*c*) represent the best fits using the generalized Debye model for a single relaxation process. The red solid line in (*d*) shows the best fit taking into account indicated relaxation processes (the simultaneous fits for the temperature-dependent relaxation times are shown in Fig. S20–S21), while the dashed colored lines represent the respective course of individual magnetic relaxation processes. For details see the comment to Fig. S18–S34 below. Best-fit parameters for the (*d*) part are gathered in Table S15.

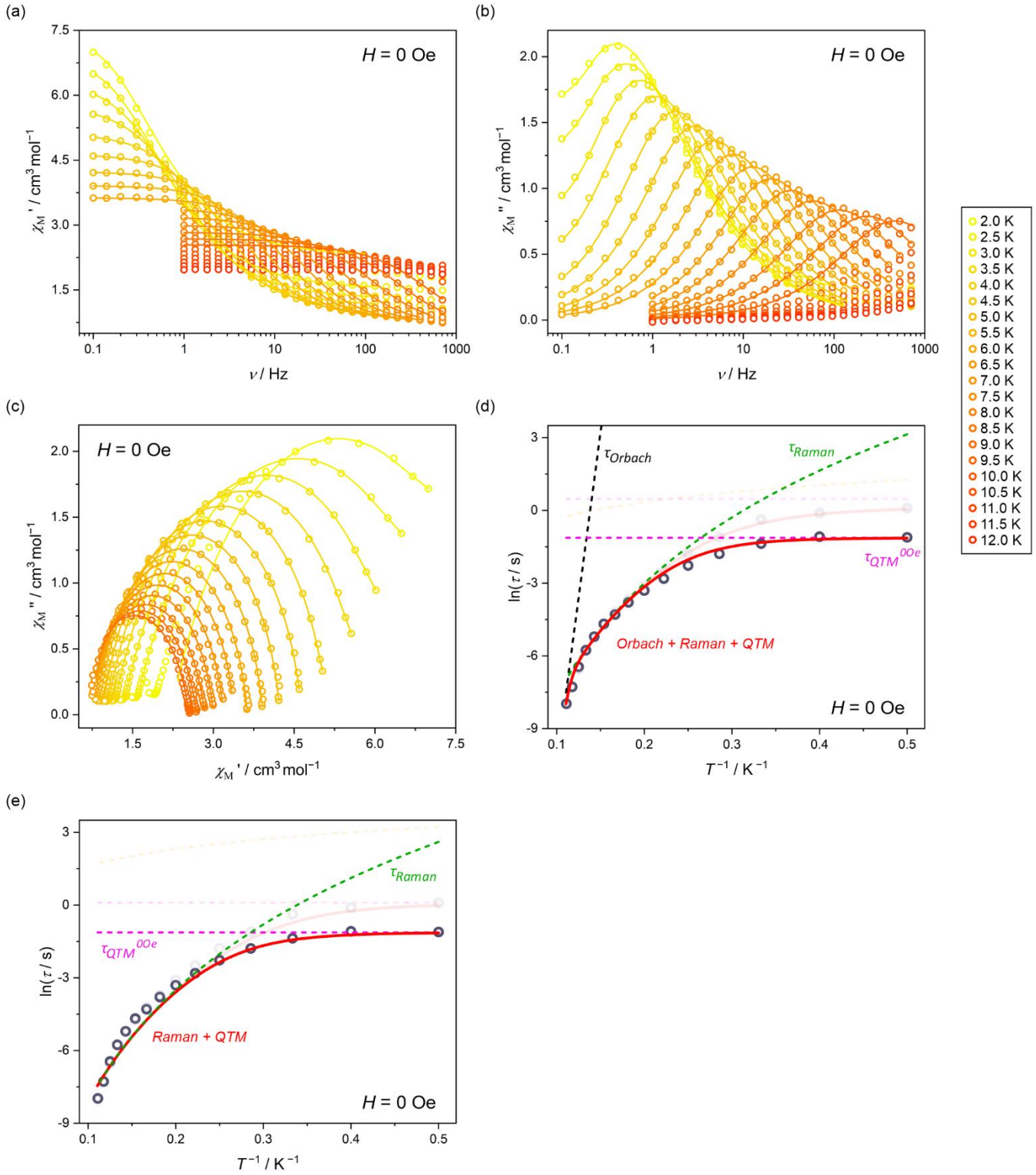

Fig. S20 Temperature-variable alternate-current (*ac*) magnetic characteristics of **1** under the zero *dc* field, shown with the related analyses: the frequency dependences of (*a*) the in-phase susceptibility, χ_M', and (*b*) the out-of-phase susceptibility, χ_M'', under variable indicated temperatures from the range of 2−12 K, (*c*) the related Argand plots, and (*d*–*e*) the temperature dependence of resulting relaxation times, τ. Colored solid curves in (*a*–*c*) represent the best fits using the generalized Debye model for a single relaxation process. The red solid line in (*d*) and (*e*) shows the best fit taking into account indicated relaxation processes (the simultaneous fit with the field-dependent relaxation times is shown in Fig. S19 and the temperature-dependent relaxation times under applied *dc* field are shown in Fig. S21), while dashed colored lines represent the respective course of individual relaxation processes. In the background of the (*d*) and (*e*) parts, the results of the temperature dependence of relaxation time for the optimal *dc* field of 600 Oe were visualized (see Fig. S21 for comparison). For details see the comment to Fig. S18–S34 below. Best-fit parameters for the (*d*) and (*e*) parts are gathered in Table S15.

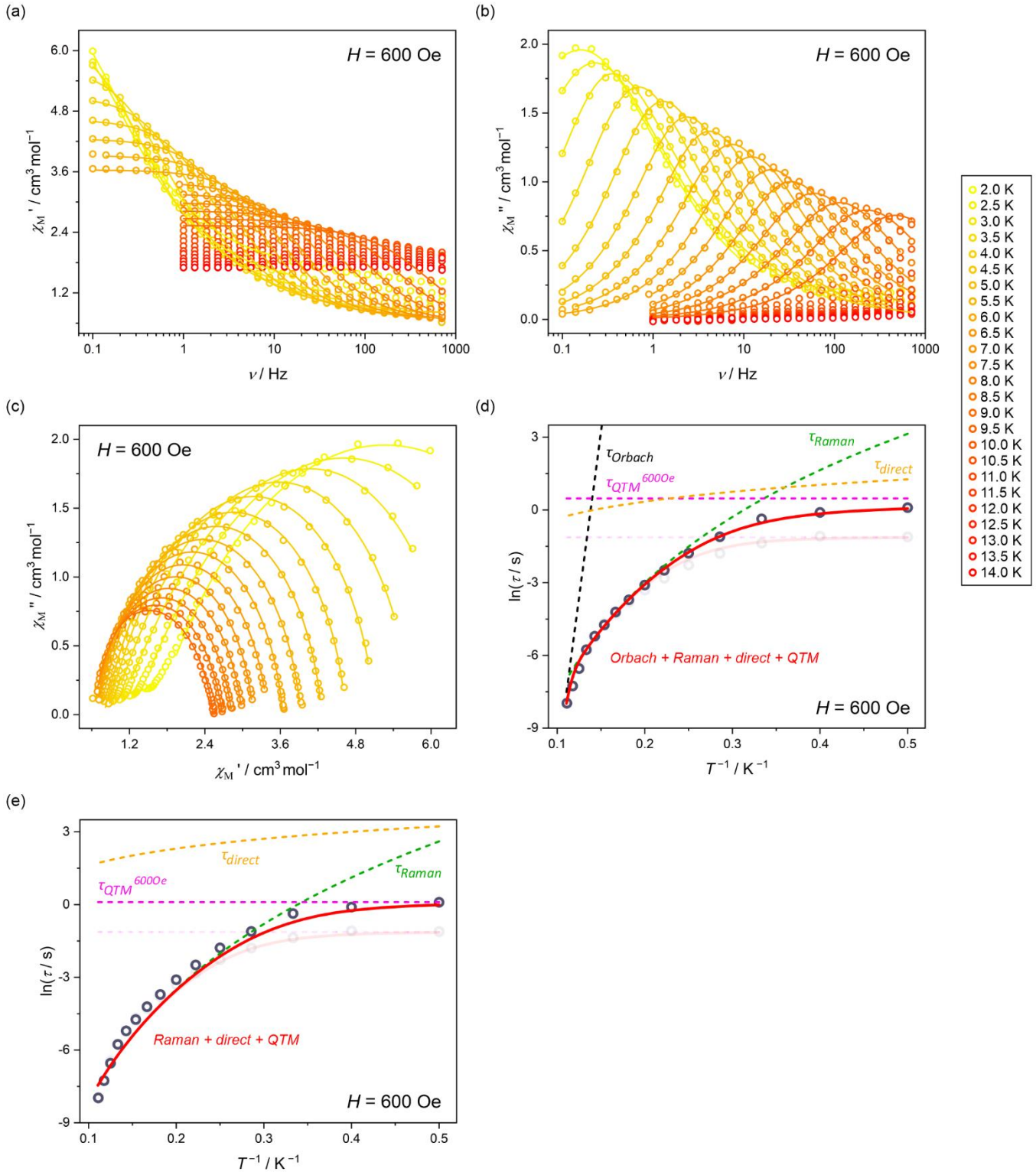

Fig. S21 Temperature-variable alternate-current (*ac*) magnetic characteristics of **1** under the optimal *dc* field, H_{dc} of 600 Oe, shown with the related analyses: the frequency dependences of (*a*) the in-phase susceptibility, χ_M', and (*b*) the out-of-phase susceptibility, χ_M", under variable indicated temperatures from the range of 2−14 K, (*c*) the related Argand plots, and (*d*–*e*) the temperature dependence of resulting relaxation times, τ. Colored solid curves in (*a*–*c*) represent the best fits using the generalized Debye model for a single relaxation process. The red solid line in (*d*) and (*e*) shows the best fit taking into account indicated relaxation processes (the simultaneous fit with the field-dependent relaxation times is shown in Fig. S19 and the temperature-dependent relaxation times under the zero *dc* field are shown in Fig. S20), while dashed colored lines represent the respective course of individual relaxation processes. In the background of the (*d*) and (*e*) parts, the results of the temperature dependence of relaxation time for the zero *dc* field were visualized (see Fig. S20 for comparison). For details see the comment to Fig. S18–S34 below. Best-fit parameters for the (*d*) and (*e*) parts are gathered in Table S15.

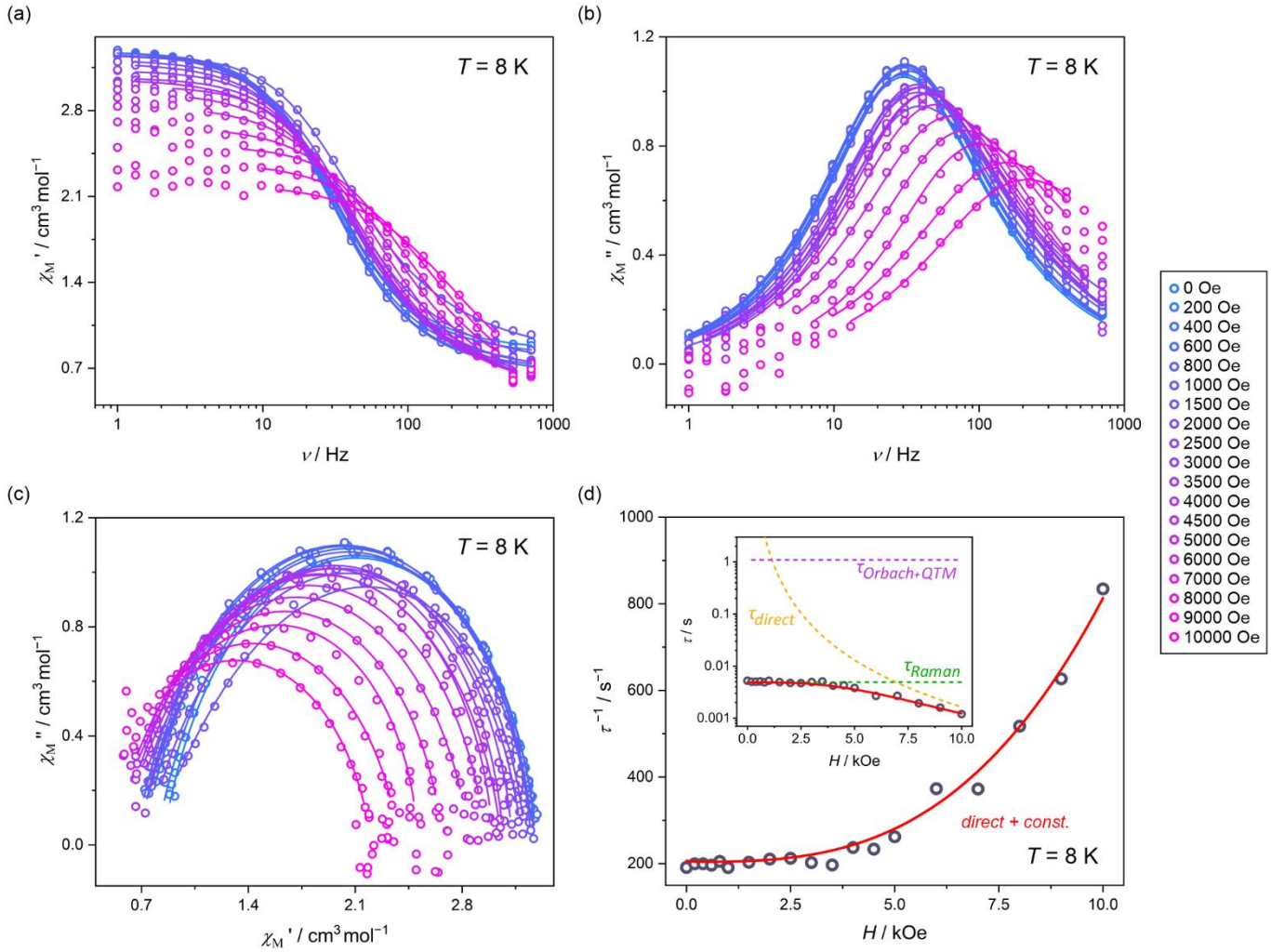

Fig. S22 Magnetic-field-variable alternate-current (*ac*) magnetic characteristics of **1·MeOH** at T = 8 K, shown with the related analyses: the frequency dependences of (*a*) the in-phase susceptibility, χ_M', and (*b*) the out-of-phase susceptibility, χ_M", under variable indicated *dc* fields from the range of 0–10 kOe, (*c*) the related Argand plots, and (*d*) the field dependence of resulting relaxation times, τ. Colored solid curves in (*a*–*c*) represent the best fits using the generalized Debye model for a single relaxation process. The red solid line in (*d*) shows the best fit taking into account indicated relaxation processes (the simultaneous fits with the temperature-dependent relaxation times are shown in Fig. S23–S24), while the dashed colored lines represent the respective course of individual relaxation processes. For details see the comment to Fig. S18–S34 below. Best-fit parameters for the (*d*) part are gathered in Table S15.

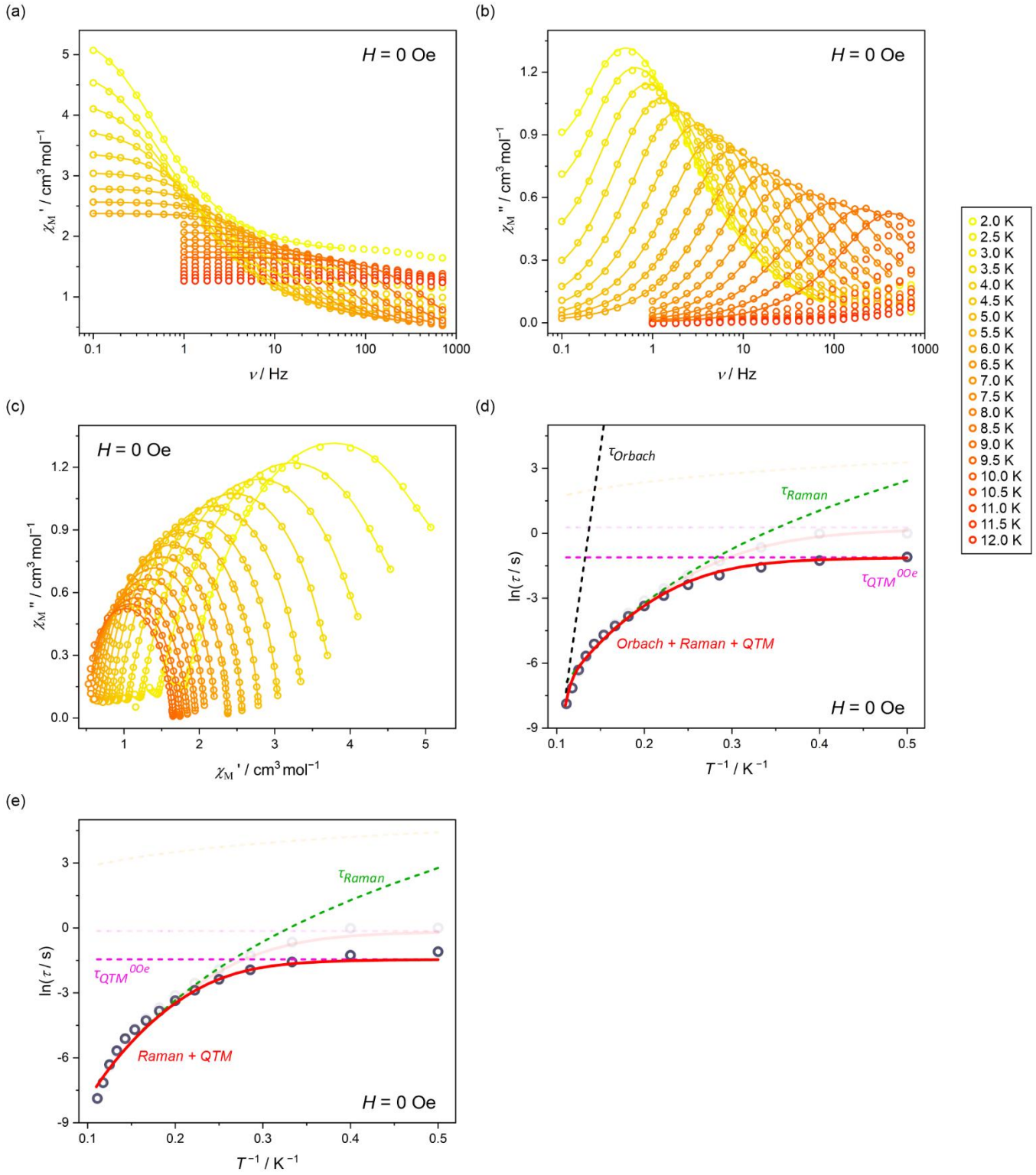

Fig. S23 Temperature-variable alternate-current (*ac*) magnetic characteristics of **1·MeOH** under the zero *dc* field, shown with the related analyses: the frequency dependences of (*a*) the in-phase susceptibility, χ_M', and (*b*) the out-of-phase susceptibility, χ_M'', under variable indicated temperatures from the range of 2–12 K, (*c*) the related Argand plots, and (*d*–*e*) the temperature dependence of resulting relaxation times, τ. Colored solid curves in (*a*–*c*) represent the best fits using the generalized Debye model for a single relaxation process. The red solid line in (*d*) and (*e*) shows the best fit taking into account indicated relaxation processes (the simultaneous fit with the field-dependent relaxation times is shown in Fig. S22 and the temperature-dependent relaxation times under the applied *dc* field are shown in Fig. S24), while dashed colored lines represent the respective course of individual relaxation processes. In the background of the (*d*) and (*e*) parts, the results of the temperature dependence of relaxation time for the optimal *dc* field of 600 Oe were visualized (see Fig. S24 for comparison). For details see the comment to Fig. S18–S34 below. Best-fit parameters for the (*d*) and (*e*) parts are gathered in Table S15.

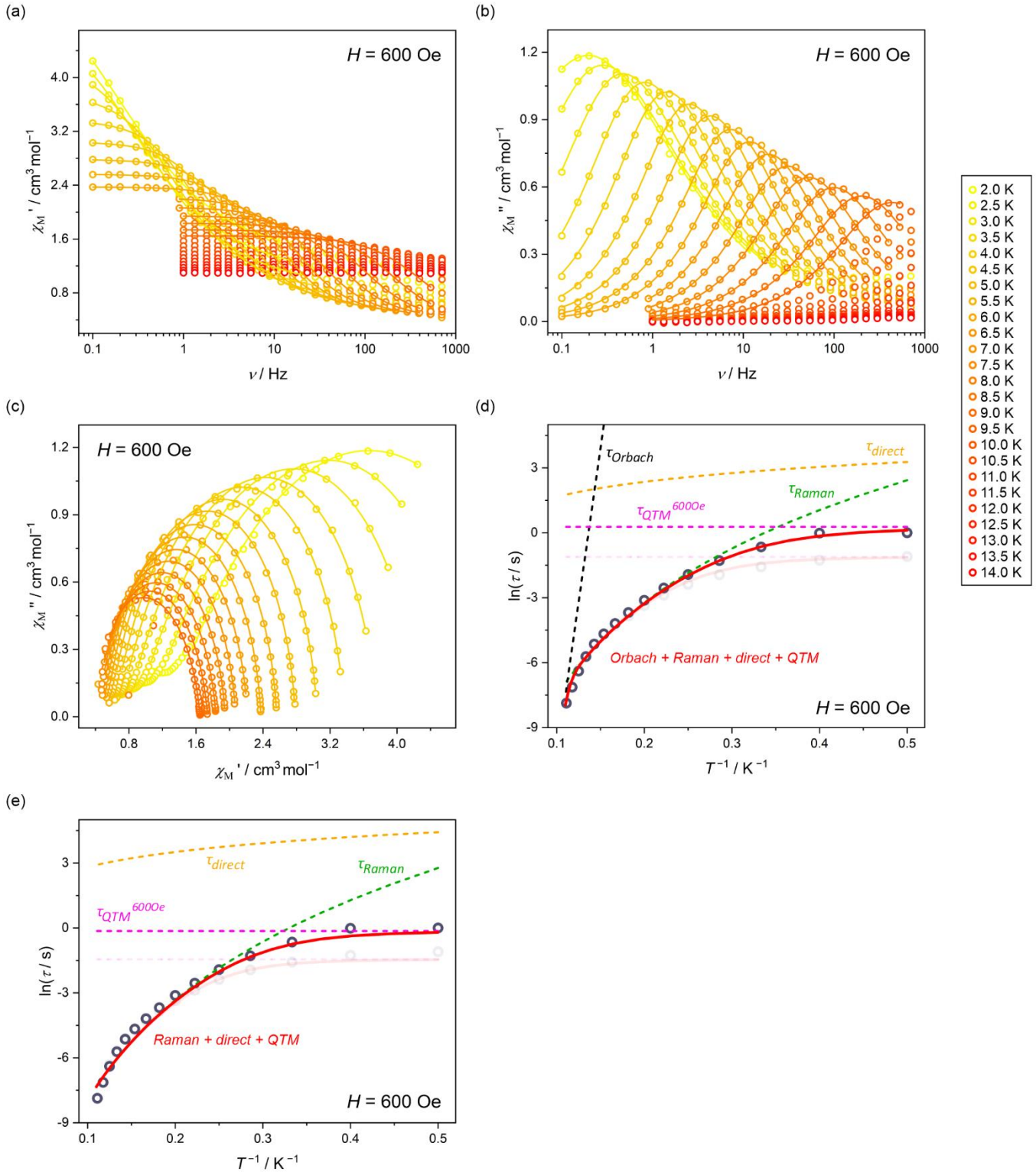

Fig. S24 Temperature-variable alternate-current (*ac*) magnetic characteristics of **1·MeOH** under the optimal *dc* field, H_{dc} of 600 Oe, shown with the related analyses: the frequency dependences of (*a*) the in-phase susceptibility, χ_M', and (*b*) the out-of-phase susceptibility, χ_M'', under variable indicated temperatures from the range of 2–14 K, (*c*) the related Argand plots, and (*d–e*) the temperature-dependence of resulting relaxation times, τ. Colored solid curves in (*a–c*) represent the best fits using the generalized Debye model for a single relaxation process. The red solid line in (*d*) and (*e*) shows the best fit taking into account indicated relaxation processes (the simultaneous fit with the field-dependent relaxation times is shown in Fig. S22 and the temperature-dependent relaxation times under the zero *dc* field are shown in Fig. S23), while dashed colored lines represent the respective course of individual relaxation processes. In the background of the (*d*) and (*e*) parts, the results of the temperature dependence of relaxation time for the zero *dc* field were visualized (see Fig. S23 for comparison). For details see the comment to Fig. S18–S34 below. Best-fit parameters for the (*d*) and (*e*) parts are gathered in Table S15.

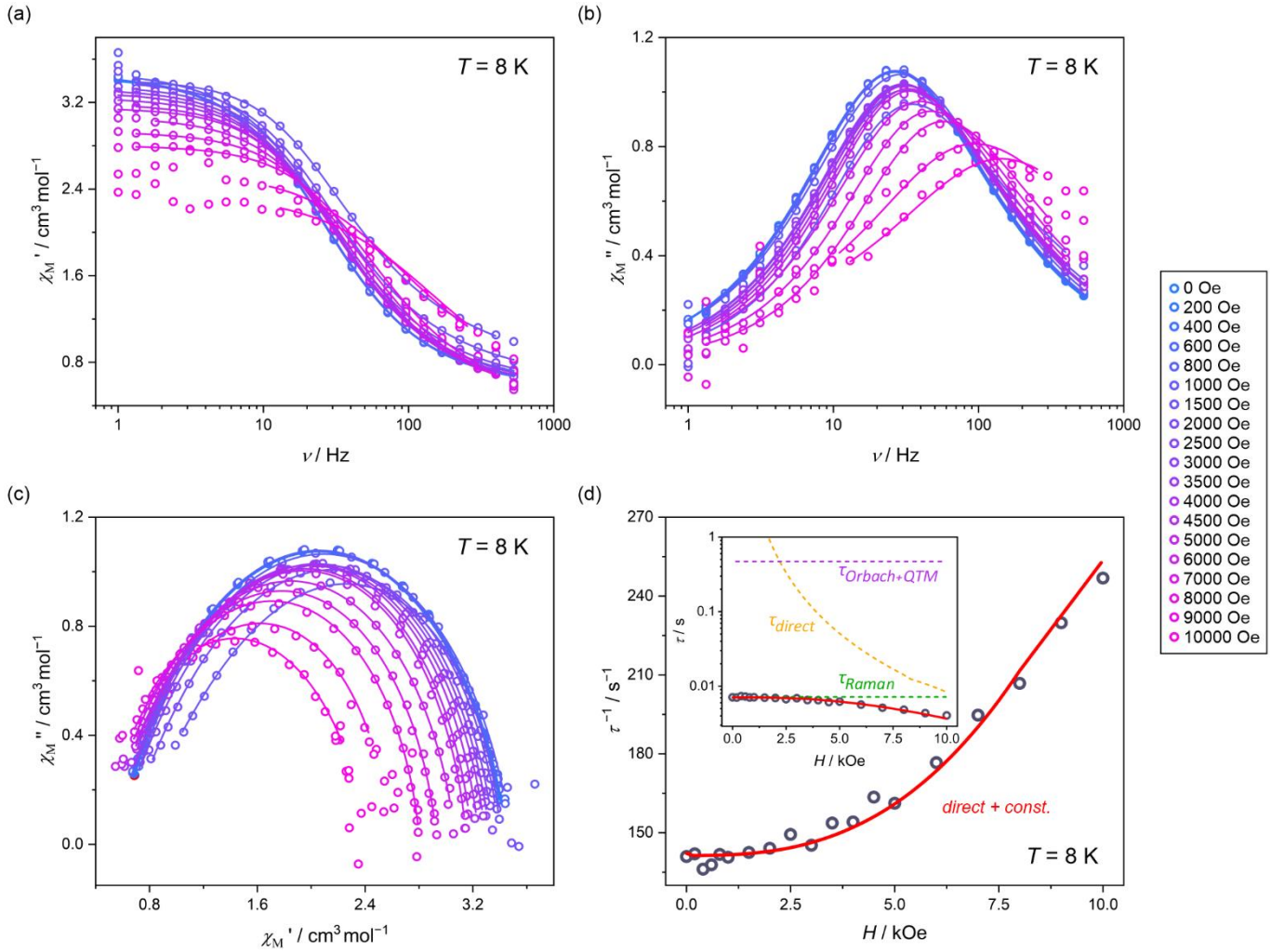

Fig. S25 Magnetic-field-variable alternate-current (*ac*) magnetic characteristics of **1·EtOH** at T = 8 K, shown with the related analyses: the frequency dependences of (*a*) the in-phase susceptibility, χ_M', and (*b*) the out-of-phase susceptibility, χ_M", under variable indicated *dc* fields from the range of 0–10 kOe, (*c*) the related Argand plots, and (*d*) the field-dependence of resulting relaxation times, τ. Colored solid curves in (*a*–*c*) represent the best fits using the generalized Debye model for a single relaxation process. The red solid line in (*d*) shows the best fit taking into account indicated relaxation processes (the simultaneous fits with the temperature-dependent relaxation times are shown in Fig. S26–S27), while the dashed colored lines represent the respective course of individual relaxation processes. For details see the comment to Fig. S18–S34 below. Best-fit parameters for the (*d*) part are gathered in Table S15.

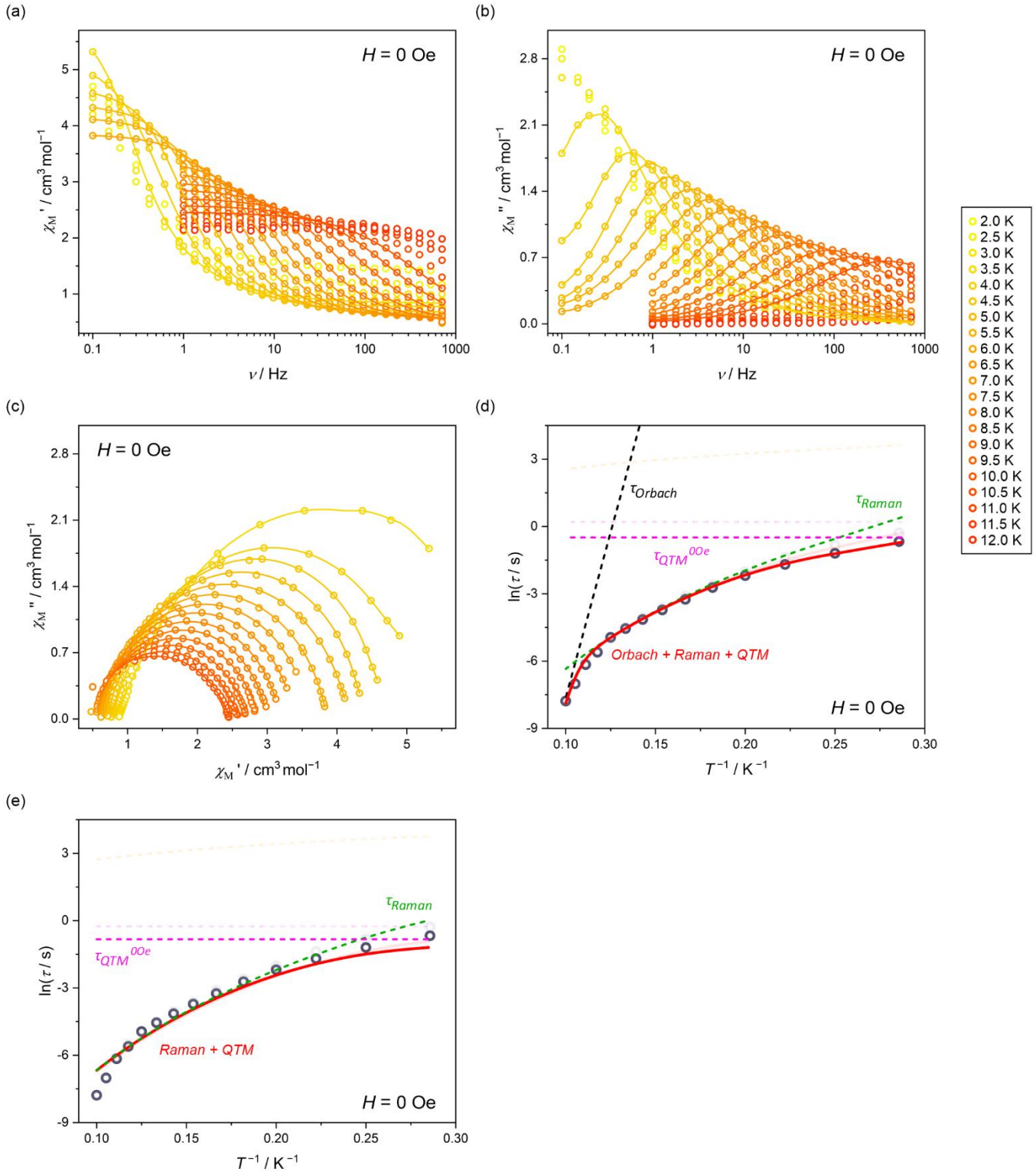

Fig. S26 Temperature-variable alternate-current (*ac*) magnetic characteristics of **1·EtOH** under the zero *dc* field, shown with the related analyses: the frequency dependences of (*a*) the in-phase susceptibility, χ_M', and (*b*) the out-of-phase susceptibility, χ_M'', under variable indicated temperatures from the range of 2–12 K, (*c*) the related Argand plots, and (*d–e*) the temperature-dependence of resulting relaxation times, τ. Colored solid curves in (*a–c*) represent the best fits using the generalized Debye model for a single relaxation process. The red solid line in (*d*) and (*e*) shows the best fit taking into account indicated relaxation processes (the simultaneous fit with the field-dependent relaxation times is shown in Fig. S25 and the temperature-dependent relaxation times under the applied *dc* field are shown in Fig. S27), while dashed colored lines represent the respective course of individual relaxation processes. In the background of the (*d*) and (*e*) parts, the results of the temperature dependence of relaxation time for the optimal *dc* field of 600 Oe were visualized (see Fig. S27 for comparison). For details see the comment to Fig. S18–S34 below. Best-fit parameters for the (*d*) and (*e*) parts are gathered in Table S15.

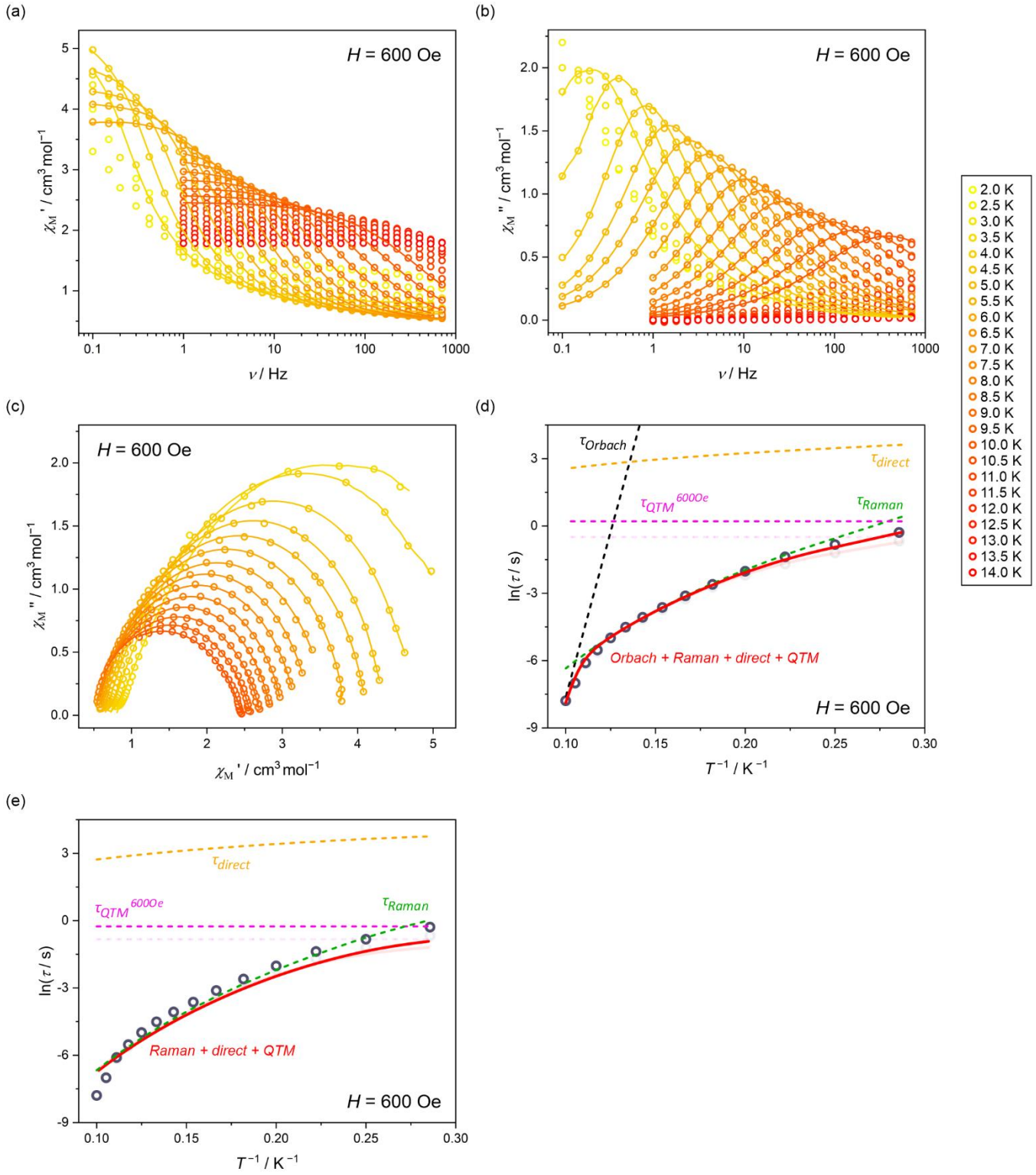

Fig. S27 Temperature-variable alternate-current (*ac*) magnetic characteristics of **1·EtOH** under the optimal *dc* field, H_{dc} of 600 Oe, shown with the related analyses: the frequency dependences of (*a*) the in-phase susceptibility, χ_M', and (*b*) the out-of-phase susceptibility, χ_M'', under variable indicated temperatures from the range of 2−14 K, (*c*) the related Argand plots, and (*d*–*e*) the temperature dependence of resulting relaxation times, τ. Colored solid curves in (*a*–*c*) represent the best fits using the generalized Debye model for a single relaxation process. The red solid line in (*d*) and (*e*) shows the best fit taking into account indicated relaxation processes (the simultaneous fit with the field-dependent relaxation times is shown in Fig. S25 and the temperature-dependent relaxation times under the zero *dc* field are shown in Fig. S26), while dashed colored lines represent the respective course of individual relaxation processes. In the background of the (*d*) and (*e*) parts, the results of the temperature dependence of relaxation time for the zero *dc* field were visualized (see Fig. S26 for comparison). For details see the comment to Fig. S18–S34 below. Best-fit parameters for the (*d*) and (*e*) parts are gathered in Table S15.

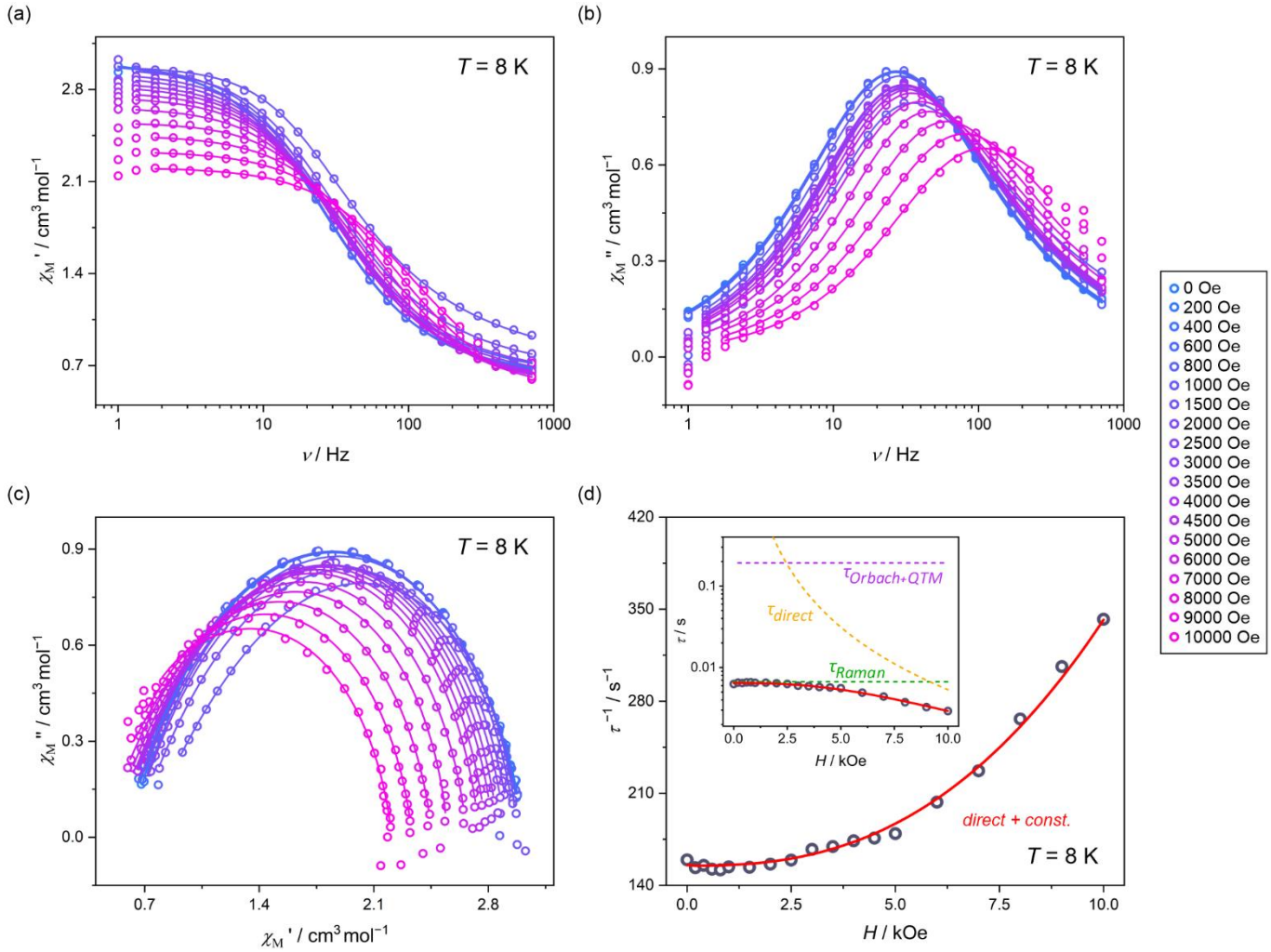

Fig. S28 Magnetic-field-variable alternate-current (*ac*) magnetic characteristics of **1·PrOH** at T = 8 K, shown with the related analyses: the frequency dependences of (*a*) the in-phase susceptibility, χ_M', and (*b*) the out-of-phase susceptibility, χ_M", under variable indicated *dc* fields from the range of 0–10 kOe, (*c*) the related Argand plots, and (*d*) the field-dependence of resulting relaxation times, τ. Colored solid curves in (*a*–*c*) represent the best fits using the generalized Debye model for a single relaxation process. The red solid line in (*d*) shows the best fit taking into account indicated relaxation processes (the simultaneous fits with the temperature-dependent relaxation times are shown in Fig. S29–S30), while the dashed colored lines represent the respective course of individual relaxation processes. For details see the comment to Fig. S18–S34 below. Best-fit parameters for the (*d*) part are gathered in Table S15.

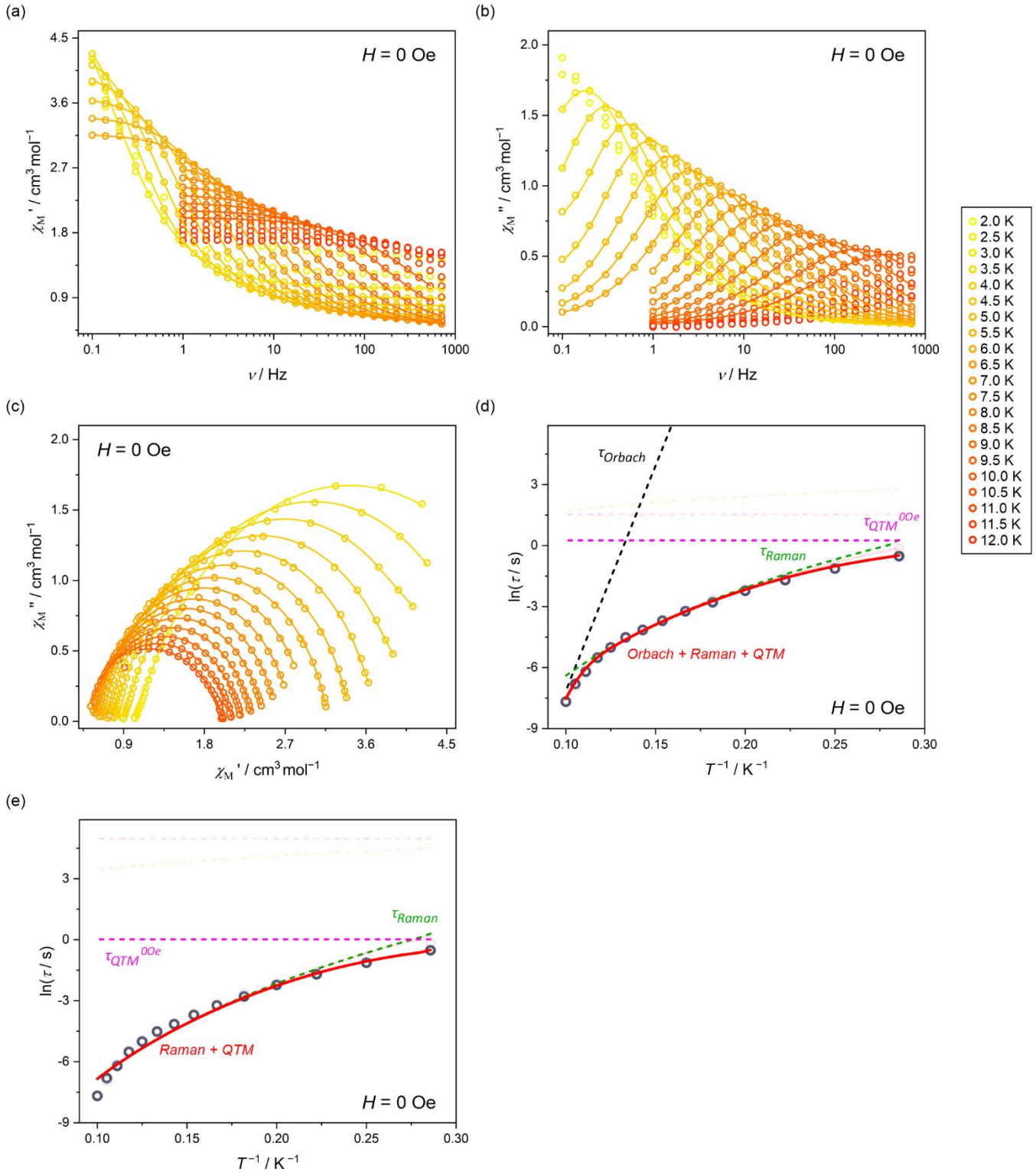

Fig. S29 Temperature-variable alternate-current (*ac*) magnetic characteristics of **1·PrOH** under the zero *dc* field, shown with the related analyses: the frequency dependences of (*a*) the in-phase susceptibility, χ_M', and (*b*) the out-of-phase susceptibility, χ_M'', under variable indicated temperatures from the range of 2–12 K, (*c*) the related Argand plots, and (*d*–*e*) the temperature-dependence of resulting relaxation times, τ. Colored solid curves in (*a*–*c*) represent the best fits using the generalized Debye model for a single relaxation process. The red solid line in (*d*) and (*e*) shows the best fit taking into account indicated relaxation processes (the simultaneous fit with the field-dependent relaxation times is shown in Fig. S28 and the temperature-dependent relaxation times under the applied *dc* field are shown in Fig. S30), while dashed colored lines represent the respective course of individual relaxation processes. In the background of the (*d*) and (*e*) parts, the results of the temperature dependence of relaxation time for the optimal *dc* field of 600 Oe were visualized (see Fig. S30 for comparison). For details see the comment to Fig. S18–S34 below. Best-fit parameters for the (*d*) and (*e*) parts are gathered in Table S15.

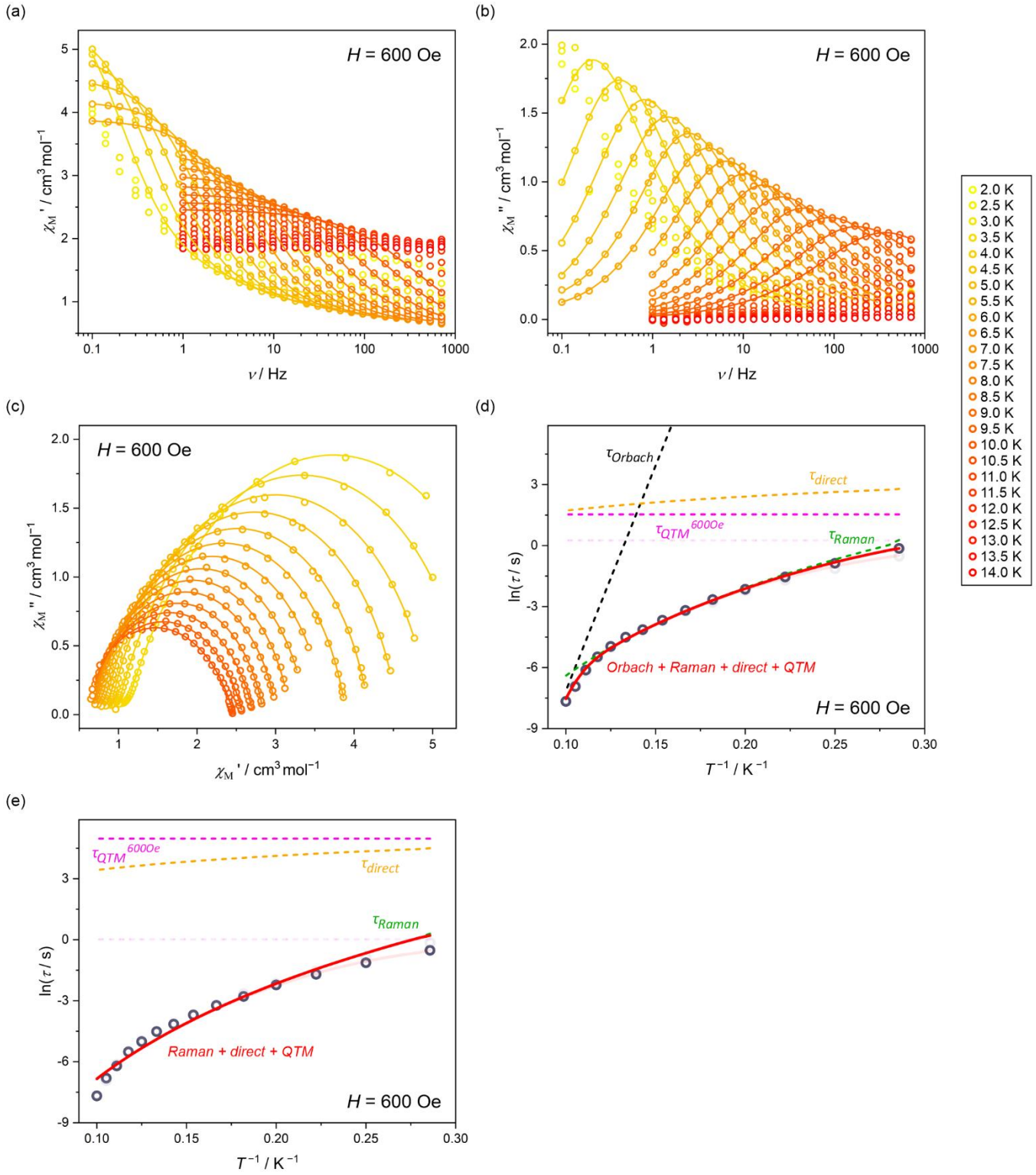

Fig. S30 Temperature-variable alternate-current (*ac*) magnetic characteristics of **1·PrOH** under the optimal *dc* field, H_{dc} of 600 Oe, shown with the related analyses: the frequency dependences of (*a*) the in-phase susceptibility, χ_M', and (*b*) the out-of-phase susceptibility, χ_M'', under variable indicated temperatures from the range of 2−14 K, (*c*) the related Argand plots, and (*d*–*e*) the temperature-dependence of resulting relaxation times, τ. Colored solid curves in (*a*–*c*) represent the best fits using the generalized Debye model for a single relaxation process. The red solid line in (*d*) and (*e*) shows the best fit taking into account indicated relaxation processes (the simultaneous fit with the field-dependent relaxation times is shown in Fig. S28 and the temperature-dependent relaxation times under the zero *dc* field are shown in Fig. S29), while dashed colored lines represent the respective course of individual relaxation processes. In the background of the (*d*) and (*e*) parts, the results of the temperature dependence of relaxation time for the zero *dc* field were visualized (see Fig. S29 for comparison). For details see the comment to Fig. S18–S34 below. Best-fit parameters for the (*d*) and (*e*) parts are gathered in Table S15.

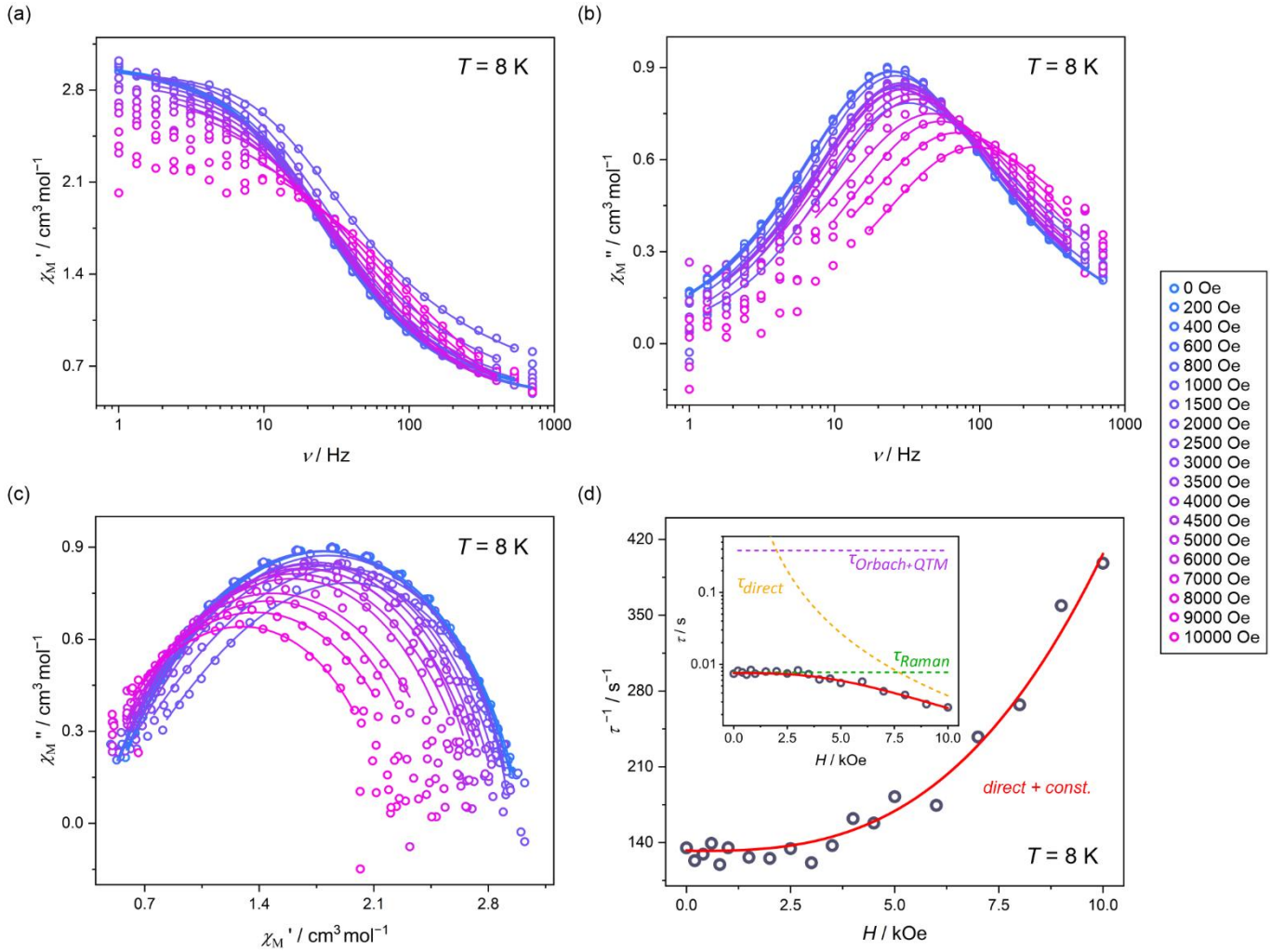

Fig. S31 Magnetic-field-variable alternate-current (*ac*) magnetic characteristics of **1·BuOH** at T = 8 K, shown with the related analyses: the frequency dependences of (*a*) the in-phase susceptibility, χ_M', and (*b*) the out-of-phase susceptibility, χ_M", under variable indicated *dc* fields from the range of 0–10 kOe, (*c*) the related Argand plots, and (*d*) the field dependence of resulting relaxation times, τ. Colored solid curves in (*a*–*c*) represent the best fits using the generalized Debye model for a single relaxation process. The red solid line in (*d*) shows the best fit taking into account indicated relaxation processes (the simultaneous fits with the temperature-dependent relaxation times are shown in Fig. S32–S33), while the dashed colored lines represent the respective course of individual relaxation processes. For details see the comment to Fig. S18–S34 below. Best-fit parameters for the (*d*) part are gathered in Table S15.

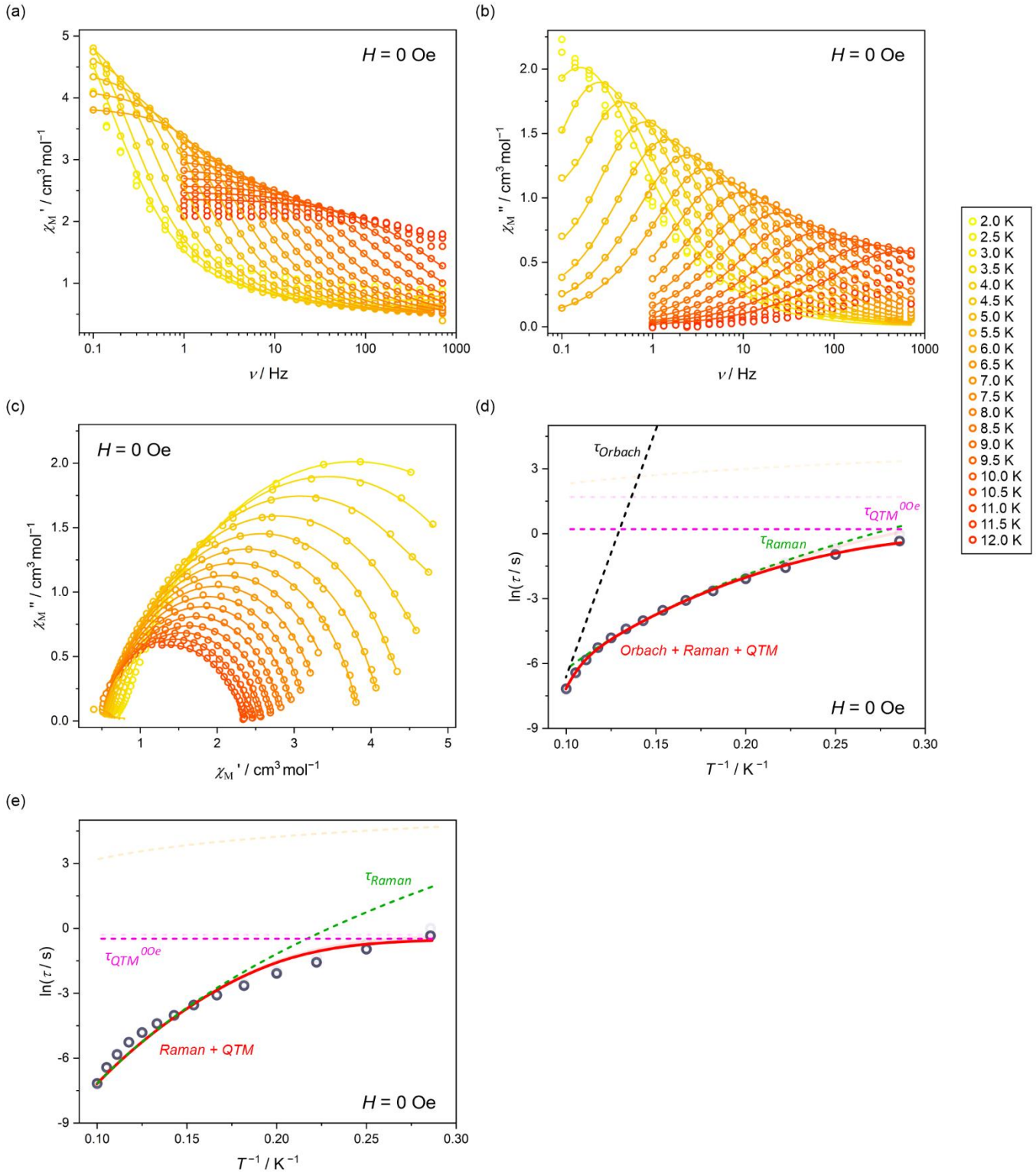

Fig. S32 Temperature-variable alternate-current (*ac*) magnetic characteristics of **1·BuOH** under the zero *dc* field, shown with the related analyses: the frequency dependences of (*a*) the in-phase susceptibility, χ_M', and (*b*) the out-of-phase susceptibility, χ_M", under variable indicated temperatures from the range of 2–12 K, (*c*) the related Argand plots, and (*d*–*e*) the temperature dependence of resulting relaxation times, τ. Colored solid curves in (*a*–*c*) represent the best fits using the generalized Debye model for a single relaxation process. The red solid line in (*d*) and (*e*) shows the best fit taking into account indicated relaxation processes (the simultaneous fit with the field-dependent relaxation times is shown in Fig. S31 and the temperature-dependent relaxation times under the applied *dc* field are shown in Fig. S33), while dashed colored lines represent the respective course of individual relaxation processes. In the background of the (*d*) and (*e*) parts, the results of the temperature dependence of relaxation time for the optimal *dc* field of 600 Oe were visualized (see Fig. S33 for comparison). For details see the comment to Fig. S18–S34 below. Best-fit parameters for the (*d*) and (*e*) parts are gathered in Table S15.

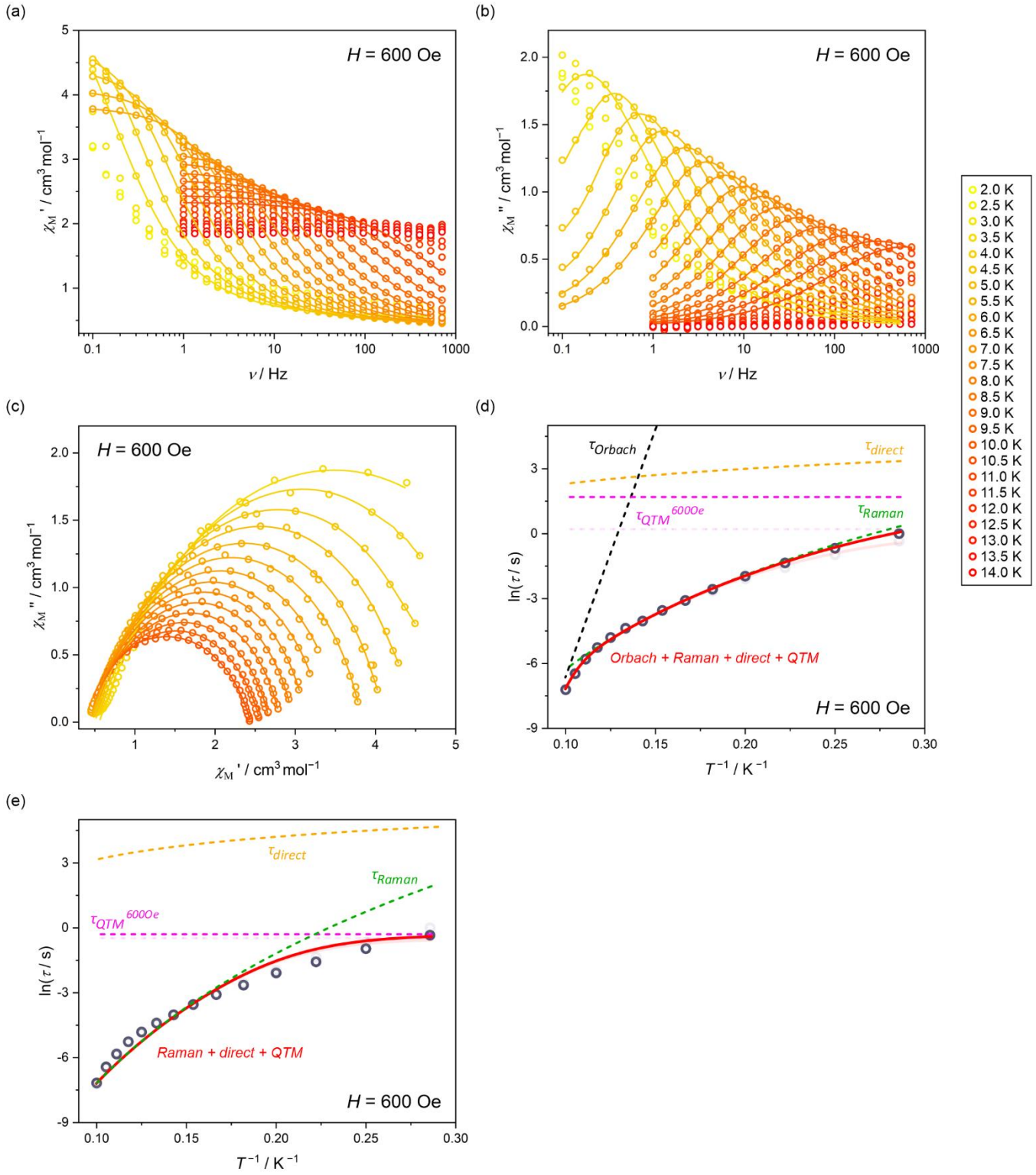

Fig. S33 Temperature-variable alternate-current (*ac*) magnetic characteristics of **1·BuOH** under the optimal *dc* field, H_{dc} of 600 Oe, shown with the related analyses: the frequency dependences of (*a*) the in-phase susceptibility, χ_M', and (*b*) the out-of-phase susceptibility, χ_M'', under variable indicated temperatures from the range of 2–14 K, (*c*) the related Argand plots, and (*d*–*e*) the temperature dependence of resulting relaxation times, τ. Colored solid curves in (*a*–*c*) represent the best fits using the generalized Debye model for a single relaxation process. The red solid line in (*d*) and (*e*) shows the best fit taking into account indicated relaxation processes (the simultaneous fit with the field-dependent relaxation times is shown in Fig. S31 and the temperature-dependent relaxation times under the zero *dc* field are shown in Fig. S32), while dashed colored lines represent the respective course of individual relaxation processes. In the background of the (*d*) and (*e*) parts, the results of the temperature dependence of relaxation time for the zero *dc* field were visualized (see Fig. S32 for comparison). For details see the comment to Fig. S18–S34 below. Best-fit parameters for the (*d*) and (*e*) parts are gathered in Table S15.

Table S15 Summary of the critical slow magnetic relaxation parameters for reported compounds of **1**, **1·MeOH**, **1·EtOH**, **1·PrOH**, and **1·BuOH**, determined within the three-dimensional simultaneous fitting of the field- and temperature-dependences of relaxation times (see Fig. S19–S21, Fig. S22–S24, Fig. S25–S27, Fig. S28–S30, and Fig. S31–S33 for **1**, **1·MeOH**, **1·EtOH**, **1·PrOH**, and **1·BuOH**, respectively). The details of applied fitting procedures are discussed in the comment below. The resulting percentage contributions of direct, QTM, Raman, and Orbach processes to the overall magnetic relaxation time are presented in Table S16 and Fig. 34.

compound	**1**	**1·MeOH**	**1·EtOH**	**1·PrOH**	**1·BuOH**
A_{direct} / $s^{-1}K^{-1}Oe^{-m}$	$2.38(1)\cdot10^{-7}$	$1.00(3)\cdot10^{-10}$	$2.26(5)\cdot10^{-10}$	$1.49(4)\cdot10^{-9}$	$9.12(8)\cdot10^{-11}$
m	2.08(4)	2.86(4)	2.71(7)	2.55(3)	2.89(8)
B_{Raman} / $s^{-1}K^{-n}$	$4.11(6)\cdot10^{-4}$	$7.22(7)\cdot10^{-4}$	$2.66(3)\cdot10^{-4}$	$3.49(8)\cdot10^{-4}$	$2.72(6)\cdot10^{-4}$
n	6.72(2)	6.36(1)	6.33(4)	6.24(3)	6.22(5)
τ_{QTM} for H_{dc} = 0 Oe / s	0.32(2)	0.29(5)	0.61 (4)	1.29(5)	1.23(7)
τ_{QTM} for H_{dc} = 600 Oe / s	1.61(6)	1.06(7)	1.23(9)	4.63(6)	5.44(9)
τ_0 / s	$4.37(5)\cdot10^{-17}$	$1.78(2)\cdot10^{-17}$	$7.96(8)\cdot10^{-17}$	$1.88(8)\cdot10^{-13}$	$1.65(4)\cdot10^{-13}$
ΔE in cm^{-1} [$\Delta E/k_B$ in K]	190.80 (fixed) [272.6]	199.04 (fixed) [284.4]	206.05 (fixed) [294.4]	155.07 (fixed) [221.6]	159.83 (fixed) [228.4]

Table S16 Percentage contributions of direct, OTM, Raman and Orbach processes to the overall relaxation time of **1**, **1·MeOH**, **1·EtOH**, **1·PrOH**, and **1·BuOH** for indicated external *dc* fields, H_{dc} (see Fig. S20–S21, Fig. S23–S24, Fig. S26–S27, Fig. S29–S30, and Fig. S32–S33 for **1**, **1·MeOH**, **1·EtOH**, **1·PrOH**, and **1·BuOH**, respectively). The percentage contributions are given for the inversion of the relaxation time (τ^{-1}) and calculated using the best-fit parameters gathered in Table S15.

T / K	% direct	% QTM	% Raman	% Orbach	% direct	% QTM	% Raman	% Orbach
	compound **1**							
	0 Oe				600 Oe			
2.0	–	98.62	1.38	0.00	29.96	65.49	4.55	0.00
2.5	–	94.12	5.88	0.00	30.37	53.11	16.52	0.00
3.0	–	82.47	17.53	0.00	24.00	36.43	38.57	0.00
3.5	–	62.56	37.44	0.00	16.74	20.91	62.35	0.00
4.0	–	40.53	59.47	0.00	9.92	10.84	79.24	0.00
4.5	–	23.61	76.39	0.00	5.67	5.51	88.82	0.00
5.0	–	13.22	86.78	0.00	3.28	2.87	93.85	0.00
5.5	–	7.43	92.57	0.00	1.96	1.56	96.48	0.00
6.0	–	4.29	95.71	0.00	1.21	0.88	97.91	0.00
6.5	–	2.55	97.44	0.01	0.77	0.52	98.70	0.01
7.0	–	1.56	98.30	0.14	0.51	0.32	99.04	0.13
7.5	–	0.98	97.83	1.19	0.34	0.20	98.27	1.19
8.0	–	0.60	92.35	7.05	0.22	0.12	92.59	7.07
8.5	–	0.31	72.38	27.31	0.12	0.06	72.48	27.34
9.0	–	0.12	39.53	60.35	0.05	0.02	39.55	60.38
T / K	compound **1·MeOH**							
	0 Oe				600 Oe			
2.0	–	98.31	1.69	0.00	1.73	92.43	5.84	0.00
2.5	–	93.37	6.63	0.00	1.82	77.85	20.33	0.00
3.0	–	81.54	18.46	0.00	1.51	53.73	44.76	0.00
3.5	–	62.36	37.64	0.00	1.01	30.73	68.26	0.00
4.0	–	41.47	58.53	0.00	0.60	16.05	83.35	0.00
4.5	–	25.09	74.91	0.00	0.35	8.32	91.33	0.00
5.0	–	14.63	85.37	0.00	0.21	4.44	95.35	0.00
5.5	–	8.55	91.45	0.00	0.13	2.47	97.40	0.00

6.0	–	5.10	94.90	0.00	0.08	1.44	98.48	0.00
6.5	–	3.13	96.86	0.01	0.05	0.87	99.07	0.01
7.0	–	1.97	97.95	0.08	0.04	0.54	99.35	0.07
7.5	–	1.27	98.02	0.71	0.02	0.35	98.92	0.71
8.0	–	0.81	94.38	4.81	0.02	0.22	94.92	4.84
8.5	–	0.46	77.74	21.80	0.01	0.12	78.00	21.87
9.0	–	0.18	44.35	55.47	0.00	0.05	44.41	55.54
T / K	compound **1·EtOH**							
	0 Oe				600 Oe			
3.5	–	68.78	31.22	0.00	1.72	51.44	46.84	0.00
4.0	–	48.61	51.39	0.00	1.21	31.65	67.14	0.00
4.5	–	30.98	69.02	0.00	0.78	18.13	81.08	0.00
5.0	–	18.72	81.28	0.00	0.49	10.25	89.26	0.00
5.5	–	11.19	88.81	0.00	0.31	5.89	93.80	0.00
6.0	–	6.77	93.23	0.00	0.20	3.48	96.32	0.00
6.5	–	4.19	95.81	0.00	0.13	2.13	97.74	0.00
7.0	–	2.66	97.33	0.01	0.09	1.34	98.56	0.01
7.5	–	1.73	98.15	0.12	0.06	0.87	98.95	0.12
8.0	–	1.15	97.93	0.92	0.04	0.58	98.45	0.93
8.5	–	0.75	94.00	5.25	0.03	0.38	94.32	5.27
9.0	–	0.44	78.61	20.95	0.02	0.22	78.77	20.99
9.5	–	0.19	48.49	51.32	0.01	0.10	48.53	51.36
10.0	–	0.06	21.72	78.22	0.00	0.03	21.72	78.25
T / K	compound **1·PrOH**							
	0 Oe				600 Oe			
3.5	–	47.36	52.64	0.00	5.51	18.90	75.59	0.00
4.0	–	28.12	71.88	0.00	3.16	9.50	87.34	0.00
4.5	–	15.80	84.20	0.00	1.82	4.87	93.31	0.00
5.0	–	8.86	91.14	0.00	1.08	2.60	96.32	0.00
5.5	–	5.09	94.91	0.00	0.67	1.46	97.87	0.00
6.0	–	3.02	96.98	0.00	0.43	0.86	98.71	0.00
6.5	–	1.86	98.12	0.02	0.28	0.52	99.18	0.02

7.0	–	1.18	98.68	0.14	0.19	0.33	99.33	0.15
7.5	–	0.76	98.46	0.78	0.13	0.21	98.88	0.78
8.0	–	0.50	96.30	3.20	0.09	0.14	96.55	3.22
8.5	–	0.32	89.30	10.38	0.06	0.09	89.45	10.40
9.0	–	0.18	74.14	25.68	0.04	0.05	74.21	25.70
9.5	–	0.09	52.50	47.41	0.02	0.03	52.52	47.43
10.0	–	0.04	32.19	67.77	0.01	0.01	32.20	67.78
T / K	compound **1·BuOH**							
	0 Oe				600 Oe			
3.5	–	54.31	45.69	0.00	3.88	20.42	75.70	0.00
4.0	–	34.04	65.96	0.00	2.23	10.25	87.52	0.00
4.5	–	19.83	80.17	0.00	1.28	5.24	93.48	0.00
5.0	–	11.35	88.65	0.00	0.76	2.80	96.44	0.00
5.5	–	6.59	93.41	0.00	0.47	1.57	97.96	0.00
6.0	–	3.94	96.06	0.00	0.30	0.92	98.78	0.00
6.5	–	2.43	97.56	0.01	0.20	0.56	99.23	0.01
7.0	–	1.54	98.38	0.08	0.13	0.35	99.43	0.09
7.5	–	1.00	98.55	0.45	0.09	0.23	99.23	0.45
8.0	–	0.66	97.36	1.98	0.07	0.15	97.79	1.99
8.5	–	0.43	92.65	6.92	0.05	0.10	92.92	6.93
9.0	–	0.26	80.92	18.82	0.03	0.06	81.07	18.84
9.5	–	0.14	61.25	38.61	0.02	0.03	61.30	38.65
10.0	–	0.07	39.62	60.31	0.01	0.02	39.64	60.33

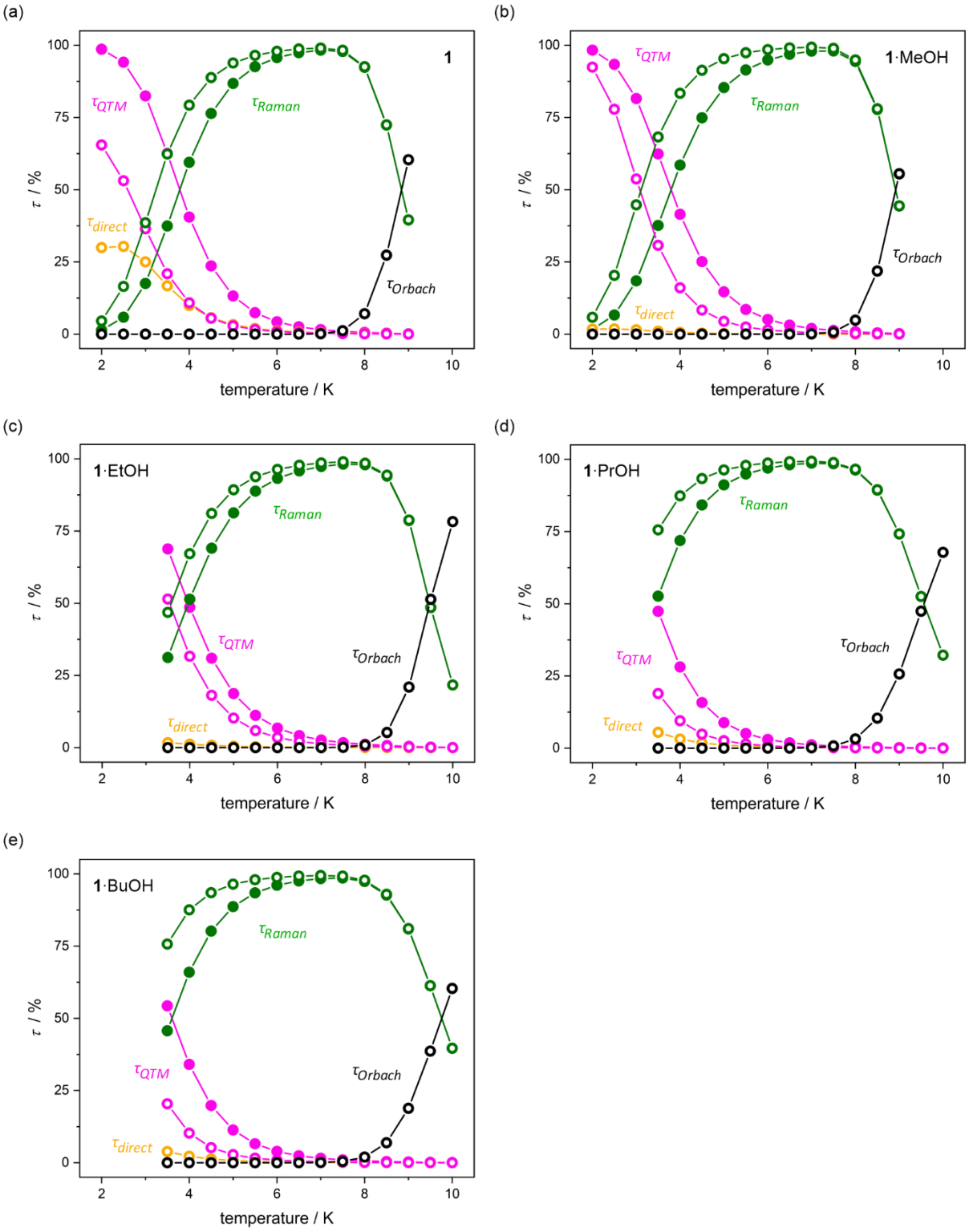

Fig. S34 Temperature dependence of percentage contributions of direct, OTM, Raman, and Orbach processes to the overall relaxation time of **1**, **1·MeOH**, **1·EtOH**, **1·PrOH**, and **1·BuOH** under the zero *dc* field (empty colored circles) and under the optimal *dc* field, H_{dc} of 600 Oe (full colored circles). The contributions, calculated for the inversion of the relaxation time (τ^{-1}) using the best-fit parameters gathered in Table S15, are presented in Table S16.

Comment to Fig. S18–S34 and Tables S15–S16 – fitting of *ac* magnetic data using the *relACs* programme

All field- and temperature-variable alternate-current (*ac*) magnetic characteristics were fitted using a *relACs* program (for details regarding this software, see the ref. [S7]). Briefly, all *ac* magnetic characteristics (frequency dependences of out-of-phase and in-phase magnetic susceptibilities together with the related Argand plots) were simultaneously fitted using a generalized Debye model:

$$\chi(\omega) = \chi_S + \frac{\chi_T - \chi_S}{(1 + i\omega\tau)^{1-\alpha}}$$

where χ_S is the adiabatic susceptibility, χ_T is the isothermal susceptibility and α represents the distribution of relaxation times (τ). The best-fit curves obtained within the *relACs* program presented in Fig. S19–S21, Fig. S22–S24, Fig. S25–S27, Fig. S28–S30, and Fig. S31–S33 for **1**, **1·MeOH**, **1·EtOH**, **1·PrOH**, and **1·BuOH**, respectively. The resulting relaxation times were plotted against the magnetic field (Fig. 19, Fig 22, Fig. 25, Fig 28, and Fig. 31) or temperature (Fig. S20–S21, Fig. S23–S24, Fig. S26–S27, Fig. S29–S30, and Fig. S32–S33). The whole set of dependencies for each compound (three curves) was simultaneously fitted taking into account four different magnetic relaxation processes:

$$\tau^{-1}(H,T) = A_{direct}H^m T + B_{Raman}T^n + {\tau_{QTM}}^{-1} + {\tau_0}^{-1}\exp\left(-\frac{\Delta E}{k_B T}\right)$$

where the first component describes a field-induced direct process, the second one reflects Raman spin-lattice relaxation, the third represents temperature-independent quantum tunneling of magnetization effect (QTM), and the last is the Orbach thermal relaxation through the real excited m_J levels. The energy barrier values of the Orbach process (ΔE) were taken from the *ab initio* calculations as the energy of the first excited m_J level (Tables S23–S27). They were fixed during the fitting procedure as leaving the related energy barrier as a free fitting parameter leads to unreliable results and the instability of the fitting procedure due to the over-parameterization. Despite a large number of remaining parameters, the procedure realized within the *relACs* program, using the simultaneous fitting of three curves allows us to obtain reasonable physical parameters. The best-fit curves, together with the course of individual relaxation processes, are shown in Fig. S19–S21, Fig. S22–S24, Fig. S25–S27, Fig. S28–S30, and Fig. S31–S33 for **1**, **1·MeOH**, **1·EtOH**, **1·PrOH**, and **1·BuOH**, respectively. To show the significant influence of the Orbach thermal relaxation on the slow magnetic relaxation time, an alternative fitting excluding this process was also made (Fig. S20e–S21e, Fig. S23e–S24e, Fig. S26e–S27e, Fig. S29e–S30e, and Fig. S32e–S33e for **1**, **1·MeOH**, **1·EtOH**, **1·PrOH**, and **1·BuOH**, respectively). The whole sets of best-fit parameters are gathered in Table S15, while the *T*-dependence of percentage contributions of individual relaxation processes was gathered in Table S16 and presented in Fig. S34.

Comment to Fig. S35 and Tables S17–S27 – details of the *ab initio* calculations

The *ab initio* calculations for all compounds, **1**, **1·MeOH**, **1·EtOH**, **1·PrOH**, and **1·BuOH**, were performed using the crystal structure taken from the single-crystal X-ray diffraction (SC-XRD) experiment without geometry optimization (Table S1). The molecular fragment that was used in the computational procedure was a part of the cyanido–bridged coordination tetrametallic $\{Dy^{III}_2Fe^{II}_2\}^{6+}$ molecule, consisting of the central Dy^{3+} ion with the ligands in its first coordination sphere together with the closest Dy^{3+} ion which was substituted by the closed-shell, diamagnetic Y^{3+} ion to enable multiconfigurational treatment of the fragment (see Fig. S35). We found, by comparison to the experimental characteristics, that the above-described cluster was sufficient to properly represent the crystal field around the metallic center. To examine local magnetic properties of Dy(III) centers, State Average Complete Active Space Self-Consistent Field (SA-CASSCF) calculations were performed using the OpenMolcas software.[S8] Scalar relativistic effects were taken into account by employing two-component second-order Douglas-Kroll-Hess (DKH2) Hamiltonian together with relativistic Atomic Natural Orbital basis sets of the ANO-RCC type.[S9–S11] To save disk space for computations, the Cholesky decomposition of ERI-s (electron repulsion integrals) was used with the $1.0 \cdot 10^{-8}$ threshold. The used model employed the VTZP basis function quality for Dy(III) centers, the VDZP for atoms occupying the first coordination sphere, and the VDZ for the others. A description of the employed basis set and its contractions are presented in Table S17. In the CASSCF step, the active space was composed of seven 4f-orbitals of Dy(III) centers with 9 active electrons – CAS(9in7), and 21 sextets, 224 quartets, and 490 doublets states arising from different possible electron distributions within $4f^9$ configuration were evaluated. In the next step, all sextets, 128 quartets, and 130 doublets optimized as spin-free states in the CASSCF step were mixed within the Restricted Active Space State Interaction (RASSI) submodule by Spin-Orbit-Coupling (SOC) within the atomic mean-field (AMFI) approximation.[S12,S13] In the final step, the resulting 898 spin-orbit states were analyzed using the SINGLE_ANISO module to obtain main magnetic axes and the pseudo-*g*-tensors of each Kramers doublet, simulate $\chi_M(T)$ and $M(H)$ magnetic dependences (Fig. S18 and Fig. S35), and decompose the ground SO states into ones with a definite projection of the total momentum on the located quantization *z*-axis of the ground Kramers doublet.[S14,S15] The energy splitting of the ground $^6H_{15/2}$ multiplet of Dy(III) centers in **1**, **1·MeOH**, **1·EtOH**, **1·PrOH**, and **1·BuOH** together with pseudo-*g*-tensor components and the composition of the ground doublet in the $|J = 15/2, m_J>$ basis are presented in Tables S18–S22.

After obtaining the local *ab initio* magnetic properties of each Dy^{3+} ion, we employed the POLY_ANISO module to simulate the magnetic interaction of two adjacent centers in each tetrametallic $\{Dy^{III}_2Fe^{II}_2\}^{6+}$ molecule. We took into account both dipole-dipole and exchange interactions. The former are treated exactly using the positions and magnetic momenta of Dy(III) centers found during the *ab initio* procedure:

$$H_{dip} = \frac{\mu_0}{4\pi r^3}\left[\boldsymbol{\mu_1}\cdot\boldsymbol{\mu_2} - \frac{3}{r^2}(\boldsymbol{\mu_1}\cdot\boldsymbol{r})(\boldsymbol{\mu_2}\cdot\boldsymbol{r})\right]$$

where $\boldsymbol{\mu_1}$ and $\boldsymbol{\mu_2}$ are magnetic dipole moment operators for two Dy(III) centers and $\boldsymbol{r}$ is the distance between them. The exchange interaction is accounted for within the Lines model[S16] utilizing a single, effective isotropic exchange parameter $\boldsymbol{J_{Lines}}$ with the Hamiltonian equation:

$$H_{exch} = \boldsymbol{J_{Lines}}\cdot\tilde{\boldsymbol{S}}_{\boldsymbol{1}}\cdot\tilde{\boldsymbol{S}}_{\boldsymbol{2}}$$

where $\tilde{\boldsymbol{S}}_{\boldsymbol{1}}$ and $\tilde{\boldsymbol{S}}_{\boldsymbol{2}}$ are previously found *ab initio* pseudo-spin operators ($\boldsymbol{S} = 15/2$) corresponding to the states with definite projections on the z-quantization axis of the ground Kramers doublet (the same used for the decomposition in Tables S18–S22). Therefore the exchange manifold has a dimension of 16 x 16 exchange states, and the rest of the excited states are treated as local states on each magnetic site, not participating in the exchange but with their contributions accounted for the simulation of magnetic properties. In this regard, the magnitude of the obtained exchange parameter cannot be compared to the usual, phenomenological pure spin Hamiltonians widely present in the literature. The $\boldsymbol{J_{Lines}}$ effective exchange parameter is the only unknown in the model, and it is found by fitting the simulated $\chi_M(T)$ dependencies to the experimental data (Fig. S18 and Fig. S35). After construction and diagonalization of the exchange Hamiltonian, we ended up with new exchange energy states, which were also analyzed for *g*-tensors and tunneling splitting between the Ising doublets. Note that, after the coupling, investigated systems are no longer Kramers ones; therefore, the degeneracy of doublets is lifted, and g_x,

g_y components of the pseudo-*g*-tensors are zero from the definition. The only relevant factor, then, is the tunneling splitting between them. The energies, tunnelling splitting, and g_z components of pseudo-*g*-tensors for **1**, **1·MeOH**, **1·EtOH**, **1·PrOH**, and **1·BuOH** are reported in Tables S23–S27.

Table S17 Description and contractions of the basis set employed in the *ab initio* calculations of the Dy^{III} crystal field in **1**, **1·MeOH**, **1·EtOH**, **1·PrOH**, and **1·BuOH**.

Basis set
Dy.ANO-RCC-VTZP 8S7P5D3F2G1H
Y.ANO-RCC-VDZ 6S5P3D
O.ANO-RCC-VDZP 3S2P1D
N.ANO-RCC-VDZP 3S2P1D (for CN^- in the first coordination sphere) N.ANO-RCC-VDZ 3S2P
C.ANO-RCC-VDZ 3S2P
H.ANO-RCC-VDZ 2S

Table S18 Summary of the energy splitting of the $^6H_{15/2}$ multiplet of Dy^{III} centers in **1** with the pseudo-*g*-tensors of each Kramers doublet and the composition in the $|m_J\rangle$ basis of the ground state.

energy and pseudo-*g*-tensor components (g_x, g_y, g_z) of 8 ground Kramers doublets			
energy / cm^{-1}	pseudo-*g*-tensor components		
	g_x	g_y	g_z
0.000	0.0065	0.0107	19.8149
178.874	0.4943	1.6644	17.9007
219.130	2.5226	4.4138	12.9256
266.210	6.9799	5.0892	3.1252
330.269	3.1828	4.2885	7.5776
400.929	1.7421	2.1752	11.3806
442.548	3.3877	5.3014	10.1581
511.701	0.4346	0.6394	17.0625

composition of the ground Kramers doublets in the $\|m_J\rangle$ the basis on the quantization axes within *J* = 15/2 manifold					
1st doublet	2nd doublet	3rd doublet	4th doublet	5th doublet	6th doublet
86.8% |-15/2>	86.8% | 15/2>	36.4% | 1/2>	36.4% | -1/2>	36.4% | 13/2>	36.4% |-13/2>
12.5% | 15/2>	12.5% |-15/2>	17.7% | -1/2>	17.7% | 1/2>	26.0% |-13/2>	26.0% | 13/2>
0.4% | -9/2>	0.4% | 9/2>	13.8% | 3/2>	13.8% | -3/2>	10.6% | 1/2>	10.6% | -1/2>
0.1% | -7/2>	0.1% | -9/2>	12.7% | -3/2>	12.7% | 3/2>	7.6% | -1/2>	7.6% | 1/2>
0.1% | 9/2>	0.1% | 7/2>	6.4% | 5/2>	6.4% | -5/2>	4.8% | 5/2>	4.8% | -5/2>
0.0% |-13/2>	0.0% |-13/2>	3.3% | -5/2>	3.3% | 5/2>	3.4% | 3/2>	3.4% | -3/2>
0.0% |-11/2>	0.0% |-11/2>	2.8% | 13/2>	2.8% |-13/2>	3.2% | 7/2>	3.2% | -7/2>
0.0% | -5/2>	0.0% | -7/2>	1.7% | 7/2>	1.7% | -7/2>	2.1% | -7/2>	2.1% | 7/2>
0.0% | -3/2>	0.0% | -5/2>	1.6% | -7/2>	1.6% | 7/2>	2.0% | 11/2>	2.0% |-11/2>
0.0% | -1/2>	0.0% | -3/2>	1.2% | 9/2>	1.2% | -9/2>	1.1% | -5/2>	1.1% | 5/2>
0.0% | 1/2>	0.0% | -1/2>	0.9% |-11/2>	0.9% | 11/2>	1.0% |-11/2>	1.0% | -9/2>
0.0% | 3/2>	0.0% | 1/2>	0.6% | 11/2>	0.6% |-11/2>	1.0% | 9/2>	1.0% | 11/2>
0.0% | 5/2>	0.0% | 3/2>	0.5% | -9/2>	0.5% | 9/2>	0.6% | -3/2>	0.6% | 3/2>
0.0% | 7/2>	0.0% | 5/2>	0.4% |-13/2>	0.4% | 13/2>	0.1% | -9/2>	0.1% | 9/2>
0.0% | 11/2>	0.0% | 11/2>	0.0% |-15/2>	0.0% |-15/2>	0.0% |-15/2>	0.0% |-15/2>
0.0% | 13/2>	0.0% | 13/2>	0.0% | 15/2>	0.0% | 15/2>	0.0% | 15/2>	0.0% | 15/2>

Table S19 Summary of the energy splitting of the $^6H_{15/2}$ multiplet of Dy^{III} centers in **1·MeOH** with the pseudo-*g*-tensors of each Kramers doublet and the composition in the $|m_J\rangle$ basis of the ground state.

energy and pseudo-*g*-tensor components (g_x, g_y, g_z) of 8 ground Kramers doublets			
energy / cm^{-1}	pseudo-*g*-tensor components		
	g_x	g_y	g_z
0.000	0.0058	0.0097	19.8128
186.318	0.4405	1.4687	17.8718
221.905	2.2798	4.2415	13.0963
273.358	6.5499	5.5696	3.3116
338.499	3.3543	4.1831	7.5159
406.076	1.4144	2.3589	11.6425
448.421	3.4806	5.4287	9.8425
520.506	0.4301	0.5308	17.1462

composition of the ground Kramers doublets in the $\|m_J\rangle$ the basis on the quantization axes within *J* = 15/2 manifold					
1st doublet	2nd doublet	3rd doublet	4th doublet	5th doublet	6th doublet
99.3% | 15/2>	99.3% |-15/2>	43.6% | 1/2>	43.6% | -1/2>	33.2% | 13/2>	33.2% |-13/2>
0.5% | 9/2>	0.5% | -9/2>	24.8% | 3/2>	24.8% | -3/2>	32.0% |-13/2>	32.0% | 13/2>
0.1% | 7/2>	0.1% |-11/2>	10.4% | 5/2>	10.4% | -5/2>	11.4% | 1/2>	11.4% | -1/2>
0.1% | 11/2>	0.1% | -7/2>	6.8% | -1/2>	6.8% | 1/2>	8.0% | -1/2>	8.0% | 1/2>
0.0% |-15/2>	0.0% |-13/2>	4.2% | 13/2>	4.2% |-13/2>	3.8% | -5/2>	3.8% | 5/2>
0.0% |-13/2>	0.0% | -5/2>	3.6% | 7/2>	3.6% | -7/2>	2.5% | 7/2>	2.5% | -7/2>
0.0% |-11/2>	0.0% | -3/2>	1.8% | -3/2>	1.8% | -9/2>	2.2% | -7/2>	2.2% | 3/2>
0.0% | -9/2>	0.0% | -1/2>	1.8% | 9/2>	1.8% | 3/2>	2.2% | -3/2>	2.2% | 7/2>
0.0% | -7/2>	0.0% | 1/2>	1.7% | 11/2>	1.7% |-11/2>	2.0% |-11/2>	2.0% | 11/2>
0.0% | -5/2>	0.0% | 3/2>	0.6% |-13/2>	0.6% | 13/2>	0.8% | 5/2>	0.8% | -5/2>
0.0% | -3/2>	0.0% | 5/2>	0.2% | -9/2>	0.2% | 7/2>	0.7% | -9/2>	0.7% |-11/2>
0.0% | -1/2>	0.0% | 7/2>	0.2% | -7/2>	0.2% | 9/2>	0.7% | 11/2>	0.7% | 9/2>
0.0% | 1/2>	0.0% | 9/2>	0.1% |-11/2>	0.1% |-15/2>	0.2% | 3/2>	0.2% | -9/2>
0.0% | 3/2>	0.0% | 11/2>	0.1% | 15/2>	0.1% | 11/2>	0.2% | 9/2>	0.2% | -3/2>
0.0% | 5/2>	0.0% | 13/2>	0.0% |-15/2>	0.0% | 5/2>	0.0% |-15/2>	0.0% |-15/2>
0.0% | 13/2>	0.0% | 15/2>	0.0% | -5/2>	0.0% | 15/2>	0.0% | 15/2>	0.0% | 15/2>

Table S20 Summary of the energy splitting of the $^6H_{15/2}$ multiplet of Dy^{III} centers in **1·EtOH** with the pseudo-*g*-tensors of each Kramers doublet and the composition in the $|m_J\rangle$ basis of the ground state.

energy and pseudo-*g*-tensor components (g_x, g_y, g_z) of 8 ground Kramers doublets			
energy / cm^{-1}	pseudo-*g*-tensor components		
	g_x	g_y	g_z
0.000	0.0046	0.0070	19.8212
205.591	0.2619	0.8797	18.1626
240.958	0.9103	2.6215	13.8505
316.482	3.7946	4.3557	8.5253
380.628	8.5556	5.9286	0.6547
437.225	1.0327	2.9341	10.1961
494.414	2.7291	4.1680	11.7066
553.684	0.8223	1.5821	16.7011

composition of the ground Kramers doublets in the $\|m_J\rangle$ the basis on the quantization axes within *J* = 15/2 manifold					
1st doublet	2nd doublet	3rd doublet	4th doublet	5th doublet	6th doublet
98.8% |-15/2>	98.8% | 15/2>	27.2% | -3/2>	27.2% | 3/2>	49.5% | 13/2>	49.5% |-13/2>
0.6% | 15/2>	0.6% |-15/2>	21.5% | 1/2>	21.5% | -1/2>	22.9% |-13/2>	22.9% | 13/2>
0.4% | -9/2>	0.4% | 9/2>	17.5% | -1/2>	17.5% | 1/2>	18.2% | 1/2>	18.2% | -1/2>
0.1% |-11/2>	0.1% | 7/2>	11.4% | -5/2>	11.4% | 5/2>	1.6% | -5/2>	1.6% | 5/2>
0.1% | -7/2>	0.1% | 11/2>	9.1% |-13/2>	9.1% | 13/2>	1.5% |-11/2>	1.5% | -7/2>
0.0% |-13/2>	0.0% |-13/2>	5.9% | -7/2>	5.9% | 7/2>	1.5% | 7/2>	1.5% | 11/2>
0.0% | -5/2>	0.0% |-11/2>	2.6% | -9/2>	2.6% | 9/2>	1.0% | -1/2>	1.0% | 1/2>
0.0% | -3/2>	0.0% | -9/2>	1.9% | 5/2>	1.9% | -5/2>	0.8% | -7/2>	0.8% | -3/2>
0.0% | -1/2>	0.0% | -7/2>	1.8% |-11/2>	1.8% | 11/2>	0.8% | 3/2>	0.8% | 7/2>
0.0% | 1/2>	0.0% | -5/2>	0.5% | 13/2>	0.5% |-13/2>	0.6% | 11/2>	0.6% |-11/2>
0.0% | 3/2>	0.0% | -3/2>	0.4% | 11/2>	0.4% |-11/2>	0.5% | -9/2>	0.5% | 9/2>
0.0% | 5/2>	0.0% | -1/2>	0.2% | 7/2>	0.2% | -7/2>	0.4% | 9/2>	0.4% | -9/2>
0.0% | 7/2>	0.0% | 1/2>	0.1% |-15/2>	0.1% | 15/2>	0.3% | -3/2>	0.3% | 3/2>
0.0% | 9/2>	0.0% | 3/2>	0.0% | 3/2>	0.0% |-15/2>	0.1% | 5/2>	0.1% | -5/2>
0.0% | 11/2>	0.0% | 5/2>	0.0% | 9/2>	0.0% | -9/2>	0.0% |-15/2>	0.0% |-15/2>
0.0% | 13/2>	0.0% | 13/2>	0.0% | 15/2>	0.0% | -3/2>	0.0% | 15/2>	0.0% | 15/2>

Table S21 Summary of the energy splitting of the $^6H_{15/2}$ multiplet of Dy^{III} centers in **1·PrOH** with the pseudo-*g*-tensors of each Kramers doublet and the composition in the $|m_J\rangle$ basis of the ground state.

energy and pseudo-*g*-tensor components (g_x, g_y, g_z) of 8 ground Kramers doublets			
energy / cm^{-1}	pseudo-*g*-tensor components		
	g_x	g_y	g_z
0.000	0.0057	0.0117	19.7935
154.513	0.1527	0.7173	18.6107
213.777	3.1993	4.6395	12.4627
265.110	3.7941	4.8075	7.2775
327.313	3.2458	5.0414	7.0901
396.316	0.6436	2.2191	11.7253
440.780	3.5637	4.1555	10.1845
503.456	0.6744	0.7541	16.5762

composition of the ground Kramers doublets in the $\|m_J\rangle$ the basis on the quantization axes within *J* = 15/2 manifold					
1st doublet	2nd doublet	3rd doublet	4th doublet	5th doublet	6th doublet
72.6% | 15/2>	72.6% |-15/2>	26.5% | -3/2>	26.5% | 3/2>	40.9% |-13/2>	40.9% | 13/2>
26.5% |-15/2>	26.5% | 15/2>	25.1% | 1/2>	25.1% | -1/2>	15.1% | 13/2>	15.1% |-13/2>
0.5% | 9/2>	0.5% | -9/2>	22.5% | -1/2>	22.5% | 1/2>	14.2% | 1/2>	14.2% | -1/2>
0.2% | -9/2>	0.2% | 9/2>	10.0% | -5/2>	10.0% | 5/2>	9.6% | -1/2>	9.6% | 1/2>
0.1% | 7/2>	0.1% | -7/2>	4.2% | -7/2>	4.2% | 7/2>	5.8% | -5/2>	5.8% | 5/2>
0.0% |-13/2>	0.0% |-13/2>	2.7% |-13/2>	2.7% | 13/2>	4.2% | -7/2>	4.2% | 7/2>
0.0% |-11/2>	0.0% |-11/2>	2.4% | 5/2>	2.4% | -5/2>	3.4% |-11/2>	3.4% | 11/2>
0.0% | -7/2>	0.0% | -5/2>	2.2% | 3/2>	2.2% | -3/2>	2.5% | -3/2>	2.5% | 3/2>
0.0% | -5/2>	0.0% | -3/2>	2.1% | -9/2>	2.1% | 9/2>	1.9% | 7/2>	1.9% | -7/2>
0.0% | -3/2>	0.0% | -1/2>	1.1% |-11/2>	1.1% | 11/2>	1.4% | -9/2>	1.4% | 9/2>
0.0% | -1/2>	0.0% | 1/2>	0.6% | 11/2>	0.6% |-11/2>	0.4% | 3/2>	0.4% | -3/2>
0.0% | 1/2>	0.0% | 3/2>	0.5% | 7/2>	0.5% | -7/2>	0.2% | 5/2>	0.2% |-11/2>
0.0% | 3/2>	0.0% | 5/2>	0.1% |-15/2>	0.1% | -9/2>	0.2% | 11/2>	0.2% | -5/2>
0.0% | 5/2>	0.0% | 7/2>	0.1% | 9/2>	0.1% | 15/2>	0.1% | 9/2>	0.1% | -9/2>
0.0% | 11/2>	0.0% | 11/2>	0.0% | 13/2>	0.0% |-15/2>	0.0% |-15/2>	0.0% |-15/2>
0.0% | 13/2>	0.0% | 13/2>	0.0% | 15/2>	0.0% |-13/2>	0.0% | 15/2>	0.0% | 15/2>

Table S22 Summary of the energy splitting of the $^6H_{15/2}$ multiplet of Dy^{III} centers in **1·BuOH** with the pseudo-*g*-tensors of each Kramers doublet and the composition in the $|m_J\rangle$ basis of the ground state.

energy and pseudo-*g*-tensor components (g_x, g_y, g_z) of 8 ground Kramers doublets			
energy / cm^{-1}	pseudo-*g*-tensor components		
	g_x	g_y	g_z
0.000	0.0073	0.0117	19.7888
159.360	0.0771	0.2373	18.9858
231.579	1.7025	2.3251	14.0638
305.188	2.5565	4.3035	8.9974
377.254	9.3383	5.6744	0.2974
428.273	0.5339	2.6656	10.8033
489.961	0.9057	4.0940	9.8322
534.628	1.5062	3.4724	14.6329

composition of the ground Kramers doublets in the $\|m_J\rangle$ the basis on the quantization axes within *J* = 15/2 manifold					
1st doublet	2nd doublet	3rd doublet	4th doublet	5th doublet	6th doublet
89.6% | 15/2>	89.6% |-15/2>	38.4% | -1/2>	38.4% | 1/2>	51.3% | 13/2>	51.3% |-13/2>
9.4% |-15/2>	9.4% | 15/2>	14.9% | -3/2>	14.9% | 3/2>	17.8% |-13/2>	17.8% | 13/2>
0.5% | 9/2>	0.5% | -9/2>	14.1% | 3/2>	14.1% | -3/2>	17.6% | 1/2>	17.6% | -1/2>
0.1% | -9/2>	0.1% |-11/2>	13.6% | -5/2>	13.6% | 5/2>	3.3% | 7/2>	3.3% | -7/2>
0.1% | 7/2>	0.1% | -7/2>	4.9% | -7/2>	4.9% | 7/2>	2.6% | -5/2>	2.6% | 5/2>
0.1% | 11/2>	0.1% | 9/2>	2.4% |-13/2>	2.4% | 13/2>	1.7% |-11/2>	1.7% | 11/2>
0.0% |-13/2>	0.0% |-13/2>	2.1% | -9/2>	2.1% | 9/2>	1.3% | 11/2>	1.3% |-11/2>
0.0% |-11/2>	0.0% | -5/2>	1.9% | 7/2>	1.9% | -7/2>	1.0% | 9/2>	1.0% | -9/2>
0.0% | -7/2>	0.0% | -3/2>	1.8% |-11/2>	1.8% | 11/2>	0.9% | -9/2>	0.9% | 7/2>
0.0% | -5/2>	0.0% | -1/2>	1.7% | 13/2>	1.7% |-13/2>	0.9% | -7/2>	0.9% | 9/2>
0.0% | -3/2>	0.0% | 1/2>	1.6% | 1/2>	1.6% | -1/2>	0.5% | -3/2>	0.5% | 3/2>
0.0% | -1/2>	0.0% | 3/2>	1.4% | 5/2>	1.4% | -5/2>	0.4% | -1/2>	0.4% | -3/2>
0.0% | 1/2>	0.0% | 5/2>	0.9% | 9/2>	0.9% | -9/2>	0.4% | 3/2>	0.4% | 1/2>
0.0% | 3/2>	0.0% | 7/2>	0.2% |-15/2>	0.2% |-11/2>	0.2% | 5/2>	0.2% | -5/2>
0.0% | 5/2>	0.0% | 11/2>	0.2% | 11/2>	0.2% | 15/2>	0.0% |-15/2>	0.0% |-15/2>
0.0% | 13/2>	0.0% | 13/2>	0.0% | 15/2>	0.0% |-15/2>	0.0% | 15/2>	0.0% | 15/2>

Table S23 Summary of the energy splitting of exchange states in **1** with the pseudo-*g*-tensor g_z components and tunneling splitting between the Ising doublets.

energy, g_z components of pseudo-*g*-tensors, and tunneling splitting between the Ising doublets		
energy / cm^{-1}	g_z	tunneling splitting / cm^{-1}
0.000 0.000	1.3221 1.3221	0.0000
1.195 1.195	1.3221 1.3221	0.0000
190.798 190.800	0.0000 39.6459	0.0016
190.801 190.802	0.0000 0.0000	0.0016
190.991 190.991	29.3890 29.3307	0.0001
191.002 191.002	0.0000 0.0000	0.0001
235.678 235.678	33.8479 33.8464	0.0000
235.693 235.693	0.0000 0.0000	0.0001
236.426 236.426	24.8914 24.9021	0.0000
236.575 236.575	0.0000 0.0000	0.0000

Table S24 Summary of the energy splitting of exchange states in **1·MeOH** with the pseudo-*g*-tensor g_z components and tunneling splitting between the Ising doublets.

energy, g_z components of pseudo-*g*-tensors, and tunneling splitting between the Ising doublets		
energy / cm^{-1}	g_z	tunneling splitting / cm^{-1}
0.000 0.000	1.3220 1.3220	0.0000
1.190 1.190	1.3220 1.3220	0.0000
199.040 199.042	0.0000 39.6423	0.0014
199.044 199.046	0.0000 0.0000	0.0015
199.264 199.264	29.5436 29.4624	0.0001
199.280 199.280	0.0000 0.0000	0.0001
238.290 238.290	33.6311 33.6353	0.0000
238.305 238.305	0.0000 0.0000	0.0001
239.022 239.022	24.7344 24.7422	0.0000
239.169 239.169	0.0000 0.0000	0.0000

Table S25 Summary of the energy splitting of exchange states in **1·EtOH** with the pseudo-*g*-tensor g_z components and tunneling splitting between the Ising doublets.

energy, g_z components of pseudo-*g*-tensors, and tunneling splitting between the Ising doublets		
energy / cm^{-1}	g_z	tunneling splitting / cm^{-1}
0.000 0.000	1.3219 1.3219	0.0000
1.195 1.195	1.3219 1.3219	0.0000
206.046 206.047	0.0000 39.6422	0.0011
206.051 206.052	0.0000 0.0000	0.0011
206.314 206.314	29.9172 29.8408	0.0000
206.338 206.338	0.0000 0.0000	0.0001
241.165 241.165	33.1693 33.1790	0.0000
241.178 241.178	0.0000 0.0000	0.0001
241.870 241.870	24.7544 24.7625	0.0000
242.011 242.011	0.0000 0.0000	0.0000

Table S26 Summary of the energy splitting of exchange states in **1·PrOH** with the pseudo-*g*-tensor g_z components and tunneling splitting between the Ising doublets.

energy, g_z components of pseudo-*g*-tensors, and tunneling splitting between the Ising doublets		
energy / cm^{-1}	g_z	tunneling splitting / cm^{-1}
0.000 0.000	1.3221 1.3221	0.0000
1.187 1.187	1.3221 1.3221	0.0000
155.065 155.066	0.0000 39.5974	0.0010
155.070 155.071	0.0000 0.0000	0.0010
155.269 155.269	29.8033 29.7892	0.0002
155.280 155.280	0.0000 0.0000	0.0001
227.196 227.196	32.9283 32.9176	0.0002
227.215 227.216	0.0000 0.0000	0.0001
227.883 227.883	25.8199 25.8411	0.0001
228.018 228.018	0.0000 38.0929	0.0000

Table S27 Summary of the energy splitting of exchange states in **1·BuOH** with the pseudo-*g*-tensor g_z components and tunneling splitting between the Ising doublets.

energy, g_z components of pseudo-*g*-tensors, and tunneling splitting between the Ising doublets		
energy / cm^{-1}	g_z	tunneling splitting / cm^{-1}
0.000 0.000	1.32189 1.32189	0.0000
1.191 1.191	1.32189 1.32189	0.0000
159.831 159.832	0.0000 39.5773	0.0008
159.839 159.839	0.0000 0.0000	0.0009
160.066 160.067	30.1334 30.1118	0.0002
160.084 160.084	0.0000 0.0000	0.0001
231.784 231.784	33.0983 33.0932	0.0001
231.805 231.805	0.0000 0.0000	0.0001
232.485 232.485	25.5837 25.6022	0.0000
232.623 232.623	0.0000 37.9654	0.0000

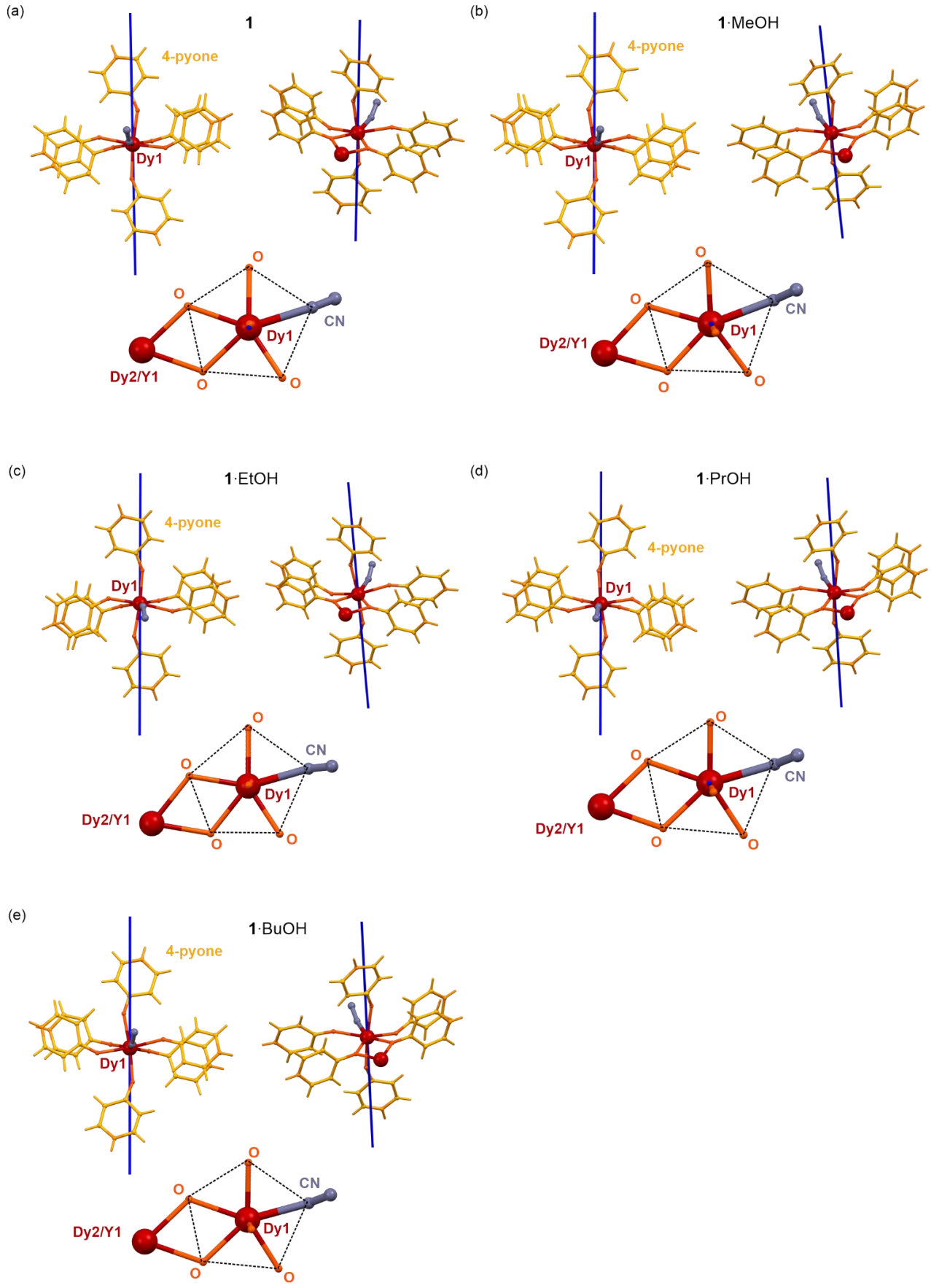

Fig. S35 Graphical presentation of the molecular fragments selected for the *ab initio* calculations for all compounds, **1** (*a*), **1·MeOH** (*b*), **1·EtOH** (*c*), **1·PrOH** (*d*), and **1·BuOH** (*e*), shown in two different orientations, together with the magnetic easy axis marked as blue-colored line (the direction of the g_z component of the pseudo-*g*-tensor of the ground state; for details, see Tables S17–S27 and the **comment** regarding the *ab initio* calculations above).

Table S28 Comparison of observed energy barrier, $\Delta E/k_B$, pre-exponential τ_0 factor, and quantum tunneling rate, τ_{QTM}, in **1**, **1·MeOH**, **1·EtOH**, **1·PrOH**, and **1·BuOH** with selected previously reported dinuclear {Dy^{III}_2}-based SMMs. For the comparison, we selected compounds whose magnetic properties were analyzed analogously (in terms of the description of magnetic dynamics) to the reported **1** to **1·BuOH** series.

dinuclear {Dy^{III}_2} compound	Dy···Dy distance / Å	$\Delta E/k_B$ / K	τ_0 / s	τ_{QTM} / ms	Ref.
$[Cp'_2Dy^{III}(I)]_2$	4.07	106	–	0.46	S17
$[\{Cp_2Dy^{III}(bta)\}_2]$	4.90	57	$1\cdot10^{-7}$	0.7	S18
$[Cp'_2Dy^{III}(Br)]_2$	4.22	139	–	2.7	S17
$[Dy^{III}_2(hmi)_2(NO_3)_2(MeOH)_2]$	3.75	56	$3\cdot10^{-7}$	3	S19
$[Dy^{III}_2(HMBA)_2(MBA)_2(DMF)_2(H_2O)_2]\cdot6H_2O$	3.69	90	$1\cdot10^{-9}$	3.2	S20
$[Dy^{III}_2(hfac)_6(H_2O)_4pz]\cdot2pz$	8.09	111	$8.4\cdot10^{-10}$	3.5	S21
$[Cp'_2Dy^{III}(Cl)]_2$	4.47	341	–	4.1	S17
$[Dy^{III}_2(HBpz_3)_4(ox)]\cdot2MeCN\cdot CH_2Cl_2$	6.14	42	–	8.2	S22
$[Dy^{III}_2(hmi)_2(NO_3)_2(MeOH)_2]_n\cdot$ MeCN	3.80	71	$7\cdot10^{-8}$	12	S19
$[Dy^{III}_2(valdien)_2(NO_3)_2]$	3.77	76	$6\cdot10^{-7}$	70	S23
$[Dy^{III}_2(opch)_2(OAc)_2(H_2O)_2]\cdot MeOH$	3.89	95	$4\cdot10^{-8}$	170	S24
$[Dy^{III}_2(ovph)_2Cl_2(MeOH)_3]\cdot MeCN$	3.86	174	$1\cdot10^{-8}$	35000	S25
1	4.10	274	$4.37\cdot10^{-17}$	320	this work
1·MeOH	4.10	284	$1.78\cdot10^{-17}$	290	
1·EtOH	4.09	206	$7.96\cdot10^{-17}$	610	
1·PrOH	4.10	155	$1.88\cdot10^{-13}$	1290	
1·BuOH	4.08	160	$1.65\cdot10^{-13}$	1230	

Cp' = cyclopentadienyltrimethylsilane anion; Cp = cyclopentadienyl; btaH=1H-1,2,3-benzotriazole; H_2hmi = (isonicotino)hydrazine; H_2MBA = 2-hydroxy-3-methoxybenzoic acid; pz = pyrazine; hfac = hexafluoro-acetylacetonate anion; $HBpz_3^-$ = hydrotris(pyrazolyl)borate anion; ox^{2-} = oxalate anion; valdien = (*N*1,*N*3-bis(3-methoxysalicylidene)diethylenetriamine); H_2opch = (*E*)-N'-(2-hydroxy-3-me-thoxybenzylidene)-pyrazine-2-carbo-hydrazide; H_2ovph = pyridine-2-carboxylic acid.

Literature:

S1 M. Llunell, D. Casanova, J. Cirera, J. Bofill, P. Alemany, S. Alvarez, M. Pinsky and D. Avnir, Program for the Stereochemical Analysis of Molecular Fragments by Means of Continuous Shape Measures and Associated Tools, SHAPE v. 2.1.; University of Barcelona: Barcelona, Spain, **2013**.

S2 D. Casanova, J. Cirera, M. Llunell, P. Alemany, D. Avnir and S. Alvarez, Minimal Distortion Pathways in Polyhedral Rearrangements, *J. Am. Chem. Soc*., 2004, **126**, 1755–1763.

S3 J. M. Miller and K. Balasanmugam, Characterization of metal complexes of 1,10-phenanthroline, 2,2′-bipyridine, and their derivatives by fast atom bombardment mass spectrometry, *Can. J. Chem*., 1989, **67**, 1496–1500.

S4 M. D. Ritz, A. C. Gerhard, R. D. Pike and D. C. Bebout, Synthesis, Solid State, Solution and ESI-MS Studies of Zinc(II) Cluster Complexes with a Branched Mixed Donor Thiolate Ligand, *Eur. J. Inorg. Chem*., 2019, **38**, 4070–4077.

S5 V. B. Di Marco and G. G. Bombi, Electrospray mass spectrometry (ESI-MS) in the study of metal–ligand solution equilibria, *Mass Spectrom. Rev.*, 2006, **25**, 347–379.

S6 U. Mayer, V. Gutmann and W. Gerger, The acceptor number — A quantitative empirical parameter for the electrophilic properties of solvents, *Monatsh. Chem.*, 1975, **106**, 1235–1257.

S7 M. Liberka, M. Zychowicz, W. Zychowicz and S. Chorazy, Neutral dicyanidoferrate(II) metalloligands for the rational design of dysprosium(III) single-molecule magnets, *Chem. Commun.*, 2022, **58**, 6381–6384.

S8 I. F. Galvam, M. Vacher, A. Alavi, C. Angeli, F. Aquilante, J. Autschbach, J. J. Bao, S. I. Bokarev, N. A. Bogdanov, R. K. Carlson, L. F. Chibotaru, J. Creutzberg, N. Dattani, M. G. Delcey, S. S. Dong, A. Dreuw, L. Freitag, L. M. Frutos, L. Gagliardi, F. Gendron, A. Giussani, L. Gonzalez, G. Grell, M. Guo, C. E. Hoyer, M. Johansson, S. Keller, S. Knecht, G. Kovacevic, E. Kallman, G. L. Manni, M. Lundberg, Y. Ma, S. Mai, J. P. Malhado, P. A. Malmqvist, P. Marquetand, S. A. Mewes, J. Norell, M. Olivucci, M. Oppel, Q. M. Phung, K. Perloot, F. Plasser, M. Reiher, A. M. Sand, I. Schapiro, P. Sharma, C. J. Stein, L. K. Sorensen, D. G. Truhlar, M. Ugandi, L. Ungur, A. Valentini, S. Vancoillie, V. Veryazov, O. Weser, T. A. Wesołowski, P.-O. Widmark, S. Wouters, A. Zech, J. P. Zobel and R. Lindh, OpenMolcas: From Source Code to Insight, *J. Chem. Theory Comput*., 2019, **15**, 5925–5964.

S9 B. O. Roos, R. Lindh, P.-A. Malmqvist, V. Veryazov and P.-O. Widmark, Main Group Atoms and Dimers Studied with a New Relativistic ANO Basis Set, *J. Phys. Chem. A*, 2004, **108**, 2851–2858.

S10 B. O. Roos, R. Lindh, P.-A. Malmqvist, V. Veryazov and P.-O. Widmark, New Relativistic ANO Basis Sets for Transition Metal Atoms, *J. Phys. Chem. A*, 2005, **109**, 6575–6579.

S11 B. O. Roos, R. Lindh, P.-A. Malmqvist, V. Veryazov and P.-O. Widmark and A. C. Borin, New Relativistic Atomic Natural Orbital Basis Sets for Lanthanide Atoms with Applications to the Ce Diatom and LuF_3, *J. Phys. Chem. A*, 2008, **112**, 11431–11435.

S12 P. A. Malmqvist, B. O. Roos and B. Schimmelpfennig, B., The restricted active space (RAS) state interaction approach with spin–orbit coupling, *Chem. Phys. Lett.*, 2002, **357**, 230−240.

S13 B. A. Heß, C. M. Marian, U. Wahlgren and O. A. Gropen, A mean-field spin-orbit method applicable to correlated wavefunctions, *Chem. Phys. Lett.*, 1996, **251**, 365−371.

S14 L. F. Chibotaru and L. Ungur, *Ab initio* calculation of anisotropic magnetic properties of complexes. I. Unique definition of pseudospin Hamiltonians and their derivation, *J. Chem. Phys.*, 2012, **137**, 064112(22).

S15 L. Ungur and L. F. Chibotaru, *Ab Initio* Crystal Field for Lanthanides, *Chem. Eur. J.*, 2017, **23**, 3708–3718.

S16 M. E. Lines, Orbital Angular Momentum in the Theory of Paramagnetic Clusters, *J. Chem. Phys.*, 1971, **55**, 2977.

S17 Y.-S. Meng, J. Xiong, M.-W. Yang, Y.-S. Qiao, Z.-Q. Zhong, H.-L. Sung, J.-B. Han, T. Liu, B.-W. Wang and S. Gao, Experimental Determination of Magnetic Anisotropy in Exchange-Bias Dysprosium Metallocene Single-Molecule Magnets, *Angew. Chem. Int.Ed.,* 2020, **59**, 13037–13043.

S18 R. A. Layfield, J. J. W. McDouall, S. A. Sulway, F. Tuna, D. Collison and R. E. P. Winpenny, Influence of the N-Bridging Ligand on Magnetic Relaxation in an Organometallic Dysprosium Single-Molecule Magnet, *Chem. Eur. J.*, 2010, **16**, 4442–4446.

S19 P.-H. Lin, T. J. Burchell, R. Clerac and M. Murugesu, Dinuclear Dysprosium(III) Single-Molecule Magnets with a Large Anisotropic Barrier, *Angew. Chem. Int. Ed.*, 2008, **47**, 8848–8851.

S20 L. Zhong, W.-B. Chen, Z.-H. Li, Z.-J. OuYang, M. Yang, Y.-Q. Zhang and S. Gao, W. Dong, Four Dinuclear and One-Dimensional-Chain Dysprosium and Terbium Complexes Based on 2-Hydroxy-3-methoxybenzoic Acid: Structures, Fluorescence, Single-Molecule-Magnet, and Ab Initio Investigation, *Inorg. Chem*., 2020, **59**, 4414–4423.

S21 Y. Ma, G.-F. Xu, X. Yang, L.-C. Li, J. Tang, S.-P. Yan, P. Cheng and D.-Z. Liao, Pyrazine-bridged Dy_2 single-molecule magnet with a large anisotropic barrier, *Chem. Commun.*, 2010, **46**, 8264–8266.

S22 G.-F. Xu, Q.-L. Wang, P. Gamez, Y. Ma, R. Clerac, J. Tang, S.-P. Yan, P. Cheng and D.-Z. Liao, A promising new route towards single-molecule magnets based on the oxalate ligand, *Chem. Commun.*, 2010, **46**, 1506–1508.

S23 J. Long, F. Habib, P.-H. Lin, I. Korobkov, G. Enright, L. Ungur, W. Wernsdorfer, L. F. Chibotaru and M. Murugesu, Single-Molecule Magnet Behavior for an Antiferromagnetically Superexchange-Coupled Dinuclear Dysprosium(III) Complex, *J. Am. Chem. Soc.*, 2011, **133**, 5319–5328.

S24 H. Tian, L. Ungar, L. Zhao, S. Ding, J. Tang and L. F. Chibotaru, Exchange Interactions Switch Tunneling: A Comparative Experimental and Theoretical Study on Relaxation Dynamics by Targeted Metal Ion Replacement, *Chem. Eur. J.*, 2018, **24**, 9928–9939.

S25 Y.-N. Guo, G.-F. Xu, W. Wernsdorfer, L. Ungur, Y. Guo, J. Tang, H.-J. Zhang, L. F. Chibotaru and A. K. Powell, Strong Axiality and Ising Exchange Interaction Suppress Zero-Field Tunneling of Magnetization of an Asymmetric Dy_2 Single-Molecule Magnet, *J. Am. Chem. Soc.,* 2011, **133**, 11948–11951.